

# Study of Quasielastic 1p-shell Proton Knockout in the $^{16}\text{O}(\text{e},\text{e}'\text{p})$ Reaction at $Q^2 = 0.8 \text{ (GeV/c)}^2$

by

Juncai Gao

B.Sc., University of Science and Technology of China (1990)

M.Sc., Institute of High Energy Physics, China (1994)

Submitted to the Department of Physics  
in partial fulfillment of the requirements for the degree of

Doctor of Philosophy

at the

MASSACHUSETTS INSTITUTE OF TECHNOLOGY

June 1999

© Massachusetts Institute of Technology 1999. All rights reserved.

Signature of Author .....

Department of Physics  
February 12, 1999

Certified by .....

Professor William Bertozzi  
Thesis Supervisor

Accepted by .....

Professor Thomas J. Greytak  
Associate Department Head for Education

# Study of Quasielastic 1p-shell Proton Knockout in the $^{16}\text{O}(e,e'p)$ Reaction at $Q^2 = 0.8 \text{ (GeV/c)}^2$

by

Juncai Gao

Submitted to the Department of Physics  
on February 12, 1999, in partial fulfillment of the  
requirements for the degree of  
Doctor of Philosophy

## Abstract

Coincidence cross sections and the structure functions  $R_{L+TT}$ ,  $R_T$  and  $R_{LT}$  have been obtained for the quasielastic  $^{16}\text{O}(e, e'p)$  reaction with the proton knocked out from the  $1p_{1/2}$  and  $1p_{3/2}$  states in perpendicular kinematics. The nominal energy transfer  $\omega$  was 439 MeV, the nominal  $Q^2$  was  $0.8 \text{ (GeV/c)}^2$  and the kinetic energy of knocked-out proton was 427 MeV. The data was taken in Hall A, Jefferson Laboratory, using two high resolution spectrometers to detect electrons and protons respectively. Nominal beam energies 845 MeV, 1645 MeV, and 2445 MeV were employed. For each beam energy, the momentum and angle of electron arm were fixed, while the angle between the proton momentum and the momentum transfer  $\vec{q}$  was varied to map out the missing momentum.  $R_{LT}$  was separated out to  $\sim 350 \text{ MeV/c}$  in missing momentum.  $R_{L+TT}$  and  $R_T$  were separated out to  $\sim 280 \text{ MeV/c}$  in missing momentum.  $R_L$  and  $R_T$  were separated at a missing momentum of 52.5 MeV/c for the data taken with hadron arm along  $\vec{q}$ .

The measured cross sections and response functions agree with both relativistic and non-relativistic DWIA calculations employing spectroscopic factors between 60-75% for  $1p_{1/2}$  and  $1p_{3/2}$  states. The left-right asymmetry does not support the non-relativistic DWIA calculation using the Weyl gauge. Also, the left-right asymmetry measurement favors the relativistic calculation.

This thesis describes the details of the experimental setup, the calibration of the spectrometers, the techniques used in the data analysis to derive the final cross sections as well as the response functions, and the comparison of the results with the theoretical calculations.

Thesis Supervisor: William Bertozzi

Title: Professor of Physics

# Contents

<b>1</b>	<b>Introduction</b>	<b>6</b>
1.1	Electron Scattering . . . . .	6
1.2	Inclusive Electron Scattering - $(e, e')$ . . . . .	8
1.2.1	General $(e, e')$ . . . . .	8
1.2.2	Quasielastic $(e, e')$ . . . . .	9
1.3	Exclusive Electron Scattering - $(e, e'p)$ . . . . .	10
1.3.1	One-Photon Exchange Approximation . . . . .	10
1.3.2	Plane Wave Impulse Approximation . . . . .	15
1.3.3	Distorted Wave Impulse Approximation . . . . .	17
1.3.4	Coulomb Distortion . . . . .	18
1.3.5	Two-Body Currents . . . . .	19
1.4	$^{16}\text{O}(e, e'p)$ . . . . .	19
1.4.1	Previous Experiments . . . . .	20
1.4.2	This Experiment . . . . .	29
<b>2</b>	<b>The Experimental Setup</b>	<b>32</b>
2.1	Overview . . . . .	32
2.2	Accelerator . . . . .	32
2.3	Hall A Setup . . . . .	34
2.4	Beamline . . . . .	36
2.4.1	Beam Current Monitors . . . . .	36
2.4.2	Beam Position Monitors . . . . .	38

2.5	High Resolution Spectrometer . . . . .	39
2.6	Detector Packages . . . . .	41
2.6.1	Scintillators . . . . .	43
2.6.2	Vertical Drift Chambers . . . . .	44
2.6.3	Gas Cerenkov . . . . .	48
2.7	Waterfall Target . . . . .	49
2.8	Trigger Electronics . . . . .	51
2.9	Data Acquisition . . . . .	53
<b>3</b>	<b>Data Analysis</b>	<b>56</b>
3.1	The Analyzer - ESPACE . . . . .	56
3.2	Focal Plane Track Reconstruction and $e^-/\pi^-$ Separation . . . . .	57
3.2.1	Scintillators . . . . .	57
3.2.2	Focal Plane Trajectory Reconstruction . . . . .	58
3.2.3	$e^-/\pi^-$ Separation . . . . .	64
3.3	Calibrations of High Resolution Spectrometers . . . . .	66
3.3.1	Optics Study of HRS . . . . .	66
3.3.2	Absolute Momentum Measurement . . . . .	78
3.3.3	Coincidence Time-of-Flight . . . . .	78
3.3.4	Deadtime Correction . . . . .	82
3.4	Spectrometer Efficiency . . . . .	85
3.4.1	Focal Plane Relative Efficiency . . . . .	85
3.4.2	Normalization . . . . .	93
3.4.3	Waterfall Foil Thickness . . . . .	97
3.5	Phase Space Volume Calculation . . . . .	97
3.6	Cross Section Calculation . . . . .	99
3.7	Radiative Corrections . . . . .	100
3.7.1	Theory of Radiative Corrections . . . . .	101
3.7.2	Procedure of Radiative Correction . . . . .	105
3.8	Response Function Separation . . . . .	109

3.8.1	$R_{LT}$ Separation . . . . .	109
3.8.2	$R_{L+TT}$ , $R_T$ Separation . . . . .	112
3.8.3	$R_L$ , $R_T$ Separation . . . . .	114
<b>4</b>	<b>Results and Conclusion</b>	<b>118</b>
4.1	Experimental Results and Systematic Uncertainties . . . . .	118
4.2	Comparison with Theories . . . . .	122
4.2.1	NRDWIA from Kelly . . . . .	122
4.2.2	RDWIA from Van Orden . . . . .	126
4.2.3	Comparison with the Calculations . . . . .	127
4.3	Summary and Conclusions . . . . .	141
<b>A</b>	<b>Beam Energy Measurement</b>	<b>143</b>
A.1	Introduction . . . . .	143
A.2	Beam Energy Measurement . . . . .	143
A.2.1	$^{12}\text{C}(e, e')$ Technique . . . . .	143
A.2.2	$\text{H}(e, e'p)$ Scattering Angle Technique . . . . .	150
A.2.3	$^{16}\text{O}(e, e'p)$ Missing Energy Technique . . . . .	155
A.3	Conclusions . . . . .	161
<b>B</b>	<b>Matrix Elements of HRSs</b>	<b>162</b>

# Chapter 1

## Introduction

### 1.1 Electron Scattering

Electron scattering is one of the most powerful methods of studying nuclear structure and interactions. In this scattering process, the interaction between the electron and the nucleus can be described by the exchange of virtual photons. The virtual photons interact with the charge density and the electromagnetic currents of the target nucleus, transferring energy  $\omega$  and momentum  $\vec{q}$ . By measuring the cross section for electron scattering at various kinematics (final electron energies and scattering angles), one can map out the response of the nucleus to the electromagnetic probe.

Electron scattering has several advantages as a nuclear probe:

(1) The electromagnetic interaction prevails in the process of electron scattering. The electromagnetic interaction is well understood and can be calculated very accurately using Quantum Electrodynamics (QED). This allows one to probe the details of the nuclear current,  $J_\mu$ , and extract detailed information about nuclear structure. On the contrary, proton and pion scattering is dominated by the strong force, where phenomenological models must be relied upon to interpret the nuclear structure.

(2) The electromagnetic interaction is relatively weak. Thus the interaction can be

described with a one-photon exchange approximation for the lighter nuclei. This also means that the virtual photon can penetrate the surface of the nucleus and interact with the nuclear current throughout the entire nuclear volume. On the other hand, hadronic probes interact strongly, and thus primarily sample the nuclear surface.

(3) The virtual photon carries energy and 3-momentum which can be varied independently (subject to the restriction  $Q^2 = \vec{q}^2 - \omega^2 \geq 0$ ). Thus, for example, one could fix the energy transfer  $\omega$  and (by measuring the nuclear responses at a range of  $\vec{q}$  values) map out the spatial distributions of the nuclear charge and current densities. Note that for real photon absorption,  $\vec{q}^2 - \omega^2 = 0$

(4) The virtual photon exchanged in electron scattering has both longitudinal and transverse polarizations. A longitudinally-polarized photon interacts with the charge density of the nucleus, whereas a transversely-polarized photon interacts with the nuclear electromagnetic 3-vector current density. Thus, electron scattering can probe different components of the nuclear electromagnetic current. Note that the polarization of a real photon can only be transverse.

However, electron scattering has its drawbacks and difficulties:

(1) A weakly-interacting probe means a small cross section. Thus, the counting rate for an electron scattering experiment (especially a coincidence experiment) is usually low, requiring large amounts of beam time. The generally large cross sections encountered for hadron scattering from nuclear targets allow the experimenter to make statistically similar measurements with smaller amounts of beam time.

(2) The analysis and interpretation of electron scattering data is complicated by radiation processes which can cause large effects and corrections. Radiative unfolding is manageable for single arm experiments, but for coincidence experiments, has only recently been investigated.

## 1.2 Inclusive Electron Scattering - $(e, e')$

### 1.2.1 General $(e, e')$

In a single arm electron scattering experiment, the electron beam is incident on the target, and a spectrometer set at a particular momentum and angle detects the scattered electron. Since the final nuclear state is not unique, this is called an inclusive experiment. A general inclusive  $(e, e')$  spectrum showing the cross section  $d\sigma/d\Omega_e d\omega$  (where  $d\Omega_e$  is the solid angle the electron scatters into) as a function of  $\omega$  for a fixed value of  $Q^2 = \vec{q}^2 - \omega^2$  is presented in Figure 1-1.

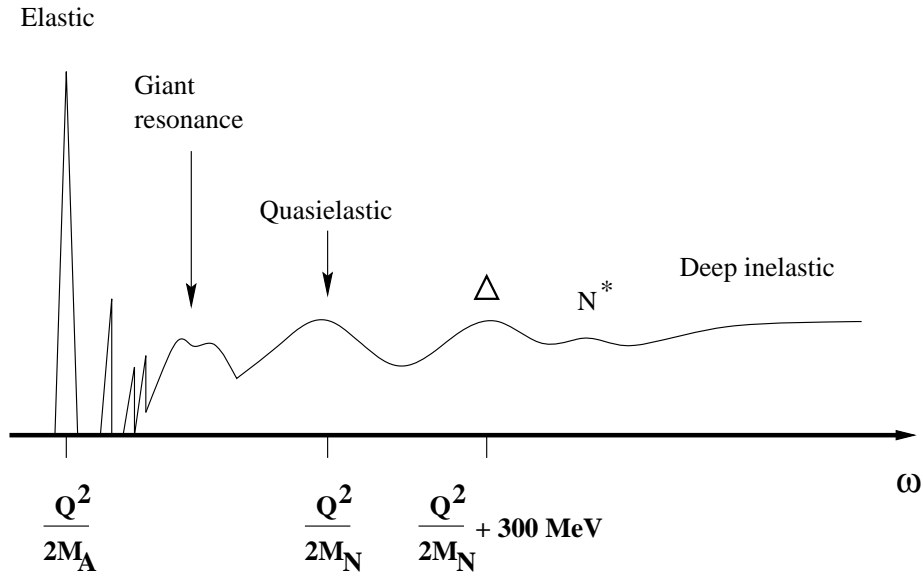


Figure 1-1: General  $(e, e')$  spectrum.

The first sharp peak is due to electron elastic scattering from the nucleus. It is called the elastic peak, with  $\omega = Q^2/2M_A$ . The next few sharp peaks at higher  $\omega$  correspond to nuclear excitation to discrete states. Then comes the excitation of the collective modes, which is called the “Giant Resonances”. At still higher  $\omega$ , there

is a broad bump peaked at  $\omega \cong Q^2/2M_N$  (where  $M_N$  is the mass of a nucleon). This is called the “quasielastic peak”, which corresponds to the virtual photon being absorbed by a single nucleon with mass  $M_N$ . The next bumps at higher energy transfer correspond to the excitation of a nucleon to the  $\Delta$  and  $N^*$ . The region well beyond  $N^*$  excitation is called the “Deep Inelastic Scattering”, where the nucleon resonances are broad, overlapping, and not distinguished as bumps. In this region, the electron may be thought of as scattering quasielastically from the individual constituent quarks of the nucleon.

In the first Born approximation (one-photon exchange), the single arm  $(e, e')$  cross section can be written as

$$\frac{d^3\sigma}{d\Omega_{e'}d\omega} = \sigma_M \left\{ \frac{Q^4}{\vec{q}^4} R_L(\omega, Q^2) + \left( \frac{Q^2}{2\vec{q}^2} + \tan^2\left(\frac{\theta_e}{2}\right) \right) R_T(\omega, Q^2) \right\}. \quad (1.1)$$

Here  $R_L(\omega, Q^2)$  and  $R_T(\omega, Q^2)$  are the longitudinal and transverse response functions,  $\theta_e$  is the electron scattering angle, and  $\sigma_M$  is the Mott cross section

$$\sigma_M = \frac{\alpha^2 \cos^2(\frac{\theta_e}{2})}{4E_i^2 \sin^4(\frac{\theta_e}{2})} \quad (1.2)$$

where  $\alpha$  is the fine structure constant ( $\sim 1/137$ ), and  $E_i$  is the incident electron energy. To separate the two response functions, the cross section must be measured at two different electron kinematics with  $\omega$  and  $Q^2$  fixed.

### 1.2.2 Quasielastic $(e, e')$

An interesting topic is the quasielastic  $(e, e')$  scattering from complex nuclei. A simple but reasonable Fermi-gas model can be used to describe this process. In this model the nucleus is just a collection of non-interacting nucleons characterized by a uniform momentum distribution  $n(\vec{p})$  up to Fermi momentum  $p_f$ , which is given by

$$p_f = (3\pi^2 \hbar^3 \rho)^{1/3} \quad (1.3)$$

where the proton/neutron number density  $\rho \approx 0.038\text{fm}^{-3}$ , so that  $p_f \approx 270\text{ MeV}/c$ . The Fermi energy is then given by  $\epsilon_f = p_f^2/2M_N \approx 38\text{MeV}$ . A virtual photon with energy  $\omega$  and momentum  $\vec{q}$  is then absorbed by a single nucleon. Energy and momentum conservation (in non-relativistic approximation) requires

$$\omega = \frac{(\vec{q} + \vec{p})^2}{2M_N} - \left( \frac{\vec{p}^2}{2M_N} - \bar{\epsilon} \right) = \frac{\vec{q}^2}{2M_N} + \frac{\vec{q} \cdot \vec{p}}{M_N} + \bar{\epsilon} \quad (1.4)$$

where  $\bar{\epsilon}$  is an energy shift which represents the binding energy and many-body effects. From equation 1.4, one can note that the quasielastic scattering is peaked at  $\omega = \vec{q}^2/2M_N + \bar{\epsilon}$ , and the width is  $\sim qp_f/M_N$ .

Whitney *et al.* [1] used this model with calculations by E. Moniz [2] to fit quasielastic data on a wide range of nuclei, from  ${}^6\text{Li}$  to  ${}^{208}\text{Pb}$ . The variables fitted were  $p_f$  and  $\bar{\epsilon}$ . The quasielastic peaks were reasonably well reproduced. De Forest [3] pointed out that when the more realistic harmonic oscillator momentum densities are used, along with center-of-mass motion corrections and experimental separation energies, the good agreement can only be achieved when final state interactions are taken into account.

### 1.3 Exclusive Electron Scattering - $(e, e'p)$

In a coincidence electron scattering experiment, the scattered electron is detected by one spectrometer, at the same time the knocked-out hadron is detected by another spectrometer. Since the final state can be selected, this is called an exclusive measurement. If the detected hadron is a proton, this reaction is called  $(e, e'p)$ .

#### 1.3.1 One-Photon Exchange Approximation

For light or medium nuclei where  $Z\alpha \ll 1$  ( $Z$  is the number of protons inside nucleus and  $\alpha$  is the fine structure constant), it is a good approximation to assume only

one photon is exchanged in the process of electron scattering. Figure 1-2 is the Feynman diagram of the reaction  $A(e, e'p)B$ , where  $k_i^\mu = (E_i, \vec{k}_i)$  and  $k_f^\mu = (E_f, \vec{k}_f)$  are the initial and final electron 4-momenta,  $p_A^\mu = (E_A, \vec{p}_A)$  and  $p_B^\mu = (E_B, \vec{p}_B)$  are the initial and final target 4-momenta,  $p_p^\mu = (E_p, \vec{p}_p)$  is the ejectile 4-momentum, and  $q^\mu = k_i^\mu - k_f^\mu = (\omega, \vec{q})$  is the 4-momentum transfer carried by the virtual photon. The plane defined by the incident and outgoing electron momenta is called scattering plane, while the plane defined by the momentum transfer  $\vec{q}$  and knocked-out proton momentum  $\vec{p}_p$  is called ejectile plane. The angle between these two planes is the out-of-plane angle  $\phi$ .

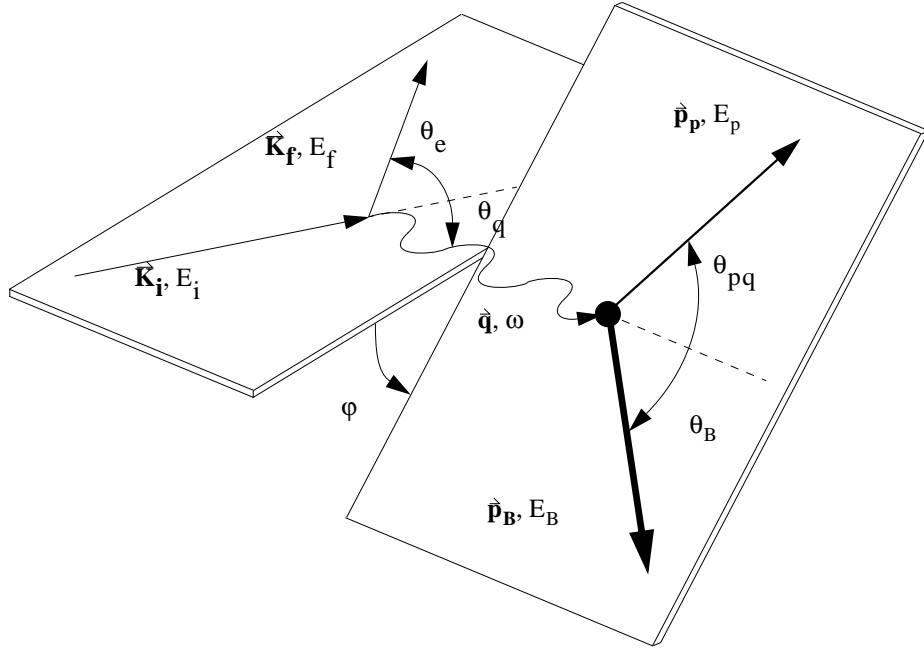


Figure 1-2: The Feynman diagram for  $(e, e'p)$ .

The invariant cross section can be written as [6]

$$d\sigma = (2\pi)^{-3} \frac{E_f}{E_i} \frac{\alpha^2}{Q^4} \eta_{\mu\nu} W_{\mu\nu} dE_f d\Omega_e d^3\vec{p}_p \quad (1.5)$$

where  $d\Omega_e$  is the solid angle for electron momentum in the laboratory,  $\eta_{\mu\nu}$  and  $W_{\mu\nu}$  are the electron and nuclear response tensors. Using

$$d^3\vec{p}_p = E_p p_p dE_p d\Omega_p \quad (1.6)$$

where  $d\Omega_p$  is the solid angle for the proton momentum in the laboratory, one can obtain the sixfold differential cross section

$$\frac{d^6\sigma}{dE_f d\Omega_e dE_p d\Omega_p} = \frac{E_p p_p}{(2\pi)^3} \frac{E_f}{E_i} \frac{\alpha^2}{Q^4} \eta_{\mu\nu} W_{\mu\nu}. \quad (1.7)$$

For  $(e, e'p)$  reactions in which only a single discrete state or narrow resonance of the target is excited, one can use

$$R = \int dE_p \delta(E_p + E_B - \omega - M_A) = \left| 1 - \frac{E_p}{E_B} \frac{\vec{p}_p \cdot \vec{p}_B}{\vec{p}_p \cdot \vec{p}_p} \right|^{-1} \quad (1.8)$$

to integrate over the peak in proton energy to obtain a fivefold differential cross section

$$\frac{d^5\sigma}{dE_f d\Omega_e d\Omega_p} = R \frac{E_p p_p}{(2\pi)^3} \frac{E_f}{E_i} \frac{\alpha^2}{Q^4} \eta_{\mu\nu} W_{\mu\nu} \quad (1.9)$$

where  $R$  is a recoil factor.

For extremely relativistic electrons, the electron mass can be neglected and the electron response tensor can be written as

$$\eta_{\mu\nu} = 2(k_{i\mu} k_{f\nu} + k_{f\mu} k_{i\nu} - k_i \cdot k_f g_{\mu\nu}) \quad (1.10)$$

and it can be expressed in the alternative form

$$\eta_{\mu\nu} = K_\mu K_\nu - q_\mu q_\nu - Q^2 g_{\mu\nu} \quad (1.11)$$

where  $K_\mu = k_{i\mu} + k_{f\mu}$ , and  $q_\mu = k_{i\mu} - k_{f\mu}$ .

The nuclear response tensor is bilinear in matrix elements of the nuclear current operator. Establishing the notation

$$W_{\mu\nu} = \langle J_\mu J_\nu^+ \rangle \quad (1.12)$$

where the angle brackets denote products of matrix elements appropriately averaged over initial states and summed over final states. Nuclear electromagnetic current conservation requires

$$q_\mu W^{\mu\nu} = W^{\mu\nu} q_\nu = 0 \quad (1.13)$$

and therefore, the contraction of electron and nuclear response tensors reduces to the form

$$\eta_{\mu\nu} W_{\mu\nu} = \langle K \cdot J K \cdot J^+ - Q^2 J \cdot J^+ \rangle. \quad (1.14)$$

The continuity equation

$$J_z = \frac{\omega}{|\vec{q}|} \rho \quad (1.15)$$

can be used to eliminate the longitudinal component of the current in favor of the charge  $\rho$ . After some tedious but straightforward algebra, one can obtain

$$\eta_{\mu\nu} W_{\mu\nu} = 4E_i E_f \cos^2 \frac{\theta_e}{2} [V_L R_L + V_T R_T + V_{LT} R_{LT} \cos \phi + V_{TT} R_{TT} \cos 2\phi] \quad (1.16)$$

therefore

$$\frac{d^6 \sigma}{dE_f d\Omega_e dE_p d\Omega_p} = \frac{E_p p_p}{(2\pi)^3} \sigma_M [V_L R_L + V_T R_T + V_{LT} R_{LT} \cos \phi + V_{TT} R_{TT} \cos 2\phi] \quad (1.17)$$

and for a given discrete state,

$$\frac{d^5\sigma}{dE_f d\Omega_e d\Omega_p} = R \frac{E_p p_p}{(2\pi)^3} \sigma_M [V_L R_L + V_T R_T + V_{LT} R_{LT} \cos \phi + V_{TT} R_{TT} \cos 2\phi] \quad (1.18)$$

where  $\sigma_M$  is the Mott cross section.

The kinematic factors are

$$\begin{aligned} V_L &= \frac{Q^4}{\vec{q}^4} \\ V_T &= \frac{Q^2}{2\vec{q}^2} + \tan^2(\theta_e/2) \\ V_{LT} &= \frac{Q^2}{\vec{q}^2} \left[ \frac{Q^2}{\vec{q}^2} + \tan^2(\theta_e/2) \right]^{\frac{1}{2}} \\ V_{TT} &= \frac{Q^2}{2\vec{q}^2} \end{aligned}$$

and the response functions can be expressed in form of nuclear current tensors

$$\begin{aligned} R_L &= \langle W_{00} \rangle = \langle \rho \rho^+ \rangle \\ R_T &= \langle W_{xx} + W_{yy} \rangle = \langle J_{\parallel} J_{\parallel}^+ + J_{\perp} J_{\perp}^+ \rangle \\ R_{LT} \cos \phi &= -\langle W_{0x} + W_{x0} \rangle = -\langle \rho J_{\parallel}^+ + J_{\parallel} \rho^+ \rangle \\ R_{TT} \cos 2\phi &= \langle W_{xx} - W_{yy} \rangle = \langle J_{\parallel} J_{\parallel}^+ - J_{\perp} J_{\perp}^+ \rangle \end{aligned}$$

where  $\rho$  is the charge component of the nuclear current,  $J_{\parallel}$  is the transverse component of the nuclear current in the scattering plane and  $J_{\perp}$  is the transverse component of the nuclear current orthogonal to that plane. Both  $J_{\parallel}$  and  $J_{\perp}$  are orthogonal to  $\vec{q}$ . The longitudinal response function  $R_L$  arises from the charge and the longitudinal component of the nuclear current. The transverse response function  $R_T$  is the incoherent sum of the contributions from the two transverse components of the nuclear current. The longitudinal-transverse interference response function  $R_{LT}$  is the interference of the longitudinal current with the transverse component of the nuclear

current in the scattering plane. The transverse-transverse interference response function  $R_{TT}$  is the interference between the two transverse components of the nuclear current.

In general,  $R_L, R_T, R_{LT}$  and  $R_{TT}$  are functions of variables  $\omega, Q^2, \theta_{pq}$  and  $p_p$ . In parallel kinematics ( $\vec{p}_p \parallel \vec{q}$ ), the orientation of the reaction plane (the azimuthal angle  $\phi$ ) becomes undefined, and only two response functions,  $R_L$  and  $R_T$  exist in the cross section expression.

### 1.3.2 Plane Wave Impulse Approximation

In the Plane Wave Impulse Approximation (PWIA), the virtual photon is totally absorbed by the proton, while the proton comes out without further interaction with the residual nucleus and is detected in the experiment. Figure 1-3 is a diagram of this process.

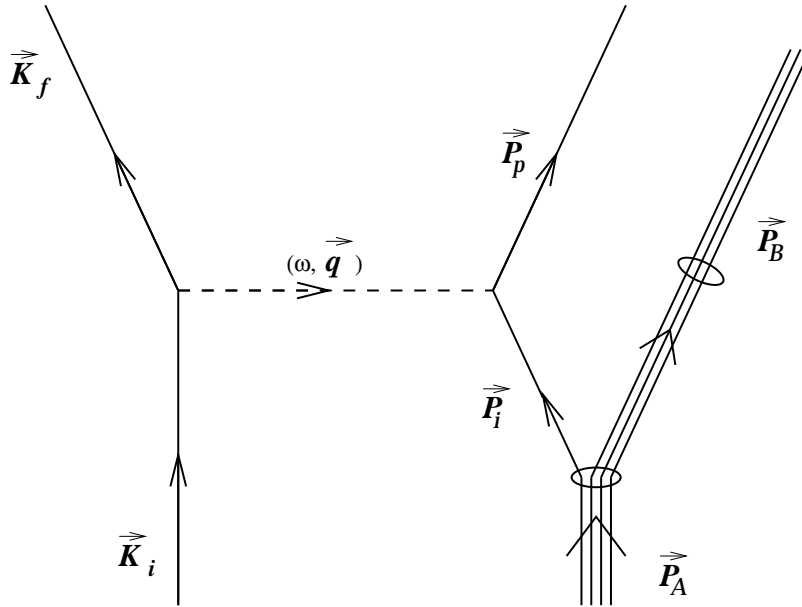


Figure 1-3: Plane Wave Impulse Approximation in  $(e, e'p)$ .

Missing momentum  $\vec{p}_{miss}$  and missing energy  $E_{miss}$  are defined as

$$\vec{p}_{miss} = \vec{p}_p - \vec{q} \quad (1.19)$$

$$E_{miss} = \omega - T_p - T_B \quad (1.20)$$

where  $T_p$  and  $T_B$  are the kinetic energies of the proton and the residual nucleus respectively. Energy and momentum conservation requires

$$\vec{p}_{miss} = \vec{p}_p - \vec{q} = -\vec{p}_B \quad (1.21)$$

$$E_{miss} = \omega - T_p - T_B = M_B + M_p - M_A \quad (1.22)$$

where  $\vec{p}_B$  is the momentum of the residual nucleus. Therefore,  $\vec{p}_{miss}$  is the proton initial momentum inside the nucleus, and  $E_{miss}$  is the binding energy of the proton.

In non-relativistic PWIA, the cross section can be factorized

$$\frac{d^6\sigma}{dE_f d\Omega_e dE_p d\Omega_p} = \frac{E_p p_p}{(2\pi)^3} \sigma_{ep} S(E_{miss}, \vec{p}_{miss}) \quad (1.23)$$

where  $\sigma_{ep}$  is the off-shell  $ep$  cross section [7], and  $S(E_{miss}, \vec{p}_{miss})$  is the spectral function, which can be written as

$$S(E_{miss}, \vec{p}_{miss}) = \sum_{\alpha} |\phi_{\alpha}(\vec{p}_{miss})|^2 \delta(E_{\alpha} - E_{miss}). \quad (1.24)$$

Here  $|\phi(\vec{p}_{miss})|^2$  is the proton momentum distribution, and  $E_{\alpha}$  is the binding energy for the shell  $\alpha$ . Therefore the spectral function  $S(E_{miss}, \vec{p}_{miss})$  can be interpreted as the probability of finding a proton with initial momentum  $\vec{p}_{miss}$  and binding energy  $E_{miss}$  inside the nucleus.

### 1.3.3 Distorted Wave Impulse Approximation

In the Distorted Wave Impulse Approximation (DWIA), the assumptions for the PWIA are made, and further, the interaction between the knocked-out proton and the residual nucleus is taken into account. Figure 1-4 shows the diagram for DWIA.

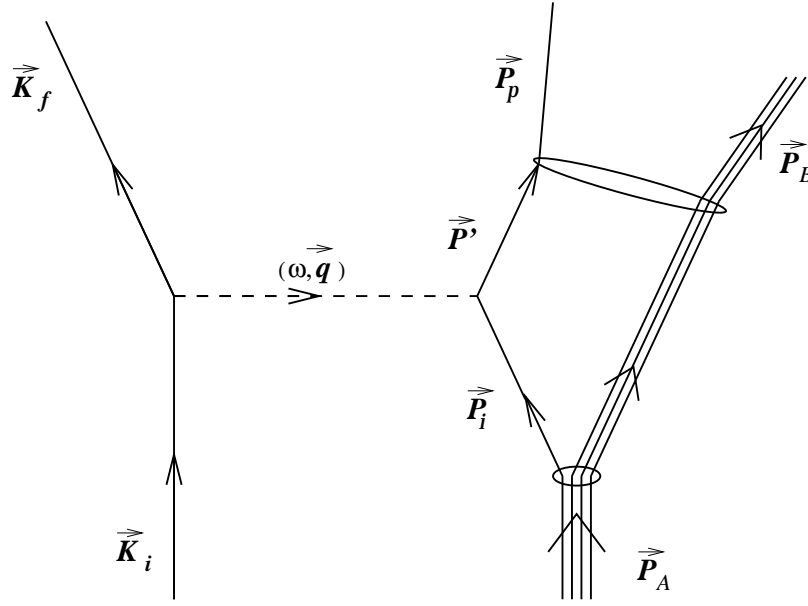


Figure 1-4: Distorted Wave Impulse Approximation in  $(e, e'p)$ .

Similarly, a distorted spectral function is defined as

$$\frac{d^6\sigma}{dE_f d\Omega_e dE_p d\Omega_p} = \frac{E_p p_p}{(2\pi)^3} \sigma_{ep} S^D(E_{miss}, \vec{p}_{miss}, \vec{p}_p). \quad (1.25)$$

Final-state interactions between the proton and the residual nucleus make the distorted spectral function  $S^D(E_{miss}, \vec{p}_{miss}, \vec{p}_p)$  depend upon the proton momentum  $\vec{p}_p$  and the angle between the initial and final proton momenta, whereas the undistorted spectral function depends only on  $E_{miss}$  and  $\vec{p}_{miss}$ . The distorted and undistorted

spectral functions are related by

$$S^D(E_{miss}, \vec{p}_{miss}, \vec{p}_p) = \int d^3\vec{p}_i |\chi(\vec{p}_p, \vec{p}_i + \vec{q})|^2 S(E_{miss}, \vec{p}_i) \quad (1.26)$$

where  $\chi$  is the proton distorted wave which satisfies the Schrödinger equation

$$[\nabla^2 + k^2 - 2\mu(U^C + U^{LS} \vec{L} \cdot \vec{S})]\chi = 0 \quad (1.27)$$

while  $k$  is the proton wave number and  $\mu$  is the reduced mass

$$\mu = \frac{E_p E_B}{E_p + E_B} \quad (1.28)$$

$U^C$  and  $U^{LS}$  are the central and spin-orbit complex optical potentials. Usually the optical potentials are extracted from fits to proton elastic scattering data.

### 1.3.4 Coulomb Distortion

The dominant effects of Coulomb distortion upon the electron wave functions can be described using the Effective Momentum Approximation [17] (EMA). In this approximation, the asymptotic electron momenta  $k$  are replaced by  $k_{eff}$  to account for the acceleration of the electron by the mean electrostatic potential

$$\vec{k}_{eff} = \vec{k} + \frac{3\alpha Z}{2R_Z} \frac{\vec{k}}{|\vec{k}|}. \quad (1.29)$$

Here  $R_Z$  is the nuclear radius assuming it is a uniformly charged sphere. Therefore, the effective momentum transfer is

$$\vec{q}_{eff} = \vec{q} + \frac{3\alpha Z}{2R_Z E_i} (\vec{q} - \omega \frac{\vec{k}_f}{|\vec{k}_f|}). \quad (1.30)$$

For a light or medium nucleus and high beam energies, the effect of Coulomb distortion is small.

### 1.3.5 Two-Body Currents

In the Impulse Approximation (IA), the nucleus is described entirely in terms of nucleonic degrees-of-freedom. Exchanged mesons only manifest themselves through the effective mean-field potential and the nucleon wave functions. However, the virtual photon may couple directly with the meson currents. Figure 1-5 shows the Feynman diagrams for meson-exchange currents (MECs) and isobar currents (ICs).

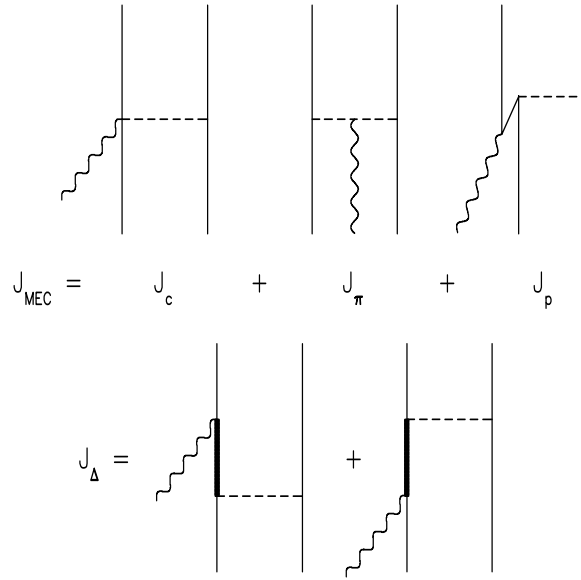


Figure 1-5: Two-Body currents.

In the non-relativistic approximation, the longitudinal part of the two-body current is eliminated, so that only the transverse part remains. Thus, the two-body current will mainly affect the transverse and interference response functions.

## 1.4 $^{16}\text{O}(e, e'p)$

$^{16}\text{O}$  is a doubly-magic, closed-shell nucleus. Its bound state wavefunction is relatively easy to calculate. As proton elastic scattering from  $^{16}\text{O}$  has been studied over a

wide range of kinematics, the final state interactions for  $^{16}\text{O}(e, e'p)$  reaction are well understood. Therefore, one can derive good predictions for both the cross sections and the response functions. This makes  $^{16}\text{O}$  a unique candidate for the study of the reaction mechanism for proton knockout.

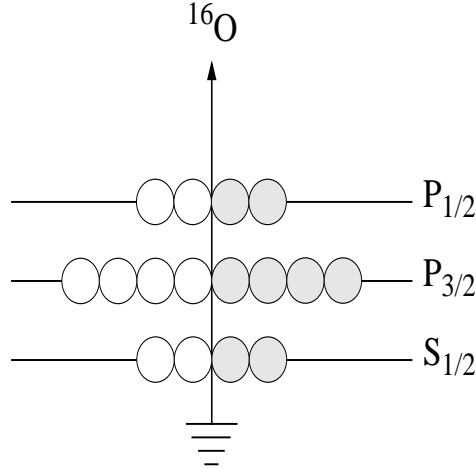


Figure 1-6: Shell model for  $^{16}\text{O}$  (energy levels not to scale).

#### 1.4.1 Previous Experiments

Quasielastic  $^{16}\text{O}(e, e'p)$  experiments have been previously performed at NIKHEF, Saclay, and Mainz in various kinematics.

Figure 1-7 shows the longitudinal-transverse interference response function  $R_{LT}$  for  $1p_{1/2}$  and  $1p_{3/2}$  states measured by Chinitz *et al.* [8] ( $T_p = 160$  MeV,  $Q^2 = 0.30$  (GeV/c) $^2$ ) at Saclay, and by Spaltro *et al.* [9] ( $T_p = 84$  MeV,  $Q^2 = 0.20$  (GeV/c) $^2$ ) at NIKHEF. The curves are the corresponding standard non-relativistic DWIA calculations.

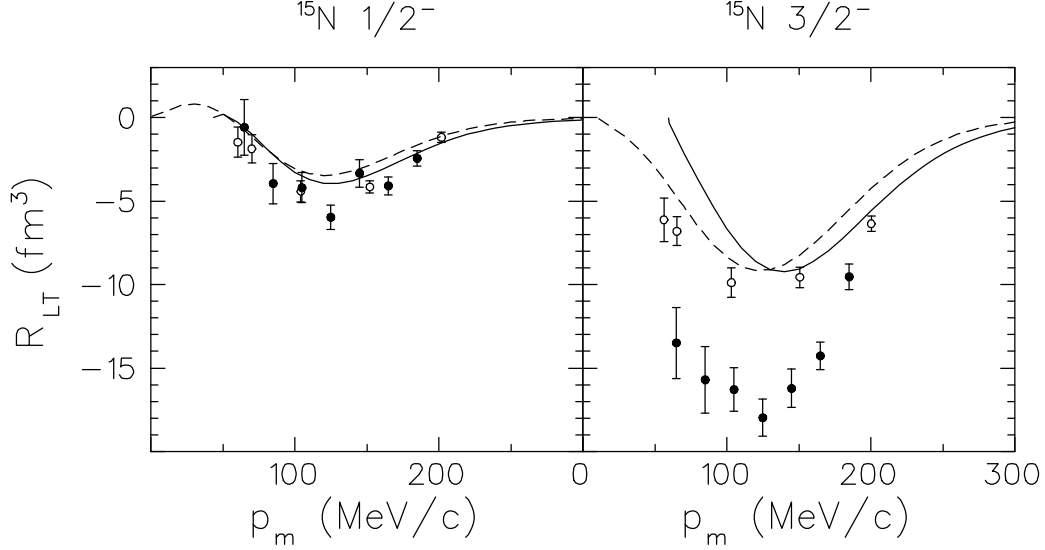


Figure 1-7: Comparison of the longitudinal-transverse interference response function with DWIA calculations. The final state interaction is described by the Schwandt optical potential [10]. Bound state wave functions and spectroscopic factors are fitted to the data obtained by Leuschner *et al.* [11]. Open circles (Chinitz *et al.* [8]) and dashed lines are for  $T_p = 160$  MeV,  $Q^2 = 0.30$  (GeV/c)<sup>2</sup>; solid circles (Spaltro *et al.* [9]) and solid lines are for  $T_p = 84$  MeV,  $Q^2 = 0.20$  (GeV/c)<sup>2</sup>.

These calculations use the Schwandt optical potential [10] and the overlap parameters fitted to the data obtained by Leuschner *et al.* [11] in parallel kinematics. The spectroscopic factors from this fit are 0.70 for  $1p_{1/2}$  state, and 0.60 for  $1p_{3/2}$  state. For  $1p_{1/2}$  state, the calculations agree with the data reasonably well; however, for  $1p_{3/2}$  state, the calculation at  $T_p = 84$  MeV has to be scaled by a factor of two to fit the data, while the corresponding factor at  $T_p = 160$  MeV is close to unity. Spaltro *et al.* [9] pointed out that the difference for  $1p_{3/2}$  state between the two data sets is actually larger than this estimate because the data of Chinitz *et al.* [8] include an unresolved contribution from the  $(1s, 2d)$  doublet, estimated to be about 10%. This implies that there is a deficiency in the DWIA model of the  $R_{LT}$  response function which depends strongly upon nuclear structure and which appears to decrease with

increasing  $Q^2$ .

The data from Chinitz *et al.* [8] and Spaltro *et al.* [9] have been compared with the DWIA calculations of Kelly [33] (see Section 4.2).

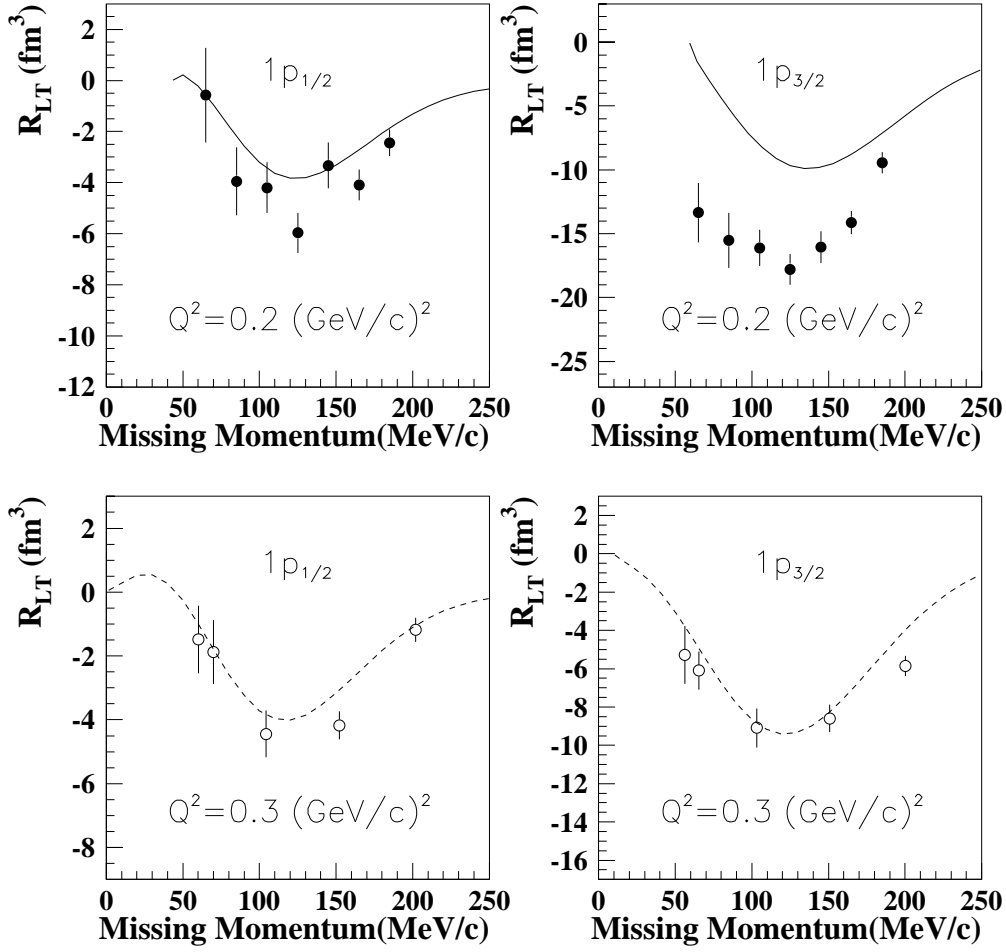


Figure 1-8: Comparison of the longitudinal-transverse interference response function with the DWIA calculations of Kelly [33]. Open circles (Chinitz *et al.* [8]) and dashed lines are for  $T_p = 160 \text{ MeV}$ ,  $Q^2 = 0.30 \text{ (GeV/c)}^2$ ; solid circles (Spaltro *et al.* [9]) and solid lines are for  $T_p = 84 \text{ MeV}$ ,  $Q^2 = 0.20 \text{ (GeV/c)}^2$ .

The DWIA calculations of Kelly in Figure 1-8 used the EDAD1 [20] optical potential. The spectroscopic factors were 0.75 for the  $1p_{1/2}$  state and 0.64 for the  $1p_{3/2}$  state. They were determined from the data of Leuschner *et al.* [11]. Figure 1-8 shows the same feature as Figure 1-7: for the  $1p_{1/2}$  state, the calculations agree with the data reasonably well; however, for the  $1p_{3/2}$  state, the calculation at  $T_p = 84$  MeV has to be scaled by a factor of two to fit the data, while the calculation at  $T_p = 160$  MeV is consistent with the data.

Van der Sluys *et al.* [12] calculated  $R_{LT}$  for  $^{16}\text{O}(e, e'p)$  with two-body currents included. In these calculations, the final-state interaction between the outgoing nucleon and the residual nucleus is handled in a self-consistent Hartree-Fock random phase approximation formalism [13] [14]. After being corrected for differences between the normalization conventions employed for the calculations and conventions used to analyze the data [6], these calculations are compared with data in Figure 1-9.

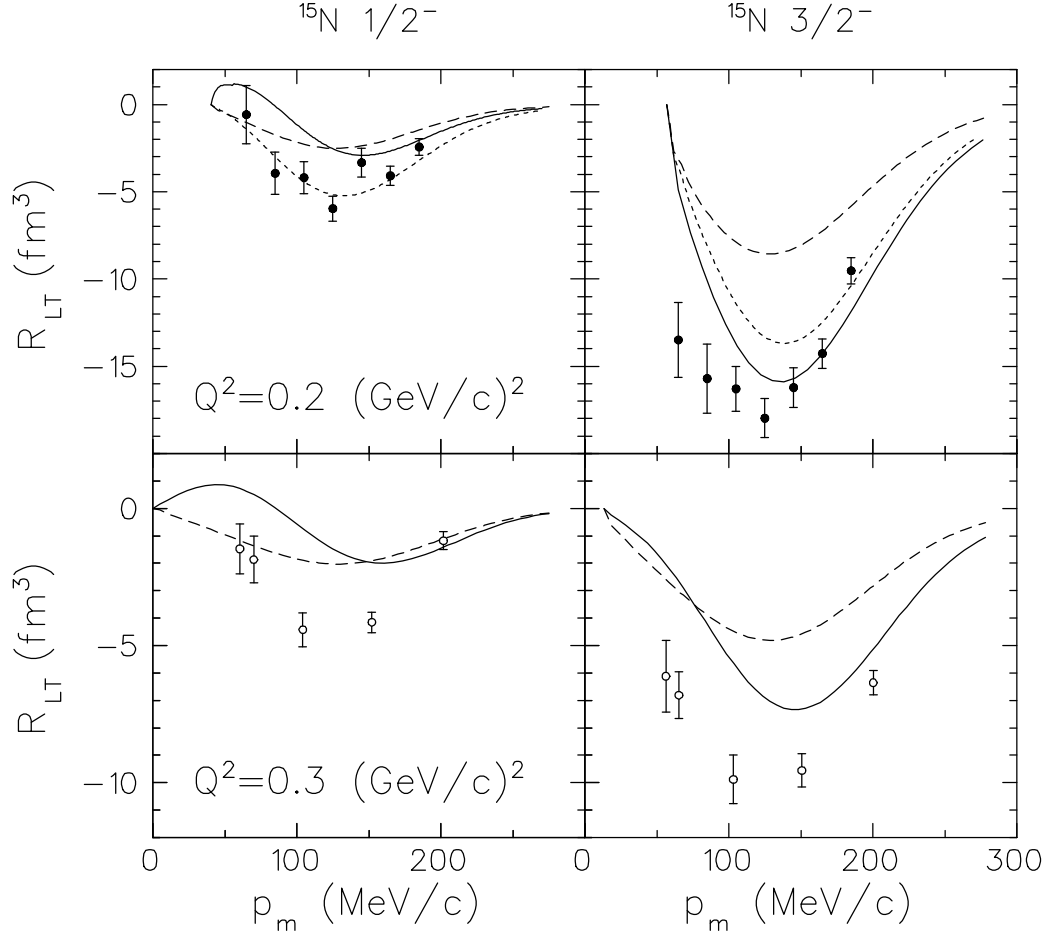


Figure 1-9: Comparison of  $R_{LT}$  calculations from Van der Sluys *et al.* [12] with the data. Open circles (Chinitz *et al.* [8]) and dashed lines are for  $T_p = 160 \text{ MeV}$ ,  $Q^2 = 0.30 \text{ (GeV/c)}^2$ ; solid circles (Spaltro *et al.* [9]) and solid lines are for  $T_p = 84 \text{ MeV}$ ,  $Q^2 = 0.20 \text{ (GeV/c)}^2$ . Dashed lines are DWIA calculations, dotted lines (top row) include MEC contributions, and solid lines include both MEC and IC contributions. The final state interaction in the DWIA calculations is described with a self-consistent Hartree-Fock random phase approximation [13] [14]. The spectroscopic factors are 85% for  $Q^2 = 0.2 \text{ (GeV/c)}^2$  and 60% for  $Q^2 = 0.3 \text{ (GeV/c)}^2$  of those obtained using the standard DWIA calculations.

Notice that in this model, the two-body current has the opposite affect upon  $R_{LT}$  for the spin-orbit partners, enhancing  $R_{LT}$  for  $1p_{3/2}$  state and suppressing it for  $1p_{1/2}$

state. Although the net effect is substantially larger for the  $1p_{3/2}$  state, it is still not enough to reproduce the observed enhancement at  $Q^2 = 0.3 \text{ (GeV/c)}^2$ . Also, in this model, the contribution from the one-body current has more  $Q^2$  dependence than that in the standard DWIA calculations shown in Figure 1-7. The spectroscopic factors are only 85% for  $Q^2 = 0.2 \text{ (GeV/c)}^2$  and 60% for  $Q^2 = 0.3 \text{ (GeV/c)}^2$  of those obtained using the standard DWIA calculations. This indicates that the Hartree-Fock random phase approximation does not adequately represent the energy dependence of absorptive process [6].

At Mainz, the  $^{16}\text{O}(e, e'p)$  cross section has been measured and the distorted momentum distribution

$$n^D = \sigma_{(e, e'p)} / K \sigma_{cc1} \quad (1.31)$$

has been obtained in parallel kinematics by Blomqvist *et al.* [15].  $\sigma_{cc1}$  is the  $ep$  off-shell cross section [7]. The proton kinetic energies were  $\sim 93 \text{ MeV}$  and  $\sim 215 \text{ MeV}$ .

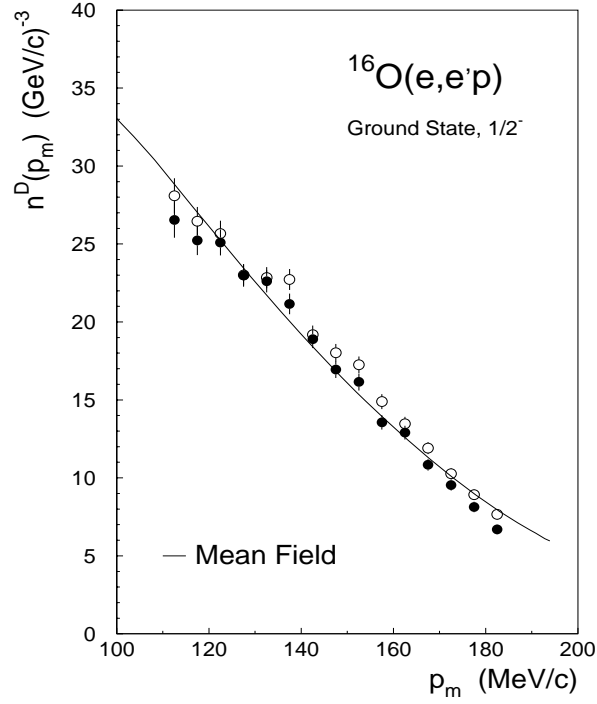


Figure 1-10:  $^{16}\text{O}(e, e'p)$  distorted momentum distribution for the  $1p_{1/2}$  state measured at Mainz [15]. The kinetic energy is  $\sim 93$  MeV. The curve is a DWIA calculation which uses a Woods-Saxon potential with parameters fit from the NIKHEF data [16], and the Schwandt optical potential [10] for final state interactions.

The spectroscopic factor deduced from Figure 1-10 is in excellent agreement with the NIKHEF measurement. This indicates that the absolute normalization of both experiments agrees at kinetic energy  $\sim 90$  MeV.

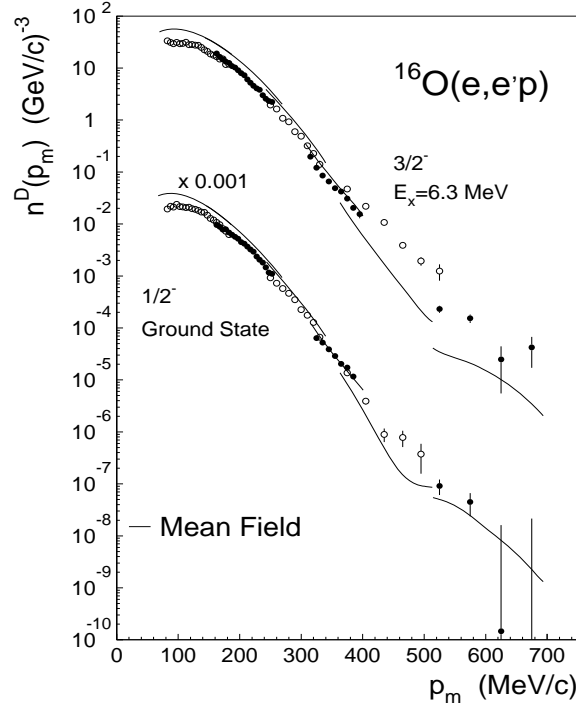


Figure 1-11:  $^{16}\text{O}(e, e'p)$  distorted momentum distributions for  $1p$  states measured at Mainz [15]. The alternating groups of solid versus open symbols correspond to successive kinematic settings. The kinetic energy is  $\sim 215$  MeV. The DWIA calculations use the spectroscopic factors and parameters for a Woods-Saxon bound-state as determined by Leuschner *et al.* [11] The final state interaction is described by the optical potential of Schwandt *et al.* [10]

Figure 1-11 shows  $^{16}\text{O}(e, e'p)$  distorted momentum distribution for the  $1p$  states at kinetic energy  $T_p \sim 215$  MeV. There is a large discrepancy between the data and the DWIA calculations which treat the final state interaction with the optical potential of Schwandt *et al.*[10] The Schwandt parametrization is obtained by fitting proton elastic scattering data with  $T_p < 180$  MeV and  $A > 23$ . Although this optical potential can reconstruct the data with  $T_p \sim 90$  MeV very well, it fails to explain the data at  $T_p \sim 215$  MeV. This indicates the  $T_p$ -extrapolation of the Schwandt optical potential might be problematic.

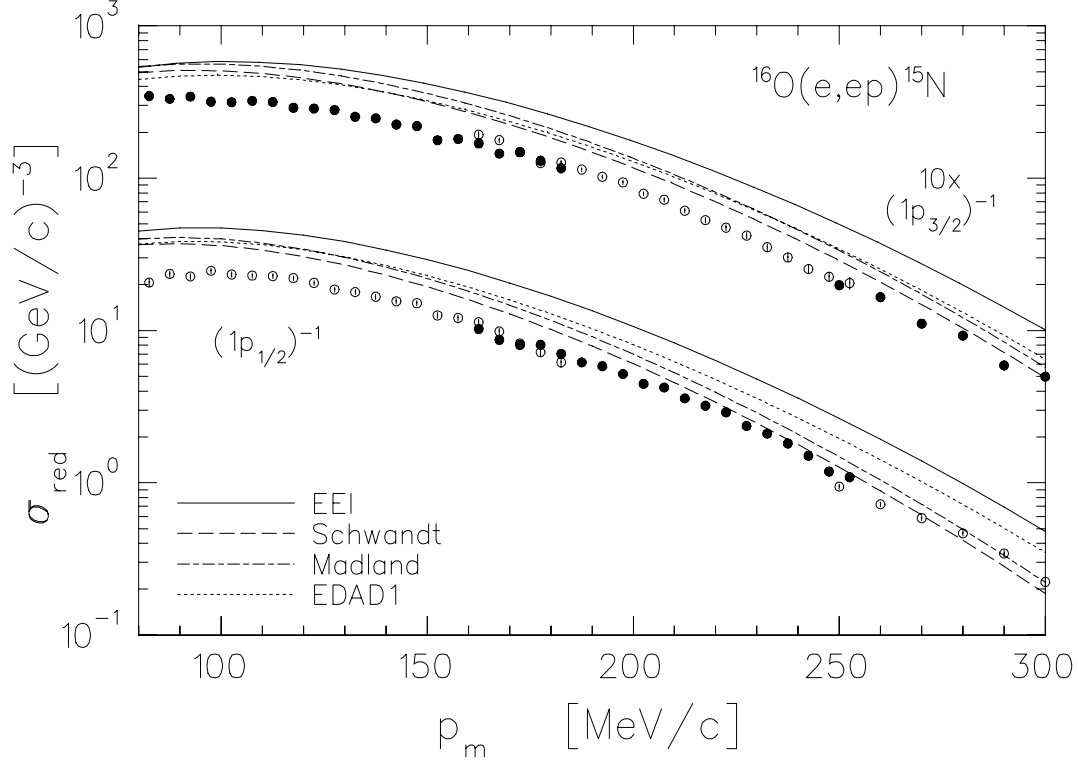


Figure 1-12: Comparison of  $^{16}\text{O}(e, e'p)$  distorted momentum distributions obtained at Mainz with DWIA calculations [17]. The proton kinetic energy is  $\sim 215$  MeV. The DWIA calculations use the overlap functions and spectroscopic factors fitted from data of Leuschner *et al.* [11]. The optical potentials are EEI [18] for the solid, Schwandt [10] for the long dashed, Madland [19] for the dot-dashed, and EDAD1 [20] for the dotted lines respectively.

The Mainz  $^{16}\text{O}(e, e'p)$  distorted momentum distribution ( $T_p \sim 215$  MeV) has been compared to DWIA calculations using different optical potentials in Figure 1-12. The DWIA calculations used the overlap functions as well as spectroscopic factors fitted from data of Leuschner *et al.* [11]. The optical potentials include EEI [18], Schwandt [10], Madland [19] and EDAD1 [20]. The EDAD1 potential is fit by Cooper *et al.* [20] using Dirac phenomenology, the Schwandt potential [10] is fit to proton elastic scattering for  $A \geq 40$  and  $80 \leq T_p \leq 180$  MeV, the EEI potential [18] is a folding model potential based upon an empirical effective interaction fit to proton-nucleus

elastic and inelastic scattering data at 200 MeV, and the Madland potential [19] is a variation of the Schwandt potential that extends the upper limit of  $T_p$  from 180 MeV to 400 MeV and the lower limit of  $A$  from 40 to 12. A detailed comparison of these potentials is available in [21]. All the calculations overestimate the peak of the missing momentum distribution and must be scaled by a factor of about 0.5-0.6 to reproduce the data for low missing momentum. This suggest that effects beyond the standad non-relativistic DWIA, such as two-body currents or relativistic effects, may play an important role even in the quasielastic region.

### 1.4.2 This Experiment

Experiment E89-003 in Hall A at Jefferson Laboratory studied quasielastic  $1p$ -shell proton knockout from  $^{16}\text{O}$  at  $Q^2 = 0.8 \text{ (GeV/c)}^2$ . So far, this is the only  $^{16}\text{O}(e, e'p)$  data set available at such high  $Q^2$ . It provides tests for different optical potentials and helps to understand the effects beyond standard non-relativistic DWIA. The data for cross sections have been acquired at three nominal beam energies, 845 MeV, 1645 MeV and 2445 MeV to separate response functions  $R_{L+TT}$ ,  $R_T$ , and  $R_{LT}$  for the  $1p$  states.  $\omega = 445 \text{ MeV}$ ,  $Q^2 = 0.8 \text{ (GeV/c)}^2$ , and  $T_p = 427 \text{ MeV}$  were kept constant during the experiment. At each beam energy, the momentum and angle of the electron arm were fixed, while the angle of the hadron arm with respect to the direction of  $\vec{q}$  was changed to map out the missing momentum. The kinematics of this experiment is summarized in Table 1.1 and diagrammed in Figure 1-13.

$E_{beam}$ (MeV)	$\theta_e$ ( $^\circ$ )	$\theta_{pq}$ ( $^\circ$ )	$P_{miss}$ (MeV/c)
845	100.7	0	0
845	100.7	8	140
845	100.7	16	275
1645	37.17	-8	140
1645	37.17	0	0
1645	37.17	8	140
2445	23.38	-20	350
2445	23.38	-16	275
2445	23.38	-8	140
2445	23.38	0	0
2445	23.38	8	140
2445	23.38	16	275
2445	23.38	20	350

Table 1.1: Kinematics settings for E89-003:  $\omega = 439$  MeV,  $Q^2 = 0.8$  (GeV/c) $^2$ , and  $T_p = 427$  MeV.

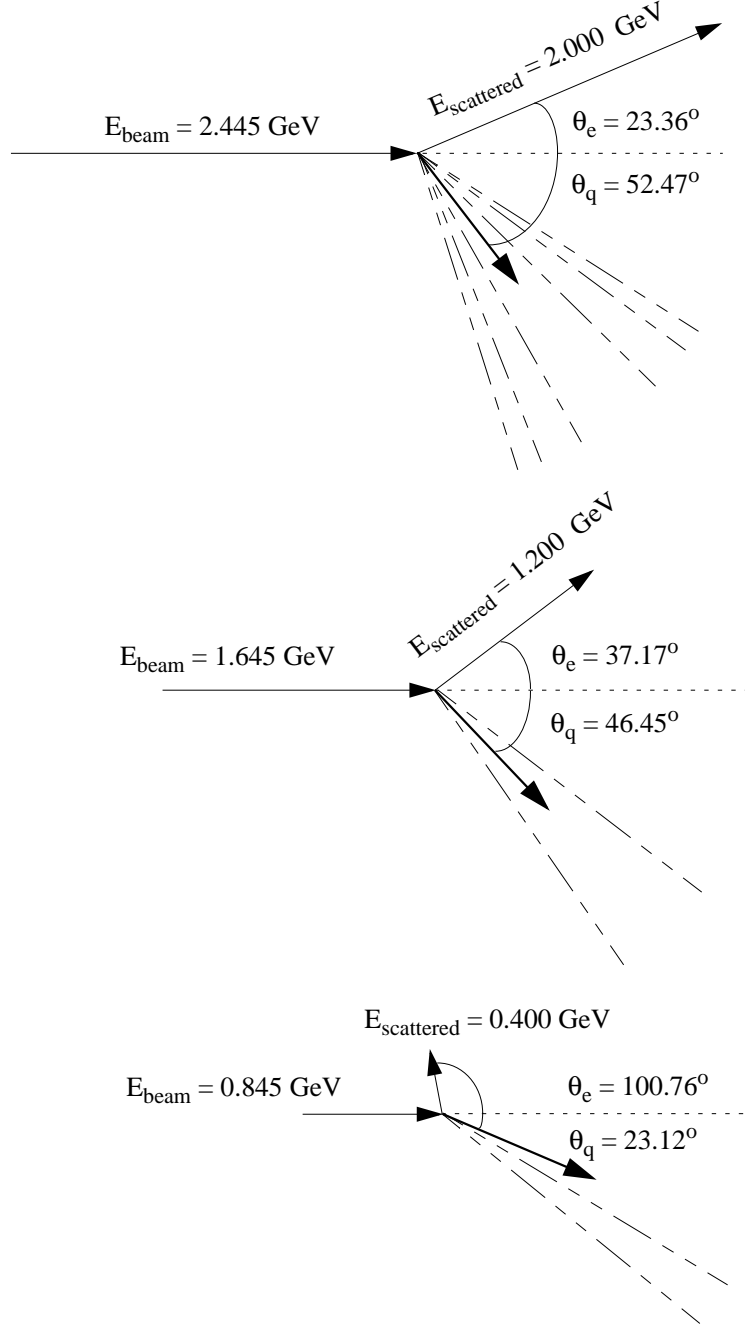


Figure 1-13: A schematic display of the E89-003 kinematics settings. Three nominal beam energies (845 MeV, 1645 MeV, 2445 MeV) were employed to separate the response functions  $R_L + \frac{V_{LT}}{V_L} R_{TT}$ ,  $R_{LT}$  and  $R_T$ .  $\omega$ ,  $Q^2$ , and  $T_p$  were fixed. At each beam energy, the momentum and angle of the electron arm was fixed, and the angle between the  $\vec{q}$  and  $\vec{p}_p$  was changed to map out the missing momentum.

## Chapter 2

# The Experimental Setup

### 2.1 Overview

In the summer of 1997, experiment E89-003 (*A Study of the Quasielastic  $^{16}\text{O}(e,e'p)$  Reaction at High Recoil Momenta* [22]) was performed in Hall A at Jefferson Laboratory (formerly called CEBAF). This laboratory is located in Newport News, Virginia. The accelerator was designed to produce high current, 100% duty factor beams of up to 4 GeV to three independent and complementary experimental halls (A, B, and C). In Hall A, two basically identical 4 GeV/c high resolution spectrometers (HRSE and HRSH) are used to detect scattered electrons and knocked-out protons respectively. The detector packages are installed on the focal plane of each spectrometer to detect the particle trajectories as well as identify the particles. To study  $^{16}\text{O}$ , a waterfall target with three waterfall foils built by the INFN group [23] was used.

### 2.2 Accelerator

The layout of the accelerator is shown in Figure 2-1.

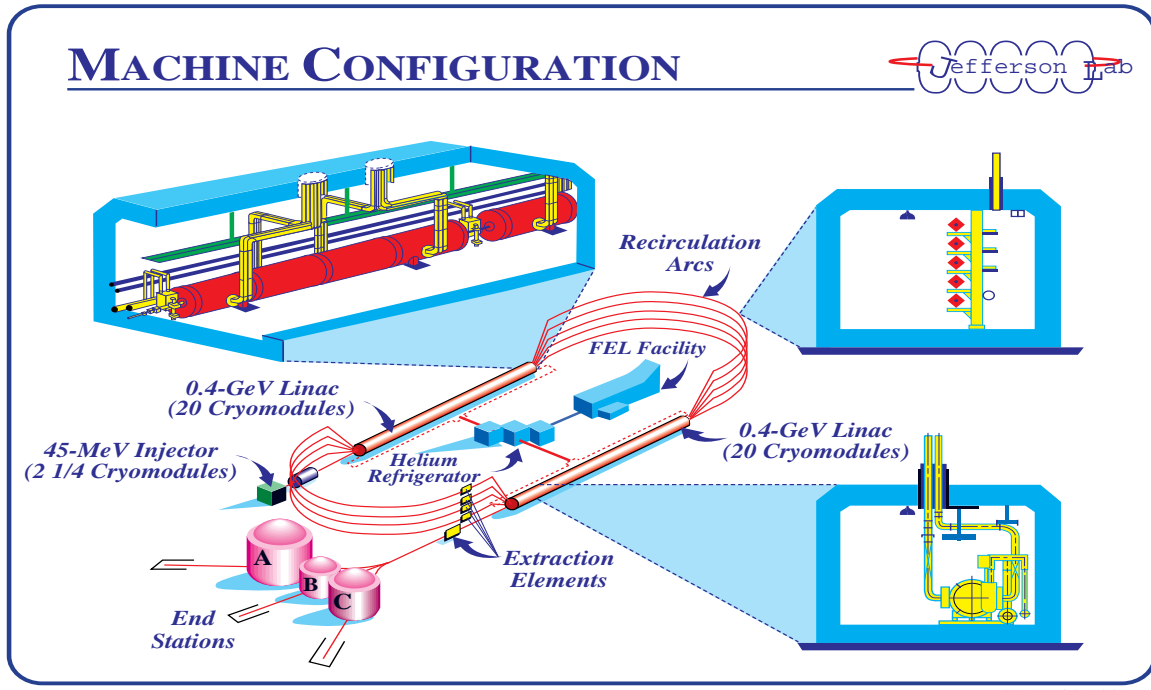


Figure 2-1: Accelerator configuration.

The electron beam is accelerated to 45 MeV in the injector before passing through a linac consisting of superconducting RF cavities where it acquires additional 400 MeV. After undergoing a  $180^\circ$  bend in the recirculation arc, the beam passes through another linac to gain 400 MeV more. At this point, the beam can be either extracted and directed into any of the three halls, or sent back for additional acceleration in the linacs. A grand total of 5 passes are available to each electron. The final beam energy is thus 45 MeV plus 800 MeV times the number of passes, up to 4045 MeV. The machine can also deliver non-standard beam energies (the energy per pass is different from 800 MeV), but the ultimate energy of the beam is always a multiple of the combined linac energies plus the initial injector energy.

There are five different arcs for recirculation on one end of the machine, and on the other end, there are four different arcs. The bending field of each arc is set to bend

the beam of a different pass; that is, beam of different energy. The beam is separated at the end of each linac, sent to the corresponding arc, and then recombined before entering the next linac. At the end of the acceleration process, the beam is extracted and then delivered to the experimental halls.

The beam has a microstructure that consists of short pulses at a frequency of 1497 MHz. Generally, each hall receives one third of the pulses, resulting in a quasi-continuous train of pulses at a frequency of 499 MHz. Beams with different energies can be delivered into the halls simultaneously.

The beam characteristics at the time of E89-003 are summarized in Table 2.1.

Maximum energy	4.045 GeV
Duty cycle	100%, CW
Emittance	$2 \times 10^{-9}$ m
Energy spread ( $4\sigma$ )	$10^{-4}$
Maximum intensity	200 $\mu$ A
Vertical size ( $4\sigma$ )	100 $\mu$ m
Horizontal size ( $4\sigma$ )	500 $\mu$ m

Table 2.1: Jefferson Laboratory beam characteristics.

In this experiment, three nominal beam energies (845 MeV, 1645 MeV and 2445 MeV) were employed for the response function separation. The typical unpolarized CW beam current was 70  $\mu$ A.

## 2.3 Hall A Setup

The basic configuration of Hall A is shown in Figure 2-2.

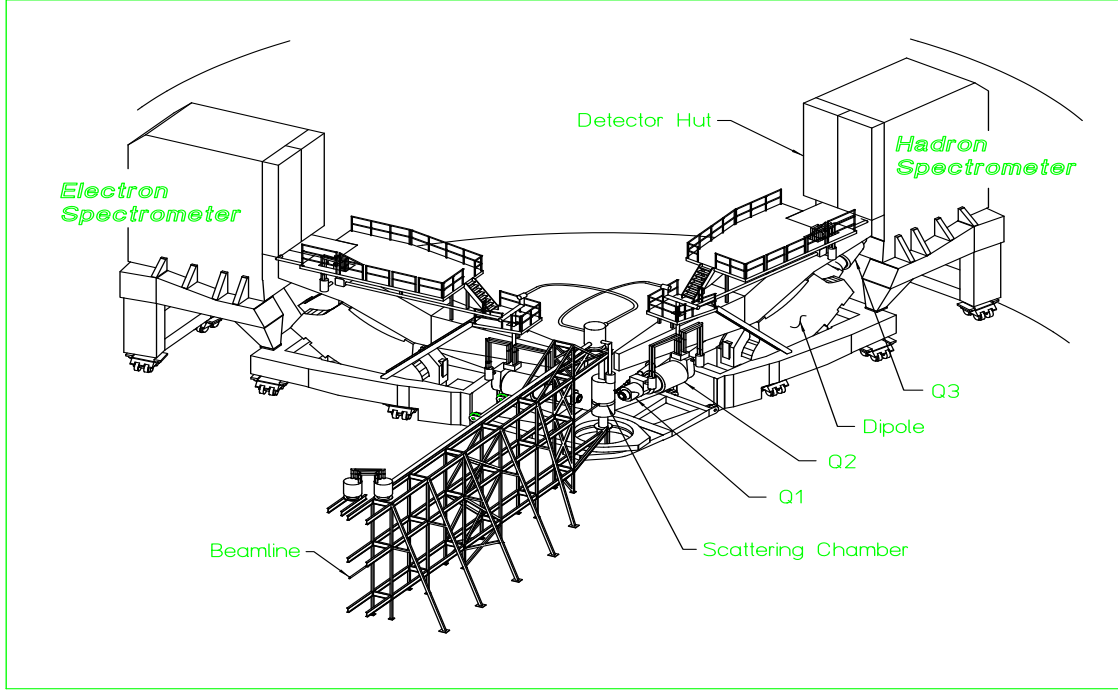


Figure 2-2: Hall A configuration.

After being extracted for use in Hall A, the electron beam is transported into the hall along the beamline, and onto the scattering chamber where the target is sitting. Along the beamline, there are two BCMs (Beam Current Monitors, see Section 2.4.1) and two BPMs (Beam Position Monitors, see Section 2.4.2) which provide precise measurements of beam current and position. The majority of the electrons incident upon the target pass through without interacting and are transported to a well-shielded beam dump. Two spectrometers (see Section 2.6) are used to perform physics experiments. The electron spectrometer (HRSE) measures the momentum and direction of the scattered electrons, and similarly, the hadron spectrometer (HRSH) detects the knocked-out protons. The two spectrometers are essentially identical in terms of the magnetic components and optics. Note that by changing the polarities of the magnets, their roles can be interchanged. On the platform of each spectrometer, a

shielding house (detector hut) has been built to prevent the detector packages and associated electronics from radiation damage, and to minimize the rates in detectors caused by particles not passing through the spectrometer.

## 2.4 Beamline

### 2.4.1 Beam Current Monitors

The beam current delivered to Hall A was measured by two Beam Current Monitors (BCMs) placed in the beamline about 24.5 meters upstream of the target. A BCM is simply a cylindrical resonant cavity made out of stainless steel, 15.48 cm in diameter and 15.24 cm in length. The resonant frequency of each cavity is adjusted to 1497 MHz, which matches the frequency of the CEBAF beam. Inside each cavity there are two loop antennas coaxial to the cavity. The large one has a radius that couples it to the one of the resonant modes of the cavity and is located where the  $\vec{H}$  field is largest. This antenna is used to couple the beam signal out of the cavity. The smaller antenna is used to periodically test the response of the cavity by sending through it a 1497 MHz calibration signal from a current source and detecting the induced current in the large antenna. When the electron beam passes through the cavity, it excites the resonant transverse electromagnetic modes  $TM_{010}$  at 1497 MHz. The large area probe loop provides an output signal that is proportional to the current.

The BCMs require an absolute calibration which is provided by an Unser monitor [24] sandwiched between them (see Figure 2-3). The Unser uses a Direct Current Transformer composed of two identical toroidal cores driven in opposite ways by an external source. In the absence of any current, the sum of the output signals from the sense windings around each core is zero. A DC-current passing through the cores produces a flux imbalance, and thus an output signal is achieved. The Unser is calibrated by passing current along a wire that is placed through the device to

simulate the beam current. This reference current is generated by a high-precision current source. Once the Unser is calibrated, it can be used to calibrate the BCMs. The underlying philosophy of the BCM calibration procedure is to transform the precise knowledge of the beam current from the Unser to the BCM cavities. This is performed over a time interval of 10 minutes during which five steps of beam on/off are executed. The BCM cavities have excellent linearity over a large dynamical range and are therefore able to serve as accurate relative current monitors. Since an overall uncertainty of about 250 nA in the Unser measurement stays constant, the relative error of the current measurement is less when the BCM cavities are calibrated at a higher current.

Because the BCM output signals have a high frequency of 1497 MHz, they also have a high attenuation. For this reason, a down-converter is installed close to each cavity to transform the 1497 MHz signals to 1 MHz signals. These 1 MHz signals are then filtered, amplified, and sent to digital multimeters. Sampled signals are taken from the 1-second average of the BCM output every 4-, 10-, and 50-seconds. They are all sent to a common ADC which sits in a VME crate in the counting house. The 4-second and 50-second samples are recorded into the data stream as EPICS (Experimental Physics and Industry Control System) events, while the 10-second signal is recorded into the Accelerator Archiver. In addition, during this experiment, the voltage signals from the downstream BCM were converted to frequency via a Voltage-to-Frequency (VtoF) converter providing a signal that was integrated over 10 seconds and passed to a run-gated scaler. The VtoF signal, calibrated using the 10-second corrected data, provided the most accurate charge determination. A detailed discussion about measuring accumulated charge during this experiment is available in [25].

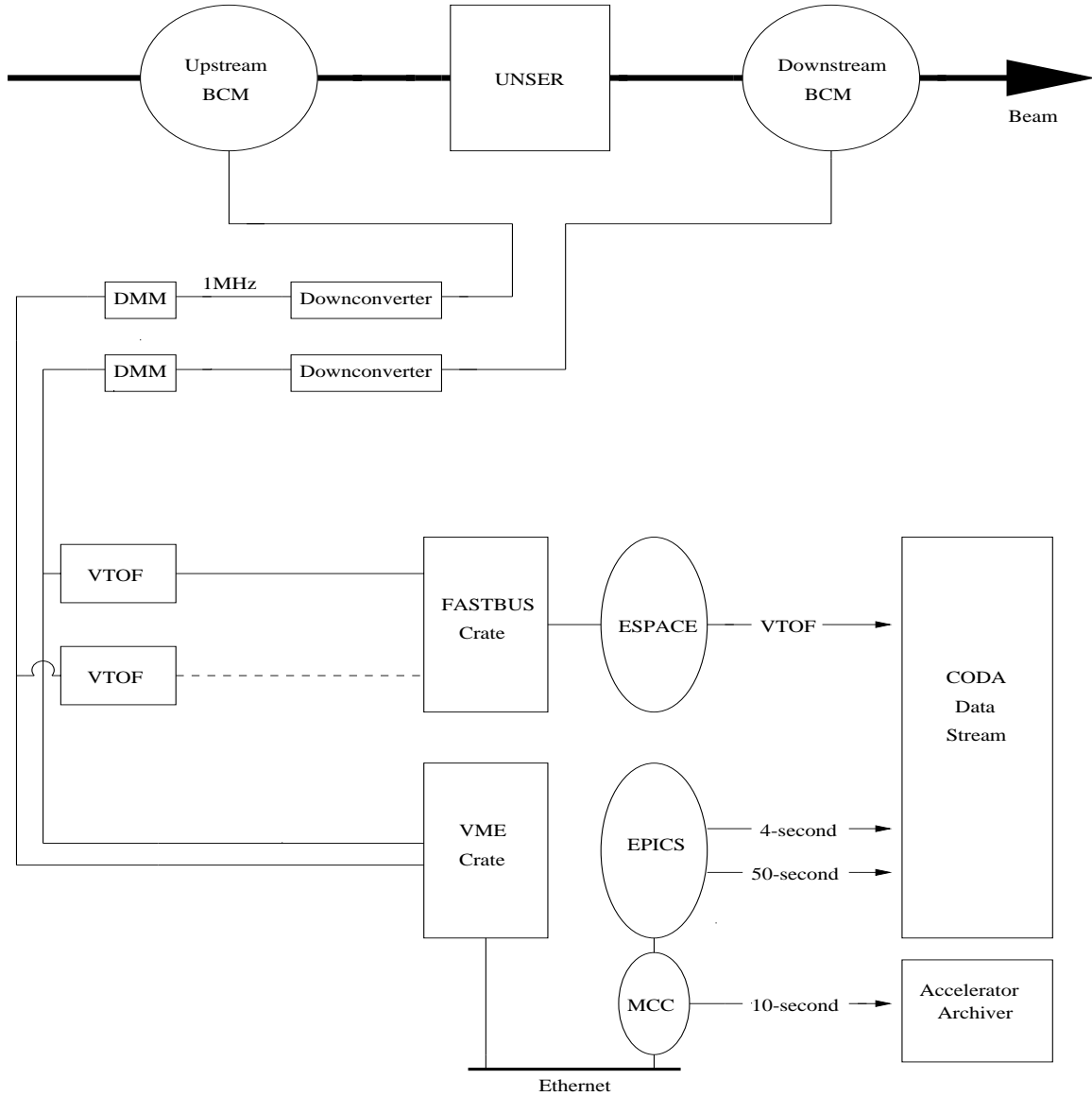


Figure 2-3: A diagram of the charge determination in E89-003.

### 2.4.2 Beam Position Monitors

The position of the beam along the Hall A beamline was monitored using two beam position monitors (BPMs) upstream of the target along the beamline. These two

BPMs are 6 m apart, and the one closer to the target is about 1 m away from the target. A BPM is simply a cavity with four antennae rotated  $\pm 45^\circ$  from the horizontal and vertical directions. The signal picked up by each antenna from the fundamental frequency of the beam is inversely proportional to the distance between the beam and the antenna. The beam position is thus the difference over the sum of the properly normalized signals from two antennae on opposite sides of the beam. At a beam current of 10  $\mu\text{A}$ , the beam position can be determined down to 20  $\mu\text{m}$ . From the information provided by the two BPMs, one can figure out both the beam position on the target and the beam direction.

During this entire experiment, the beam was required to be within 150  $\mu\text{m}$  of the center of the beamline at the BPM closer to the target, and within 1 mm of the center of the beamline at the other BPM. This kept the beam position on the target to within 200  $\mu\text{m}$  of the center of the beamline, and the angle between the beam direction and beamline axis to be less than 0.15 mrad.

## 2.5 High Resolution Spectrometer

In order to separate the closely-spaced nuclear final states and to control the systematic uncertainties in the study of  $(e, e'p)$  reactions, the Hall A spectrometers were designed to have high resolution in the determination of particle momentum, position, and angle. Each of the high resolution spectrometers consists of three  $\cos 2\theta$  quadrupoles (Q1, Q2 and Q3) and one dipole (D). The magnets are superconducting and arranged in the QQDQ configuration shown in Figure 2-4. The bending angle is  $45^\circ$  in vertical plane. The momentum range of the spectrometer is from 0.3 GeV/c to 4 GeV/c. The momentum acceptance is  $\sim 9\%$ , and the momentum resolution is  $10^{-4}$ .

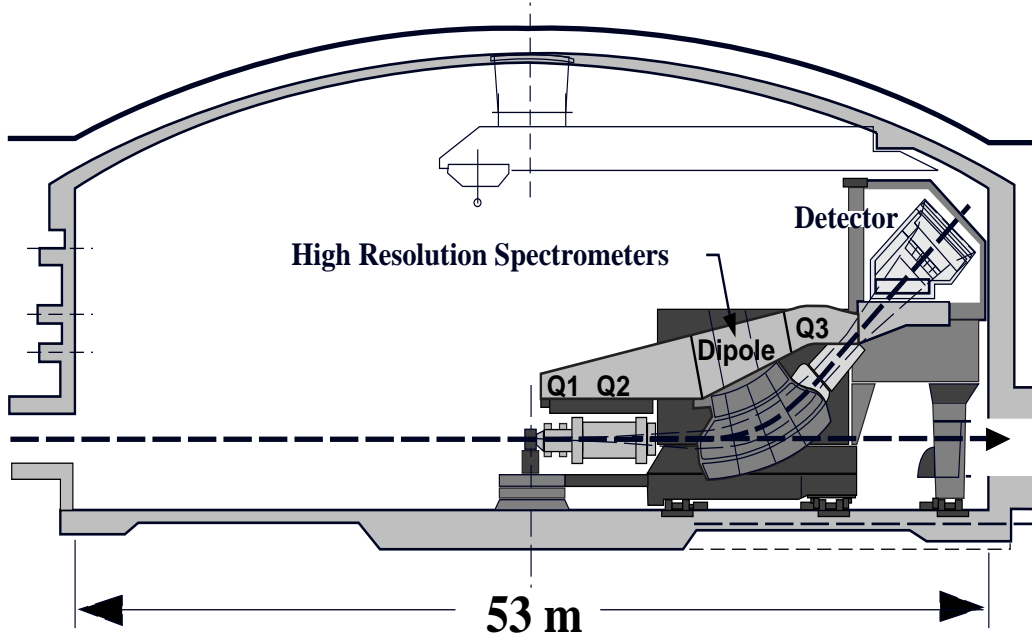


Figure 2-4: Hall A High Resolution Spectrometer.

Each spectrometer is point-to-point in the dispersive direction. Q1 is convergent in the dispersive (vertical) plane. Q2 and Q3 provide transverse focusing. The dipole which bends the charged particles has its entrance and exit both inclined at  $30^\circ$  with respect to the central axis [26]. The magnetic field of the dipole increases with the radial distance, which provides a natural focusing in the dispersive direction. The main characteristics of the spectrometer are listed in Table 2.2.

Bending angle	45°
Optical length (m)	23.4
Momentum range (GeV/c)	0.3 to 4
Momentum acceptance (%)	$\pm 4.5$
Momentum dispersion (cm/%)	11.76
Momentum resolution (FWHM)	$2.5\text{-}4.0 \times 10^{-4}$
Horizontal angular acceptance (mr)	$\pm 25$
Transverse angular acceptance (mr)	$\pm 50$
Horizontal FWHM angular resolution (mr)	1.0
Transverse FWHM angular resolution (mr)	2.0
Transverse position acceptance (cm)	$\pm 5\text{cm}$
Transverse position FWHM resolution (mm)	2.0

Table 2.2: Main characteristics of a High Resolution Spectrometer.

## 2.6 Detector Packages

The detector packages for the HRSE and the HRSH are shown in Figures 2-5 and 2-6. On the HRSE, there are two scintillator planes (S1 and S2) which provide an event trigger and time-of-flight information. Two Vertical Drift Chambers (VDCs) are paired to precisely locate the trajectories of the charged particles passing through the focal plane. The Gas Cerenkov detector is for  $e^-/\pi^-$  separation. The HRSH detector package is similar to that of HRSE, but there is no Gas Cerenkov detector on the HRSH.

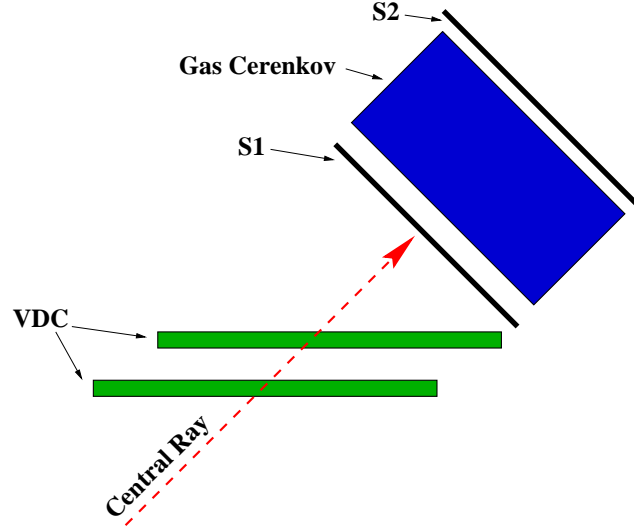


Figure 2-5: HRSE detector package. The Vertical Drift Chambers (VDCs) detect the trajectories of charged particles, scintillator planes (S1 and S2) are for trigger and time-of-flight information, and the  $\text{CO}_2$  gas Cerenkov detector is for  $e^-/\pi^-$  separation.

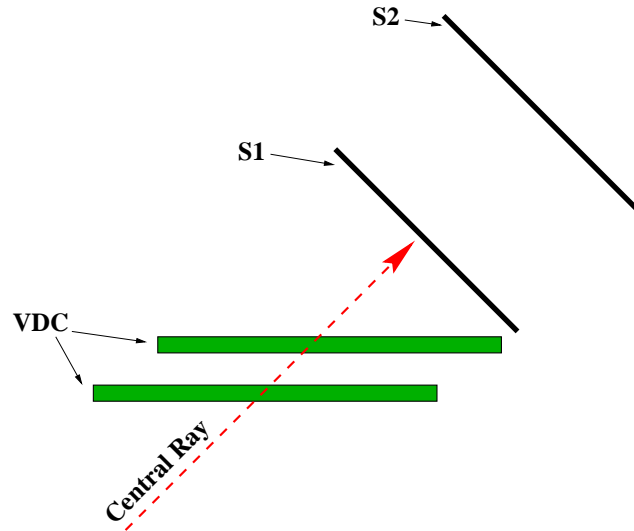


Figure 2-6: HRSB detector package. It is similar to that of HRSE, but there is no Gas Cerenkov detector on the HRSB.

### 2.6.1 Scintillators

The scintillator plane S1 is located 1.5 m downstream of the center of the first VDC. The distance between S1 and S2 is about 2 meters. Each scintillator plane is segmented and consists of 6 paddles with 0.5 cm overlap. The active area of S1 is about  $170 \text{ cm} \times 35 \text{ cm}$ , while the active area of the scintillator plane S2 is about  $220 \text{ cm} \times 54 \text{ cm}$ . At each side of each paddle, a 2-inch phototube is mounted to generate signals that are sent to both an Analog-Digital Converter (ADC) and a Time-Digital Converter (TDC).

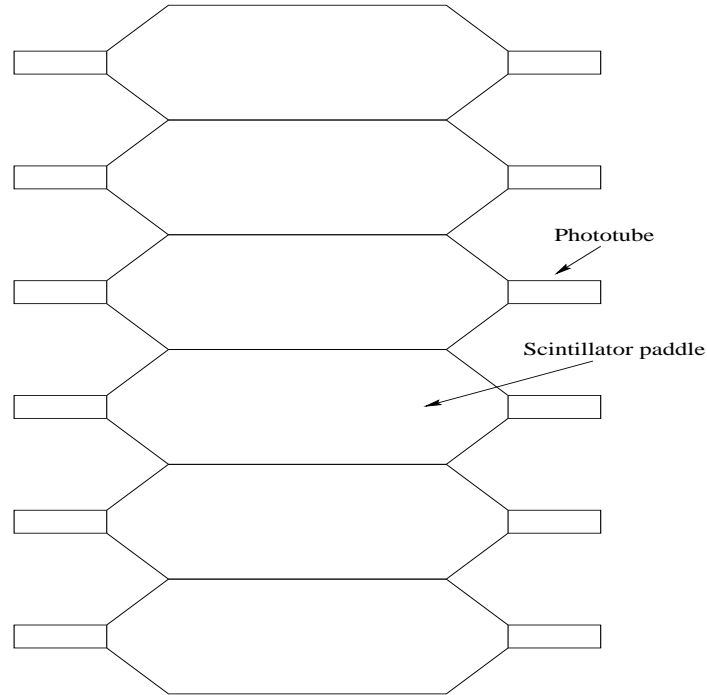


Figure 2-7: A schematic display of the scintillator plane. Each scintillator plane has six paddles. A phototube is installed at each side of each paddle.

### 2.6.2 Vertical Drift Chambers

Within the detector package of each spectrometer, there are two paired vertical drift chambers (VDCs [27]) which determine the trajectories of the charged particles at the focal plane. Figure 2-8 and 2-9 show how these two VDCs are positioned. As can be seen, they are identical and parallel to each other. The bottom one is placed near the actual focal plane. The top one is about 35 cm above the bottom chamber, and shifted by about 35 cm with respect to the bottom one in the dispersive direction. The size of each VDC is about  $240 \text{ cm} \times 40 \text{ cm} \times 10 \text{ cm}$ . The active area is  $211.8 \text{ cm} \times 28.8 \text{ cm}$ . The nominal central ray is within 0.5 cm of the center of the bottom VDC.

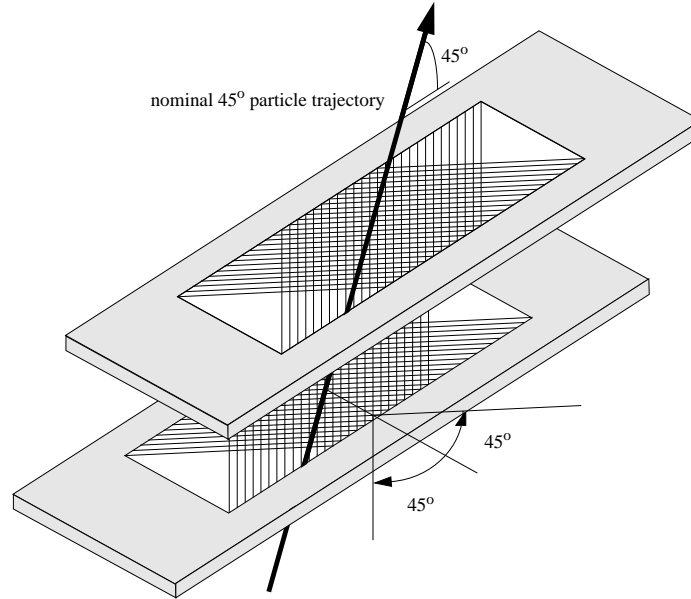


Figure 2-8: A schematic layout of the VDC pair (not to scale). There are four wire planes for each VDC pair. Each wire plane has 368 signal wires.

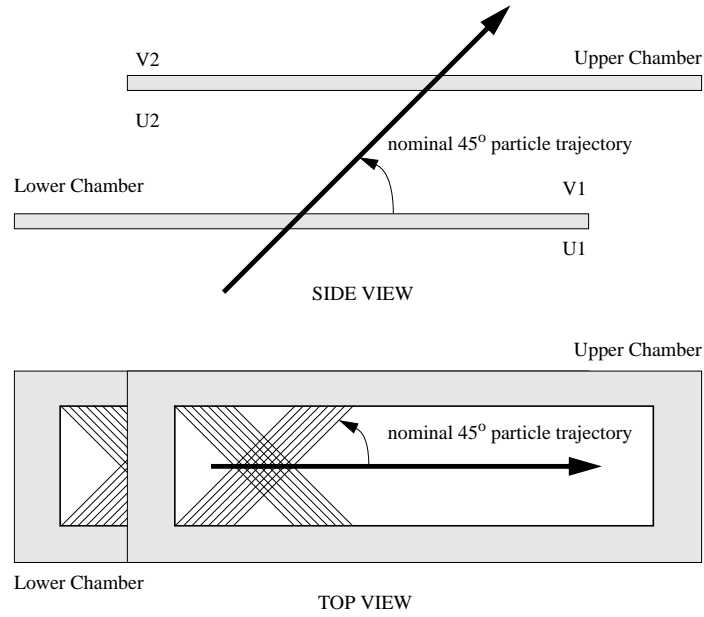


Figure 2-9: Side view and top view of VDC pair (not to scale).

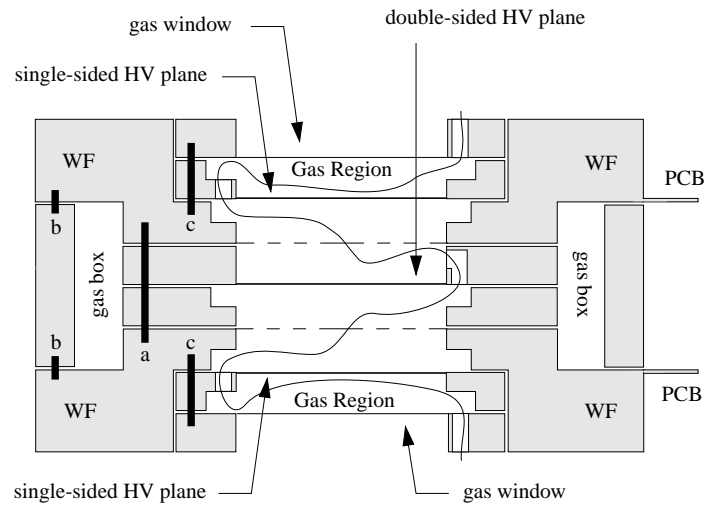


Figure 2-10: VDC cross-sectional view (not to scale).

Each VDC consists of two gas windows, two wire planes, and three high voltage

(HV) planes. Each gas window is made of 6- $\mu\text{m}$  thick Mylar coated with aluminum to shield the signals from noise. Each wire plane is sandwiched between two high voltage planes. The distance between a wire plane and a neighboring high voltage plane is 13 mm. The three high voltage planes are 6- $\mu\text{m}$  thick Mylar coated with a 0.5- $\mu\text{m}$  layer of gold for good conductivity. The middle high voltage plane is coated with gold on both sides, while the other two high voltage planes are single-sided. There are 400 wires on each wire plane. The first and last 16 wires on each wire plane are grounded to shape the electric field. The remaining 368 wires are all 20- $\mu\text{m}$  diameter signal wires which are made of tungsten coated with gold. The wires are oriented at  $\pm 45^\circ$  with respect to the dispersive direction. The distance between two neighboring wires is 4.243 mm.

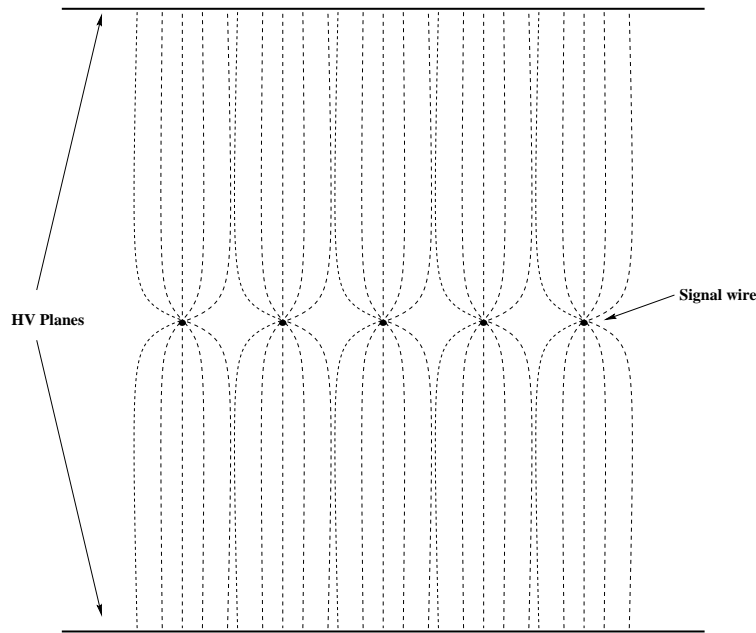


Figure 2-11: A schematic display of the electric field between two high voltage planes. The signal wires are separated by 4.243 mm, and the distance between the wires and the high voltage planes is 13 mm.

The gas used for VDC is argon-ethane mixture (1:1 by volume). The operational high voltage is about -4.0 kV. When a charged particle goes through the VDC, the atoms of the gas are ionized along its trajectory. The electrons drift along the electric field line towards the wire. In the vicinity of the wire, the electric field increases as  $1/r$ , the electrons can gain enough energy within a single mean-free-path to cause another ionization. The ionized electrons will again gain enough energy to induce more ionizations. This process is called an avalanche. As the avalanche approaches the wire, a negative signal is induced by the rapid depletion of the ions. A TDC is used to measure the time elapsed between the initial ionization and the induction of the signal on the sense wire. Knowledge of the drift velocity of the electron in the chamber gas allows the drift distance and eventually the perpendicular distance between the particle trajectory and the wire to be deduced. Generally, five or six adjacent wires fire for a trajectory. From the distances between the trajectory and the wires, the intersection point between the trajectory and the wire plane may be determined. As there are four wire planes on each spectrometer, four intersection points may be obtained. These lead to two positions  $(x_{fp}, y_{fp})$  and two angles  $(\theta_{fp}, \phi_{fp})$  for each trajectory at the focal plane.

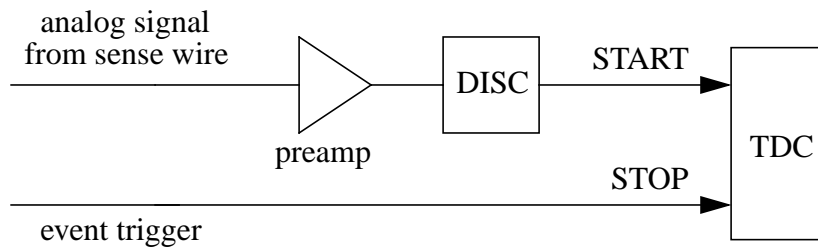


Figure 2-12: VDC block diagram.

When electrons recombine with ions, or energetic electrons strike the wire (anode), low energy photons can be produced. These photons can travel longer distances than the electrons and interact with the gas atoms to produce ion pairs at other locations.

The quenching gas (ethane) can absorb or dissipate the energies of these photons. Since ethane is a better quenching agent than  $\text{CO}_2$ , when the VDC is operated with argon- $\text{CO}_2$  gas mixture, the high voltage will be lower (3.65 kV).

Each wire has been positioned better than  $50 \mu\text{m}$  [28]. The relative position of the VDCs is known to  $100 \mu\text{m}$ . The main contribution to the ultimate position resolution is from the drift-time measurement. The final FWHM focal plane position resolution due to the VDC pair is about  $200 \mu\text{m}$ .

### 2.6.3 Gas Cerenkov

On the HRSE, a Cerenkov detector filled with  $\text{CO}_2$  gas is used to separate electrons from negatively-charged pions. The gas Cerenkov detector is based on the Cerenkov effect. When a charged particle passes through the detector having a speed exceeding the speed of light in the media, Cerenkov light is emitted. By detecting the Cerenkov light, it may be determined whether or not the velocity of the particle is larger than the threshold velocity  $c/n$ , where  $n$  is the refractive index of the media.

The  $\text{CO}_2$  gas Cerenkov detector is operated at atmospheric pressure. The refractive index of  $\text{CO}_2$  gas at one standard atmosphere is about 1.00041, therefore the threshold momentum for Cerenkov emittance for electrons is 17 MeV/c, and for pions is 4.8 GeV/c. The Cerenkov light is emitted at an angle of  $\theta = \cos^{-1}(1/n\beta)$  with respect of the direction of the charged particle. Here,  $\beta$  is the velocity of the particle relative to the speed of light in vacuum. When  $n\beta \rightarrow 1$ , the Cerenkov light is concentrated in a very narrow cone in the forward direction.

The gas Cerenkov detector consists of ten mirrors and ten 5-inch phototubes. The ten mirrors are placed just before the exit window and are grouped in two columns. Each mirror reflects the light onto a phototube which is placed at the side of the box. The positions and angles of the phototubes are arranged to maximize the collection of the Cerenkov light. The thickness of the  $\text{CO}_2$  gas is about 1.5 meters. The total

number of photoelectrons due to the Cerenkov emission of an extremely relativistic electron is about 23, therefore the efficiency of Cerenkov emittance can be as high as  $1 - \exp(-23) > 99.99\%$ .

## 2.7 Waterfall Target

Water ( $\text{H}_2\text{O}$ ) was chosen as the target for this study of  $^{16}\text{O}$ . The waterfall target was constructed by a group from INFN, and the basic design configuration for the apparatus is presented in detail in [23]. The water is continuously pumped from a reservoir through a heat exchanger, into the target can (which is sitting in the vacuum of the scattering chamber), and then back into the reservoir. Due to the surface tension and adherence, when the water flows down between a pair of stainless steel posts inside the can, a waterfall foil is generated. The waterfall target can is a rectangular box with a size of  $20\text{ cm} \times 15\text{ cm} \times 10\text{ cm}$ , and it contains one atmosphere of air. The entrance and exit windows of the can are made of  $50\text{ }\mu\text{m}$  and  $75\text{ }\mu\text{m}$  beryllium foils respectively, which allow large beam current ( $\sim 70\text{ }\mu\text{A}$ ) to pass through. The two side windows are made of  $25\text{ }\mu\text{m}$  stainless steel - a trade-off between having enough strength to sustain the pressure difference and minimizing the multiple scattering and radiative effects. Three pairs of stainless steel posts generate three water foils. The layout of the three foils is displayed in Figure 2-13.

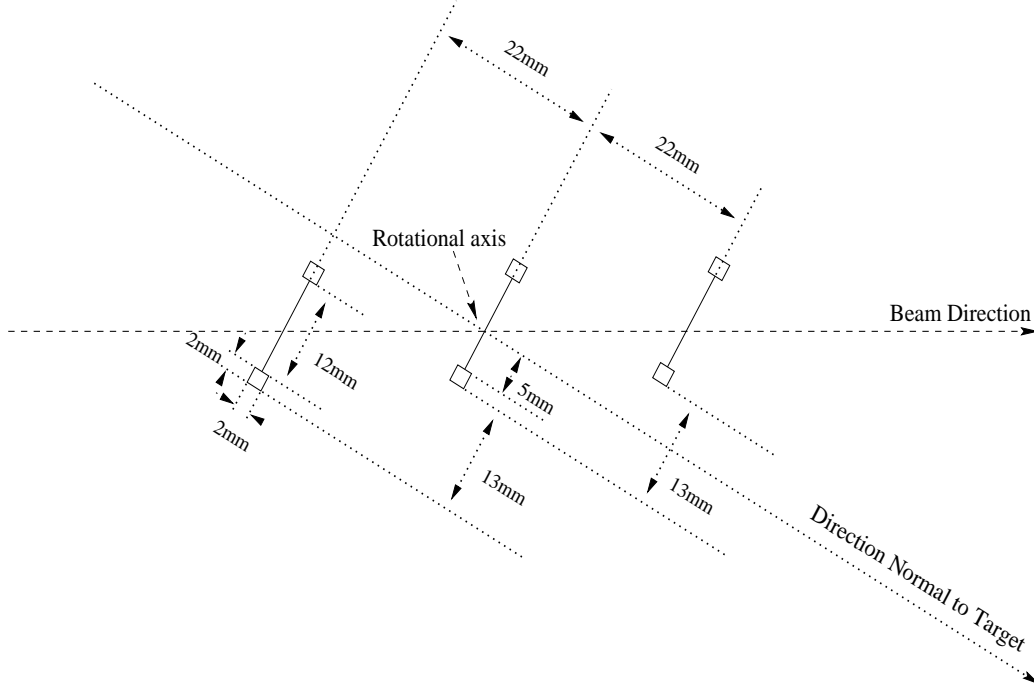


Figure 2-13: The waterfall target configuration. The three water foils are identical, 12-mm wide, and guided by posts which are 2 mm  $\times$  2 mm. In the direction normal to the target, the foils are separated by 22 mm. Along the target, the first foil is shifted down the page by 13 mm and second up the page by 13 mm. The rotational axis occurs at the intersection of the incident electron beam and the central foil. The distance from the rotational axis to the nearest post is 5 mm. The foils are parallel, and the angle between the beam direction and the direction normal to the target is 30°. The tolerance of the machining was better than 0.15 mm.

The waterfall target was built specifically for experiments E89-003 and E89-033. It was designed so that the outgoing particles from each foil do not go through the other foils or the aluminum posts, and the energy loss in the target as well as the multiple scattering due to the target are optimized.

A waterfall target is particularly useful for this experiment because of the hydrogen content of the water molecule. Since the kinematics of this experiment are quasielastic,  $H(e, e')$  can serve as a continuous luminosity monitor, and  $H(e, e'p)$  can be used

to determine the  $\vec{q}$ -direction precisely. Thus, this experiment is both self-calibrating and self-normalizing.

## 2.8 Trigger Electronics

The trigger electronics determine whether or not an event is to be recorded by the data acquisition system. Since the two spectrometers are alike, their trigger systems are very similar, and the coincidence trigger is just an *AND* of the two single spectrometer triggers.

The logic diagram of the trigger electronics is presented in Figure 2-14. The signals from the two sides of each scintillator paddle were discriminated to provide accurate timing information. In parallel, the analog signals were sent to ADCs. The timing signals were delayed, and then sent to both TDCs and scalers. Also, the timing signals from the two sides of the same paddle were sent to a logical unit *AND* to generate the timing signals for that scintillator paddle. The timing signal from each scintillator paddle was then sent to a 16-bit MLU (Memory Lookup Unit). The lower twelve bits correspond to the twelve scintillator paddles of the two scintillator planes. Only a certain hit pattern (S-ray) is taken as a good trigger. The S-ray is defined in the following manner: if the paddle  $n$  of one scintillator plane fires, then on the other scintillator plane, the hit must be from one of the three paddles  $n-1$ ,  $n$ ,  $n+1$ , or the overlap between two of them. The single spectrometer trigger was formed from the mean-timed *AND* of the two scintillator planes. The coincidence trigger signal is generated from the *AND* of the two spectrometer triggers.

The two single spectrometer triggers S1 and S3, together with the coincidence trigger S5, are sent to scalers as well as the Trigger Supervisor (TS). The Trigger Supervisor is a custom-made module built by the CEBAF Data Acquisition Group. It synchronizes the readout crates, administers the deadtime logic of the entire system, and prescales various trigger inputs. S1 and S3 are also sent to a TDC so that the

coincidence timing is measured.

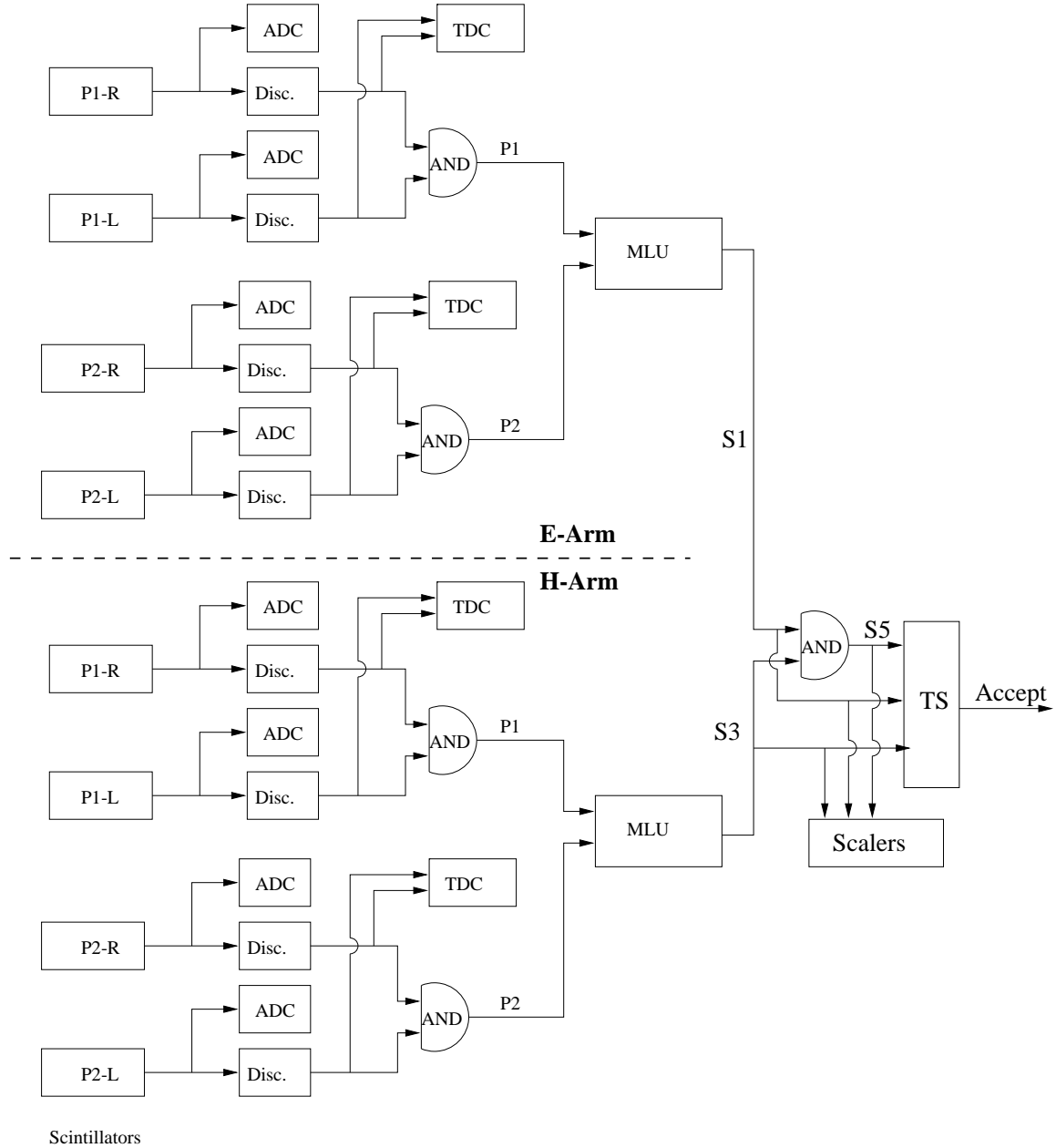


Figure 2-14: A schematic diagram of trigger electronics setup.

## 2.9 Data Acquisition

CODA [29] (CEBAF Online Data Acquisition), a toolkit developed at Jefferson Lab by the Data Acquisition Group, was used to manage the data acquisition system in Hall A. During this experiment, CODA 1.4 was used. The Data Acquisition system for this experiment is displayed in Figure 2-15.

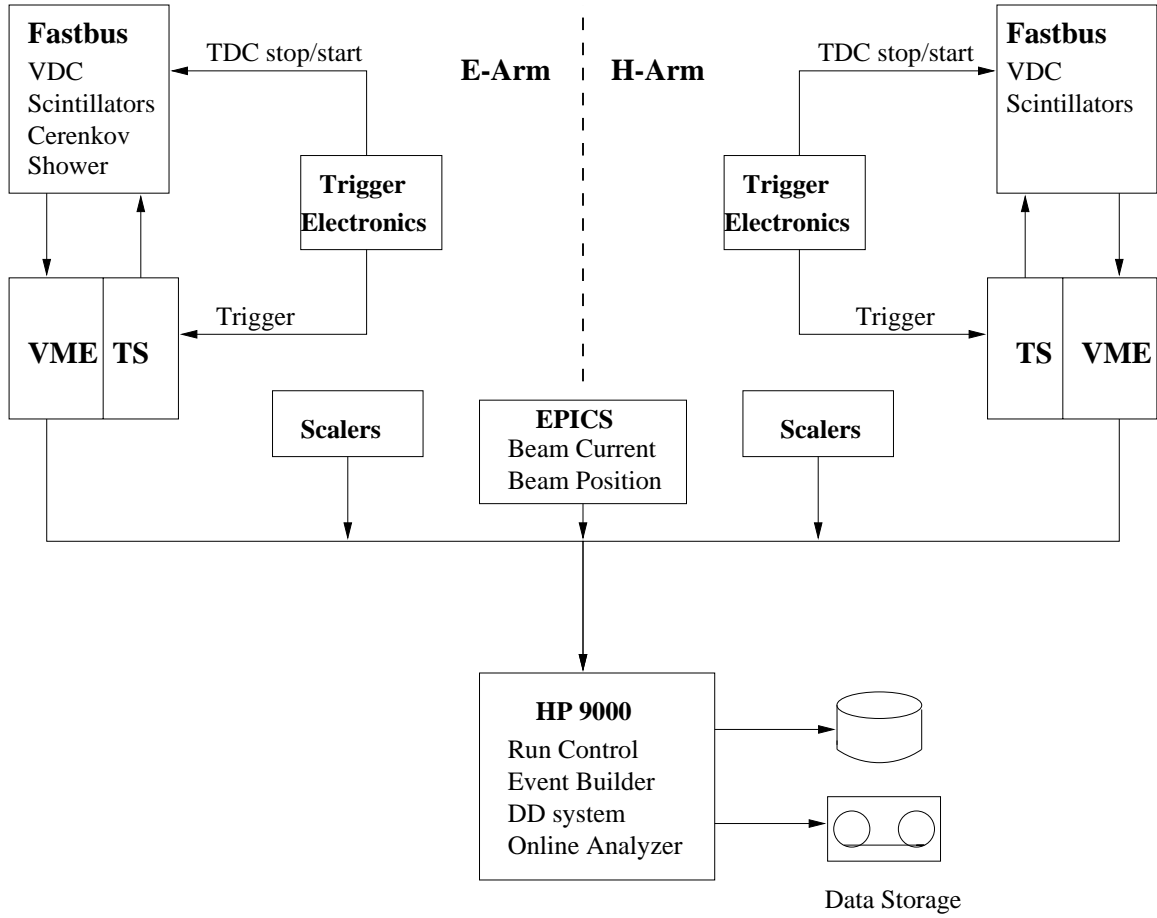


Figure 2-15: Data Acquisition system for E89-003.

On each spectrometer, there is one VME crate, one Fastbus crate and one Trigger Supervisor (TS) located inside the spectrometer shielding house. The VME crate

contains scalers. The Fastbus modules are for the detectors and consist of:

- LeCroy model 1877 TDCs: operating in common-stop mode with 0.5 ns resolution for the VDCs;
- LeCroy model 1875 TDCs: operating in common-start mode with 0.1 ns resolution for the scintillators and trigger diagnostics;
- LeCroy model 1881M ADCs: for analog signals from the scintillators and the gas Cerenkov detector.

In the counting house, an HP-9000 computer was used to run CODA and to collect the data. CODA consists of three components:

- a Readout Controller (ROC) which interfaces with the detector systems. In this experiment, ROCs were the CPUs in the Fastbus and the VME crate. The Trigger Supervisor controls the state of the run, and generates the triggers that cause the ROCs to be read out.
- an Event Builder (EB) which collects all the ROC data fragments, and incorporates all of the necessary CODA header information needed to describe and label an event and the data fragments to build the event.
- an Analyzer/Data Distribution (ANA/DD) which analyzes and/or sends the events to the disk of the computer in the counting house.

There were several types of events in the data stream. The first few events in the data file of each run were a series of status events, which were included whenever the state of the run changed. In addition, there were some user-defined status events. Most events in the data file were physics events, which contained information from only one spectrometer (single arm) or both spectrometers (coincidence). For this experiment, the size of a typical coincidence event was about 0.8-1.0 kB, and a single arm event was about half that. In total, 86 GB of data was taken during this

experiment. In addition to the two types of events above, there were scalers events which were read out every 10 seconds, and EPICS events which included the beam position and beam current information.

## Chapter 3

# Data Analysis

### 3.1 The Analyzer - ESPACE

The data analysis code, ESPACE, is the Event Scanning Program for hall A Collaboration Experiments. It was adapted from an event analyzer developed in MAINZ by Offermann [51]. It is relatively flexible and user-friendly. A detailed description can be found in the user's guide [52]. Some main features for ESPACE are presented below:

- It can generate one or more dimensional (ntuple) histograms of all the relevant spectra including the raw detector TDC and ADC signals as well as physics quantities such as the momentum and direction of the particle.
- It carries out the VDC analysis, calculates the focal plane positions  $(x_{fp}, y_{fp})$  and angles  $(\theta_{fp}, \phi_{fp})$  of the trajectories.
- It traces the trajectories back through the spectrometer to the target, using the matrix elements to obtain the relative momentum  $(dp/p)$ , transverse position  $(y_{tg})$ , and angles  $(\theta_{tg}, \phi_{tg})$  of the charged particles.
- It can perform optics optimization: an iterative fitting procedure to the optics

study data to get the correct optical matrix elements.

- It contains a logic package which allows spectra with logic tests and cut conditions to be created.
- It can filter data according to predetermined conditions.
- It can correct the raw time-of-flight event-by-event for path length and velocity variations; it can also correct for the energy loss of charged particles before and after the reaction.

## 3.2 Focal Plane Track Reconstruction and $e^-/\pi^-$ Separation

### 3.2.1 Scintillators

There are two scintillator planes S1 and S2 on each spectrometer. Each scintillator plane consists of six paddles. For each paddle, there are two phototubes (one at each side). Each phototube provides a signal for a TDC and a signal for an ADC. Figure 3-1 shows the TDC and ADC spectra generated by one of the phototubes for  $\sim 800$  MeV electrons. The width of TDC spectrum is about 1 ns, which is mainly due to the photon walking time in the scintillator, as well as the reaction time of the phototube and associated electronics. The ADC value is basically proportional to the energy deposited by the electrons in the scintillator. Since the scintillator plane is very thin ( $\sim 0.5$  cm), the energy deposited by the electrons in the scintillator has a Landau distribution.

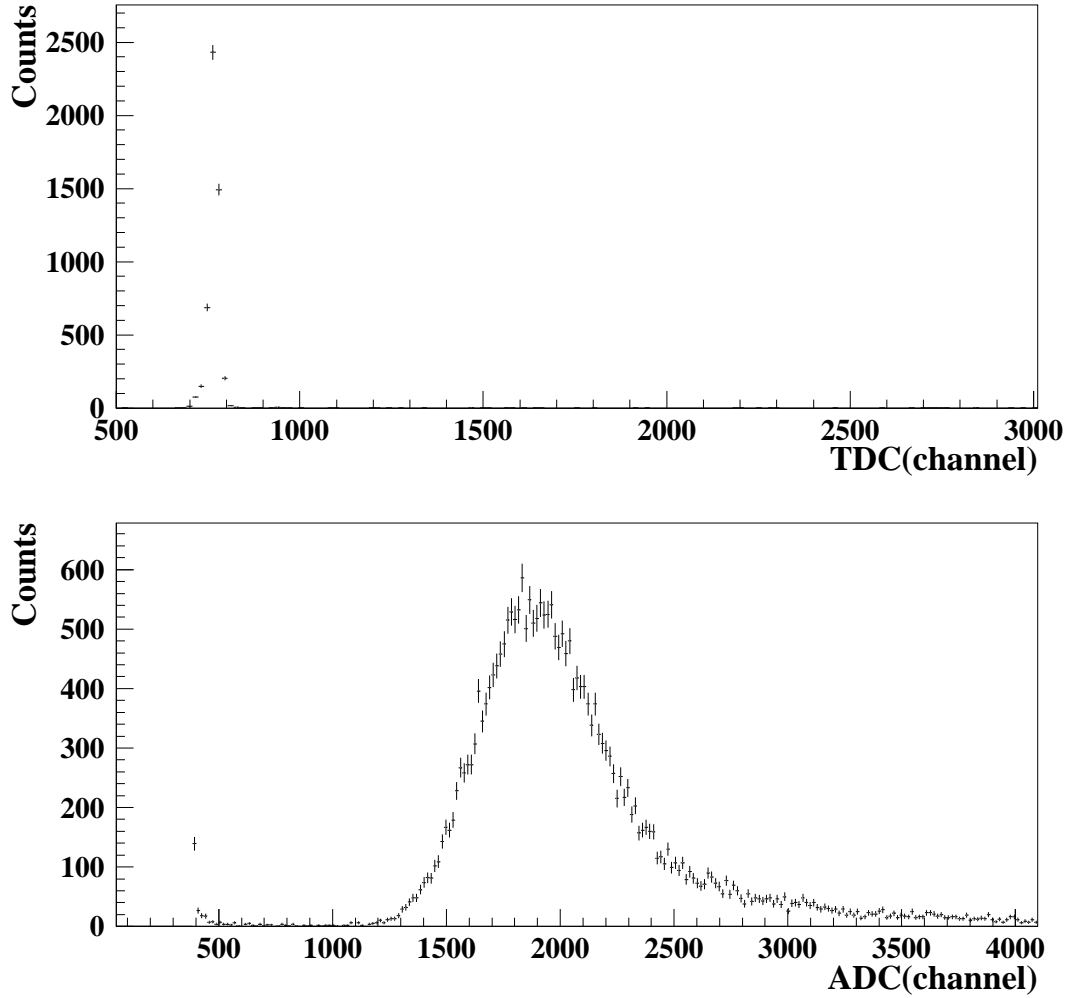


Figure 3-1: Scintillator TDC and ADC spectra for a single phototube. Here, one TDC channel is 0.1 ns.

### 3.2.2 Focal Plane Trajectory Reconstruction

The trajectories of the charged particles at the focal plane are determined from the drift times measured by the VDCs. In both spectrometers, VDC drift times are

measured in a common TDC stop mode: every signal wire which fires starts its own TDC, and all the TDCs are stopped by the scintillator trigger. The TDCs used are LeCroy 1877s with multihit capability, but only the first hit of each wire is analyzed. Figure 3-2 shows a typical electron track inclined at an angle  $\theta$  with respect to the wire plane. The arrowed solid lines (labeled geodetic in the figure) represent the shortest drift distance. The dot-dashed line is the vertical distance from the track to the signal wire. These vertical distances determined by adjacent wires are used to obtain the cross-over point between the trajectory and the wire plane.

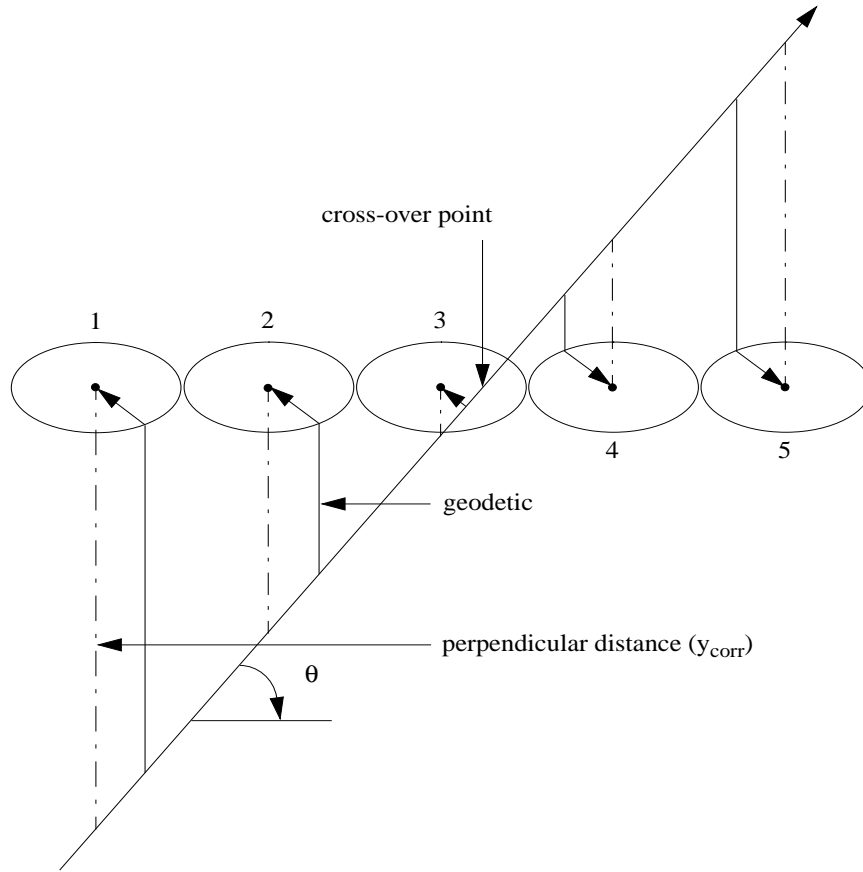


Figure 3-2: A typical trajectory in one of the VDC wire planes. The geodetic is the shortest drift time. The perpendicular distances (dot-dashed lines) are fit with a line to obtain the cross-over point between the trajectory and the wire plane.

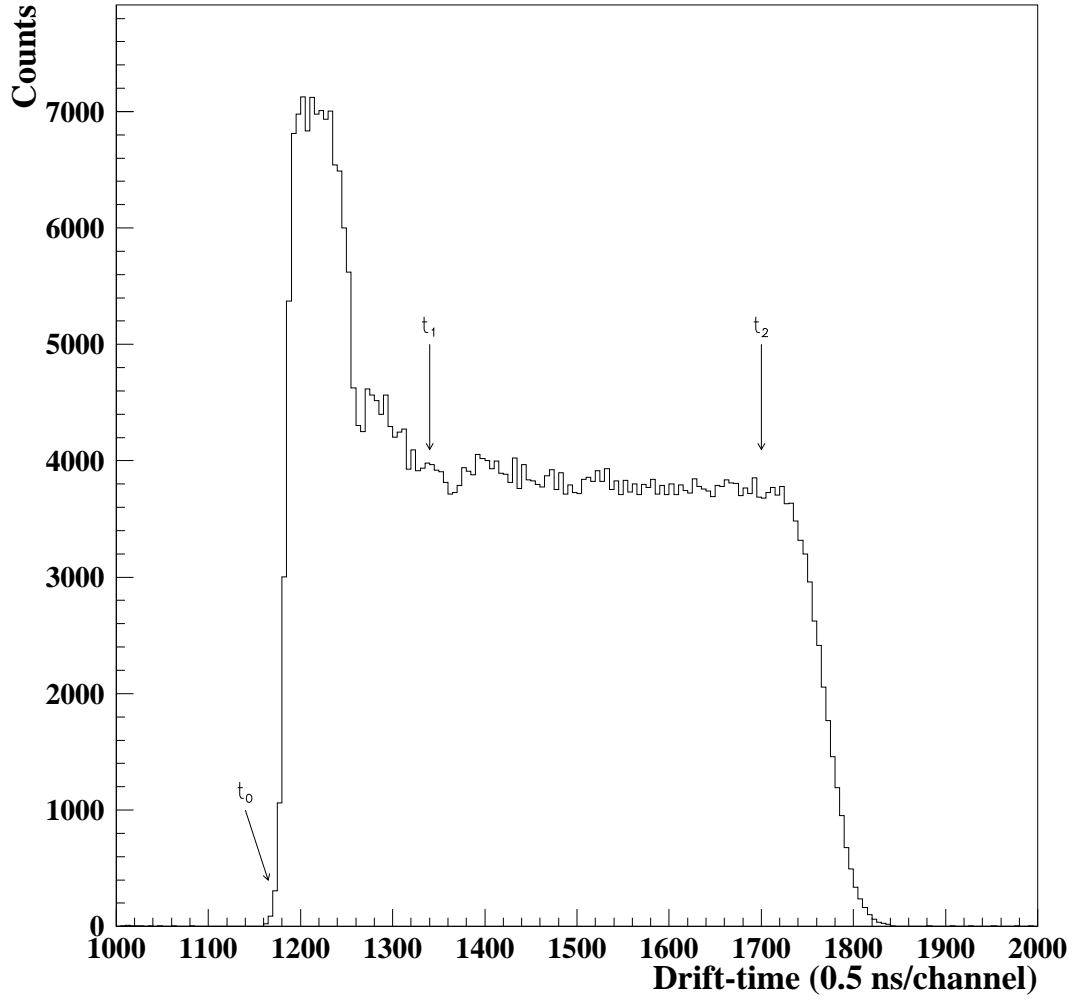


Figure 3-3: VDC Drift Time Spectrum

Figure 3-3 shows the drift-time histogram for a quasielastic spectrum.  $t_0$  is the offset of the drift time, which is set by the TDC. Between  $t_1$  and  $t_2$ , the drift time histogram is essentially flat. The number of counts per unit drift time,  $dN/dt$ , can

be expressed as

$$\frac{dN}{dt} = \frac{dN}{dy} \frac{dy}{dt} = \frac{dN}{dy} v_d \quad (3.1)$$

where  $dN/dy$  is the number of counts per unit vertical distance, and  $v_d$  is the drift velocity. If the VDC has been uniformly-illuminated ( $dN/dy = \text{constant}$ ), the shape of the drift time histogram reflects the drift velocity. The peak around channel 1200 in the drift time histogram is an effective increase in drift velocity due to the change in the geometry of the field lines in the region near the wire. By integrating 3.1,

$$y(t) = \frac{1}{dN/dy} \int_{t_0}^t \frac{dN}{dt'} dt' \quad (3.2)$$

may be obtained. This equation is only valid for  $t_0 < t < t_2$  since  $dN/dy$  is constant within this range. As the drift distance for  $t > t_2$  is larger than the cell size, those events are ignored. For drift times between  $t_1$  and  $t_2$ , both the drift velocity  $v_d$  and  $dN/dy$  are constant, and thus,

$$\frac{dN}{dy} = \langle \frac{dN}{dt} \rangle_{flat} / v_d. \quad (3.3)$$

Here  $\langle \frac{dN}{dt} \rangle_{flat}$  is the average number of counts per unit drift time between  $t_1$  and  $t_2$  where the histogram is flat.

The drift velocity for the argon-ethane gas mixture at -4.0 kV is about  $50 \mu\text{m/ns}$ . Therefore, the shortest drift distance can be calculated from the drift time as follows:

$$y(t) = \frac{v_d}{\langle \frac{dN}{dt} \rangle_{flat}} \int_{t_0}^t \frac{dN}{dt'} dt'. \quad (3.4)$$

Note that the perpendicular distances from the trajectory to the wires need to be known to obtain the cross-over point. Only when the trajectory is inclined at  $45^\circ$  with respect to the wire plane does the shortest drift distance equal to the perpendicular distance [30]. Therefore, the dependence of the perpendicular distance upon the

trajectory angle has to be corrected. Since the range of the VDC angular acceptance is  $\sim 45^\circ \pm 6^\circ$  and the radius of the radial field region is about 2 mm, this correction is less than 200  $\mu\text{m}$ . There are several methods which may be used to perform this correction. The Schmitt correction can be found in [53].

For the Hall A VDCs, a GARFIELD [54] simulation program has been used to convert the drift time to the perpendicular distance. The details of this description can be found in [28].

Once the perpendicular distances from the trajectory to the five or six adjacent wires are obtained, a line-fit is applied to determine the cross-over point where the trajectory passes through the wire plane.

Consider two coordinate systems, UVZ and XYZ. The UV plane coincides with the first wire plane U1.  $\hat{U}$  is perpendicular to the direction of the wires in the U1 plane,  $\hat{V}$  is perpendicular to the direction of the wires in the V1 plane, and  $\hat{Z}$  is pointing upward. The XYZ is obtained simply by rotating UVZ about the Z-axis for  $45^\circ$  so that  $\hat{X}$  is along the positive dispersive direction. The origin of the two coordinate systems is the intersection of wire 184 in the U1 plane and the projection of wire 184 in the V1 plane onto the U1 plane. The XYZ system is actually the Detector Coordinate System which will be discussed later in Section 3.3.1. The distance between U1 and V1 (or U2 and V2) is  $d1$ , while the distance between U1 and U2 (or V1 and V2) is  $d2$ . The diagrams are depicted in Figures 3-4 and 3-5.

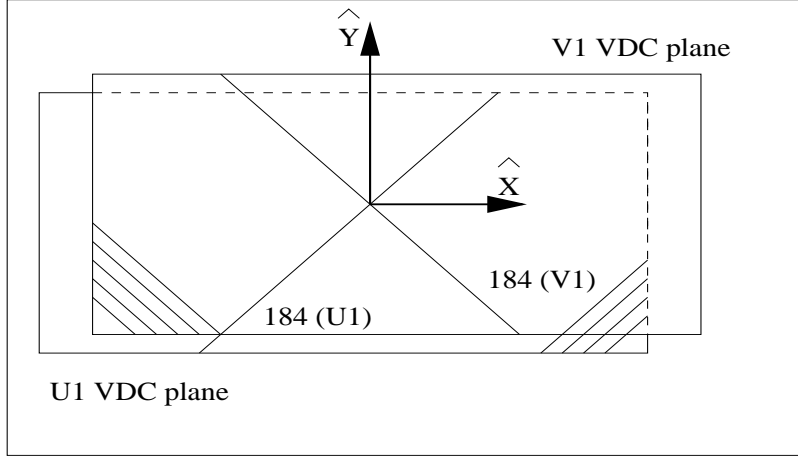


Figure 3-4: The coordinate system  $XYZ$ .  $\hat{Z}$  is pointing out of the page. The  $UVZ$  coordinate system (not shown in this plot) can be obtained by simply rotating the  $XYZ$  coordinate system in a counter clockwise fashion about the  $Z$ -axis by  $45^\circ$ .

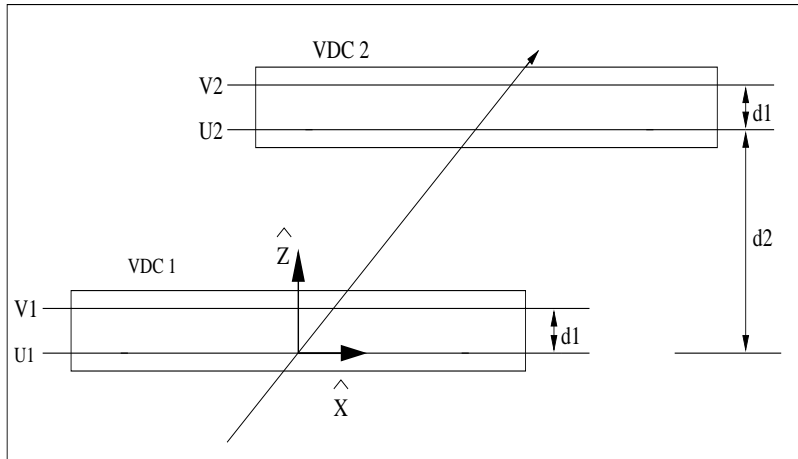


Figure 3-5: A side view of the coordinate system  $XYZ$ .  $d1$  is 26 mm, and  $d2$  is about 35 cm.

In the  $UVZ$  coordinate system, assume that a trajectory passes through the  $U1$  plane at  $(u1, w1, 0)$ , the  $V1$  plane at  $(w2, v1, d1)$ , the  $U2$  plane at  $(u2, w3, d2)$ , and the  $V2$  plane at  $(w4, v2, d1 + d2)$ .  $u1$ ,  $v1$ ,  $u2$ , and  $v2$  can be measured by each wire plane

directly. Thus, the angles of the trajectory with respect to  $\hat{U}$  and  $\hat{V}$  are

$$\tan \theta_U = \frac{dU}{dZ} = \frac{u2 - u1}{d2} \quad (3.5)$$

$$\tan \theta_V = \frac{dU}{dZ} = \frac{v2 - v1}{d2}. \quad (3.6)$$

Using geometry,  $w1$  can also be obtained

$$w1 = v1 - d1 \tan \theta_V = v1 - d1 \frac{v2 - v1}{d2}. \quad (3.7)$$

Therefore, the trajectory has been completely determined by the VDC pair.

In the XYZ system, the trajectory passes through the XY plane at  $(x, y)$  with

$$x = u1 \cos 45^\circ + w1 \sin 45^\circ = \frac{\sqrt{2}}{2} (u1 + v1 - d1 \frac{u2 - u1}{d2}) \quad (3.8)$$

$$y = -u1 \sin 45^\circ + w1 \cos 45^\circ = \frac{\sqrt{2}}{2} (-u1 + v1 - d1 \frac{u2 - u1}{d2}). \quad (3.9)$$

The angles of the trajectory with respect to  $\hat{X}$  and  $\hat{Y}$  ( $\tan \theta, \tan \phi$ ) are

$$\tan \theta = \frac{dX}{dZ} = \frac{\sqrt{2}}{2} (\tan \theta_U + \tan \theta_V) = \frac{\sqrt{2}(u2 - u1 + v2 - v1)}{2d2} \quad (3.10)$$

$$\tan \phi = \frac{dY}{dZ} = \frac{\sqrt{2}}{2} (-\tan \theta_U + \tan \theta_V) = \frac{\sqrt{2}(u1 - u2 + v2 - v1)}{2d2}. \quad (3.11)$$

### 3.2.3 $e^-/\pi^-$ Separation

The gas Cerenkov detector mounted on HRSE is used for  $e^-/\pi^-$  separation. In one atmosphere of  $\text{CO}_2$  gas, the threshold momentum for  $\pi^-$  to emit Cerenkov radiation is 4.4 GeV/c, while for an electron it is 17 MeV/c. As the HRSE central momenta are much less than 4.4 GeV/c for this experiment,  $\pi^-$  accepted by the HRSE cannot emit Cerenkov light. Figure 3-6 shows the typical TDC and ADC spectra for a single phototube connected to the gas Cerenkov detector.

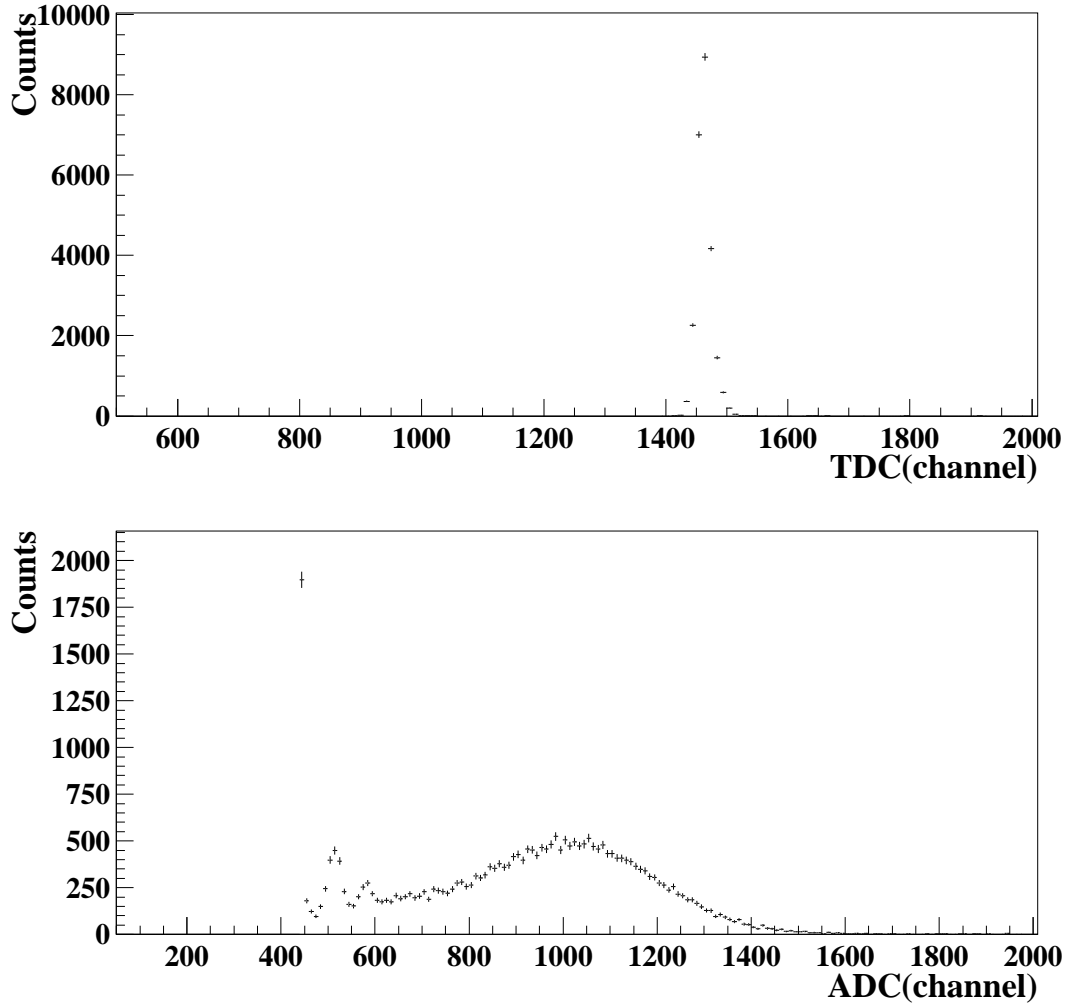


Figure 3-6: Gas Cerenkov TDC and ADC spectra for a single phototube. The TDC is 0.1 ns/channel. In the ADC spectrum, the spike around channel 450 is the pedestal, which is the offset voltage read out when there was no event corresponding to this phototube. The peak around channel 520 is the single photo electron peak, while the peak around channel 580 is the double photo electron peak.

In the ADC spectrum, the first spike around channel 450 is the pedestal, which is

the offset voltage read out when that phototube does not see any Cerenkov radiation. The single photo electron peak is around channel 520, while the peak around channel 580 is due to two photo electrons. The ADC value is related to the number of photo electrons generated by an incoming charged particle. The event cut condition signaling an electron is that at least one phototube yields an ADC signal which is higher than half of the single photo electron peak.

### 3.3 Calibrations of High Resolution Spectrometers

#### 3.3.1 Optics Study of HRS

The two spectrometers (HRSE and HRSH) have the same configuration (QQDQ) and optical features. To discuss the optical properties of the spectrometers, the following Cartesian coordinate systems [50] have been defined.

- **Hall Coordinate System (HCS)** The origin of the HCS is the center of the hall, which is on the beamline.  $\hat{z}$  is along the beamline and points to the beam dump,  $\hat{y}$  is perpendicular to the horizontal plane, and points up. Surveys of the spectrometers (angles and offsets) are always conducted in this coordinate system.

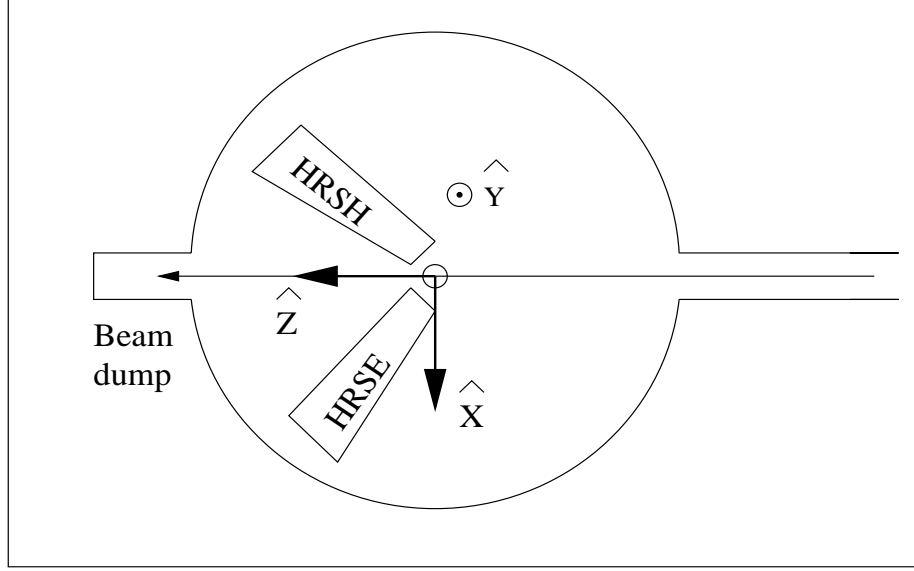


Figure 3-7: Hall Coordinate System.

- Target Coordinate System (TCS)** The TCS actually moves with the spectrometer.  $\hat{z}$  is along the central axis of the first quadrupole Q1 (the idea central ray). The origin of the TCS is center of HCS when the central axis of Q1 is pointing at the center of the hall.  $\hat{x}$  is pointing down, and  $\hat{y}$  is in the horizontal plane. The out-of-plane angle  $\tan \theta_{tg}$  and the in-plane angle  $\tan \phi_{tg}$  of the trajectory in the target coordinate system are defined as

$$\tan \theta_{tg} = \frac{dx}{dz} \quad (3.12)$$

$$\tan \phi_{tg} = \frac{dy}{dz}. \quad (3.13)$$

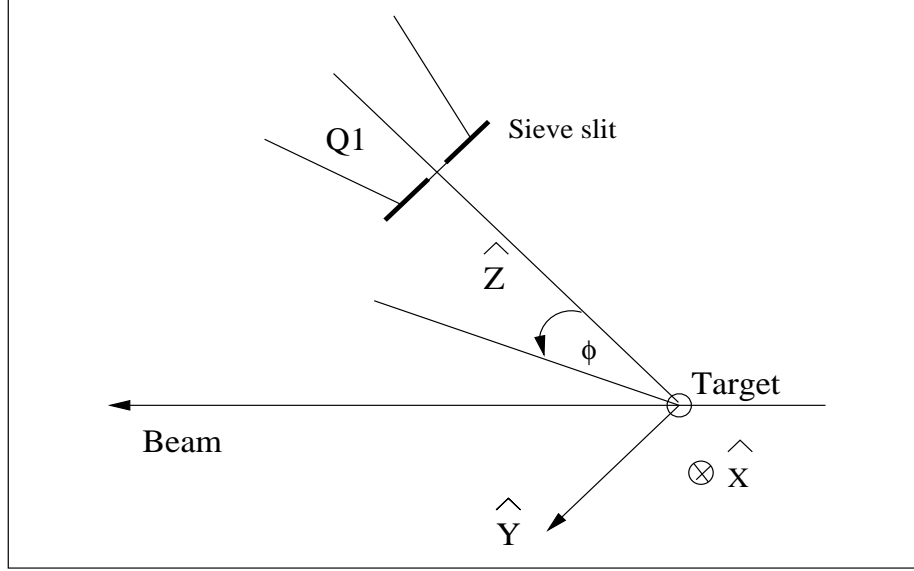


Figure 3-8: Target Coordinate System.

- **Detector Coordinate System (DCS)** The directions and positions of the trajectories at the focal plane are defined in the DCS. It is displayed in Figures 3-4 and 3-5. The origin of the DCS is the intersection of wire 184 of the VDC1 U1 plane and the projection of wire 184 in the VDC1 V1 plane onto the VDC1 U1 plane.  $\hat{z}$  is perpendicular to the U1 plane and points up,  $\hat{y}$  is parallel to the short symmetry axis of VDC1, and  $\hat{x}$  points away from the center of curvature of the dipole. The angles  $\tan \theta_{det}$  and  $\tan \phi_{det}$  are defined as

$$\tan \theta_{det} = \frac{dx_{det}}{dz_{det}} \quad (3.14)$$

$$\tan \phi_{det} = \frac{dy_{det}}{dz_{det}}. \quad (3.15)$$

- **Transport Coordinate System (TRCS)** If the DCS is rotated by  $45^\circ$  clockwise along  $\hat{y}$  so that the new  $\hat{z}$  direction is along the central ray, it becomes the

TRCS (Figure 3-9). If the trajectory passes through the point  $(x_{det}, y_{det}, 0)$  in the DCS with angles  $\tan \theta_{det}$  and  $\tan \phi_{det}$ , then in the TRCS the corresponding point  $(x_{tra}, y_{tra}, 0)$  and angles  $(\tan \theta_{tra}, \tan \phi_{tra})$  are

$$\tan \theta_{tra} = \frac{\tan \theta_{det} + \tan \rho_0}{1 - \theta_{det} \tan \rho_0} \quad (3.16)$$

$$\tan \phi_{tra} = \frac{\tan \phi_{det}}{\cos \rho_0 - \sin \rho_0 \tan \theta_{det}} \quad (3.17)$$

$$x_{tra} = x_{det} \cos \rho_0 (1 + \tan \theta_{tra} \tan \rho_0) \quad (3.18)$$

$$y_{tra} = y_{det} + \sin \rho_0 \tan \phi_{tra} x_{det}. \quad (3.19)$$

Note that  $\rho_0$  is the rotational angle  $-45^\circ$ .

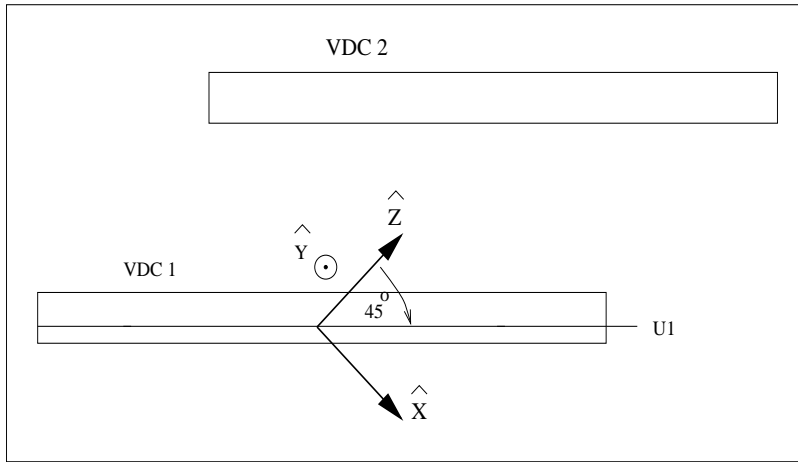


Figure 3-9: Transport Coordinate System.

- **Focal Plane Coordinate System (FPCS)** The FPCS has been chosen for the HRS data analysis. It is obtained by rotating the DCS around its  $y$ -axis by an angle  $\rho$ , where  $\rho$  is the angle between the  $\hat{z}$  of DCS and the local central ray [52]. The local central ray is the ray at the focal plane with  $\theta_{tg} = 0, \phi_{tg} = 0$  and relative momentum  $dp/p = 0$ .

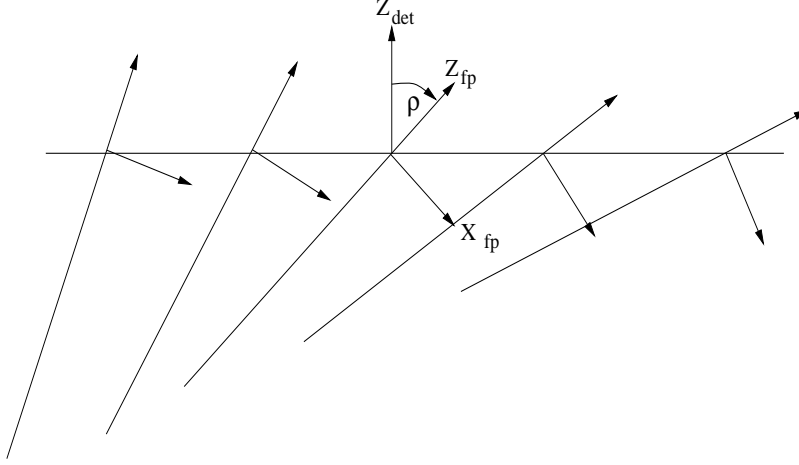


Figure 3-10: Focal Plane Coordinate System.

The FPCS also includes corrections for the offsets incurred due to misalignments of the VDC package. Therefore, in the FPCS, the coordinates and angles of the trajectory can be written as

$$x_{fp} = x_{tra} \quad (3.20)$$

$$y_{fp} = y_{tra} - \sum y_{i000} x_{fp}^i \quad (3.21)$$

$$\tan \theta_{fp} = \frac{\tan \theta_{det} + \tan \rho}{1 - \tan \theta_{det} \tan \rho} \quad (3.22)$$

$$\tan \phi_{fp} = \frac{\tan \phi_{det} - \sum p_{i000} x_{fp}^i}{\cos \rho - \sin \rho \tan \theta_{det}} \quad (3.23)$$

with

$$\tan \rho = \tan \rho_0 + \sum_{i>0} t_{i000} x_{fp}^i. \quad (3.24)$$

The focal plane coordinates ( $x_{fp}$ ,  $y_{fp}$ ,  $\tan \theta_{fp}$ , and  $\tan \phi_{fp}$ ) measured by the VDC pair are used to calculate the quantities in the TCS ( $x_{tg}$ ,  $y_{tg}$ ,  $\tan \theta_{tg}$ ,  $\tan \phi_{tg}$ , and  $\delta$  (the relative momentum  $dp/p$ )). Effectively, the  $x_{tg}$  is fixed at 0 during the optics

calibration by requiring that the beam spot is within 100  $\mu\text{m}$  of the  $y$ - $z$  plane of the TCS. The focal plane coordinates and the target coordinates are linked by a set of tensors  $Y_{ijkl}$ ,  $T_{ijkl}$ ,  $P_{ijkl}$  and  $D_{ijkl}$ :

$$y_{tg} = \sum_{i,j,k,l} Y_{ijkl} x_{fp}^i \tan^j \theta_{fp} y_{fp}^k \tan^l \phi_{fp} \quad (3.25)$$

$$\tan \theta_{tg} = \sum_{i,j,k,l} T_{ijkl} x_{fp}^i \tan^j \theta_{fp} y_{fp}^k \tan^l \phi_{fp} \quad (3.26)$$

$$\tan \phi_{tg} = \sum_{i,j,k,l} P_{ijkl} x_{fp}^i \tan^j \theta_{fp} y_{fp}^k \tan^l \phi_{fp} \quad (3.27)$$

$$\delta = \sum_{i,j,k,l} D_{ijkl} x_{fp}^i \tan^j \theta_{fp} y_{fp}^k \tan^l \phi_{fp}. \quad (3.28)$$

The mid-plane symmetry of the spectrometers requires that  $k + l$  is even for  $T_{ijkl}$  and  $D_{ijkl}$ , while  $k + l$  is odd for  $Y_{ijkl}$  and  $P_{ijkl}$ . The tensors are obtained by the minimization of the aberration functions

$$\Delta_q = \sum_s \left[ \frac{q_{tg}^s - q_{tg}^0}{\sigma_q^s} \right]^2 = \sum_s \left[ \frac{\sum_{i,j,k,l} Q_{ijkl} x_{fp}^i \tan^j \theta_{fp} y_{fp}^k \tan^l \phi_{fp} - q_{tg}^0}{\sigma_q^s} \right]^2 \quad (3.29)$$

where  $|q_{tg}^s - q_{tg}^0| \leq w_q$ . Here, the subscript  $q$  represents one of the four variables  $(y, \theta, \phi, \delta)$ , and the index  $s$  is varied over all the particles detected with their reconstructed vertex  $(y_{tg}^s, \theta_{tg}^s, \phi_{tg}^s, \delta^s)$  within the interval  $w$  of the peak value  $(y_{tg}^0, \theta_{tg}^0, \phi_{tg}^0, \delta^0)$ . The contribution of each particle track to the aberration function is weighted by the standard deviation  $(\sigma_y, \sigma_\theta, \sigma_\phi, \sigma_\delta)$  calculated for the particular track.

To extract the tensor matrix elements, elastic electron scattering data from a thin (55.8 mg/cm<sup>2</sup>) carbon target at a scattering angle of 16° were taken in April, 1997. The procedure was the following:

- A sieve slit with  $7 \times 7$  grid of holes was put in front of each spectrometer to localize the trajectories. The sieve slit was a piece of 5-mm thick tungsten. The space between two neighboring holes was 12.5 mm in the horizontal direction,

and 25 mm in the vertical direction. The radius of the small holes was 2.5 mm, while the radius of the two large holes was 5 mm. The distance from the sieve-slit to the target was about 117.0 cm. The position of the sieve slit in the TCS was precisely-determined via survey.

- The spectrometers were individually mispointed so that different  $y_{tg}^0$  were achieved (see Figure 3-11). Data on three different  $y_{tg}^0$  were taken. The position of the spectrometer for each setting was precisely-determined in the HCS via survey.

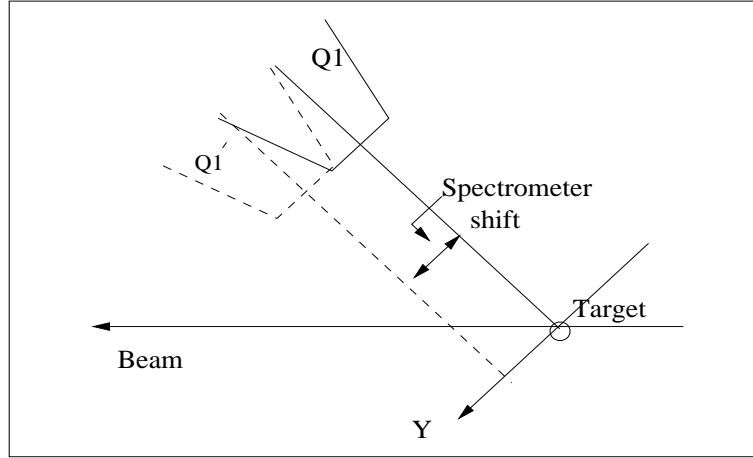


Figure 3-11: Mispointing the spectrometer.  $\Delta y_{tg}^0$  can be achieved by shifting the spectrometer in the  $y$  direction.

- For each  $y_{tg}^0$  setting, the elastic scattering peak was moved to seven different positions on the focal plane ( $\delta$  from -4.5% to +4.5% in steps of 1.5%) holding the quadrupole/dipole field ratio constant.
- The target position in the HCS was precisely-determined via survey. Therefore,  $y_{tg}^0$ ,  $\theta_{tg}^0$ , and  $\phi_{tg}^0$  for each hole at each setting could be obtained geometrically.

The ultimate results from the optics study are displayed in the following figures.

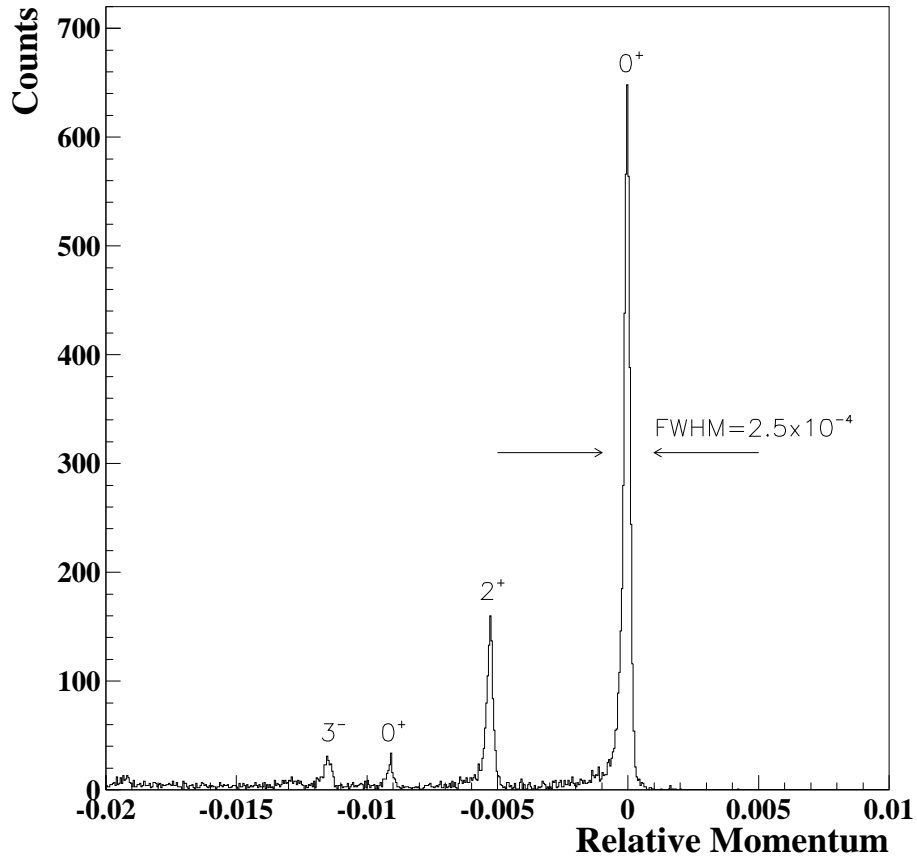


Figure 3-12: HRSE kinematically-corrected relative momentum spectrum for  $^{12}\text{C}(e, e')$ .

Figure 3-12 shows the kinematically-corrected relative momentum spectrum for  $^{12}\text{C}(e, e')$  on HRSE using the matrix elements obtained from the optics study. The incident beam energy was 845 MeV.

The kinematically-corrected relative momentum is the electron relative momentum ( $\delta = dp/p$ ) assuming the scattering angle is the spectrometer central angle  $\theta_0$ . With the energy loss in the target neglected, the relation between the elastically-scattered

electron momentum  $p$  and the scattering angle  $\theta$  is

$$p = \frac{p_i}{1 + 2p_i \sin^2(\theta/2)/M_t} \quad (3.30)$$

where  $p_i$  is the electron incident momentum, and  $M_t$  is the mass of the target. The kinematically-corrected momentum  $p_{kin}$  is defined as

$$p_{kin} = p \frac{1 + 2p_i \sin^2(\theta/2)/M_t}{1 + 2p_i \sin^2(\theta_0/2)/M_t}. \quad (3.31)$$

To first order

$$p_{kin} \approx p(1 + \frac{p_i \sin \theta_0}{M_t}(\theta - \theta_0)) \approx p(1 + \frac{p_i \sin \theta_0}{M_t}\phi_{tg}). \quad (3.32)$$

The kinematically-corrected relative momentum  $\delta_{kin}$  is therefore

$$\delta_{kin} = \frac{p_{kin} - p_0}{p_0} \quad (3.33)$$

where  $p_0$  is the spectrometer central momentum.

Figure 3-12 indicates that the FWHM relative momentum resolution of the spectrometer is about  $2.5 \times 10^{-4}$ . The ground state and the excited states of  $^{12}\text{C}$  are clearly visible. The main degradation in the momentum resolution is from multiple scattering in the exit window of the spectrometer.

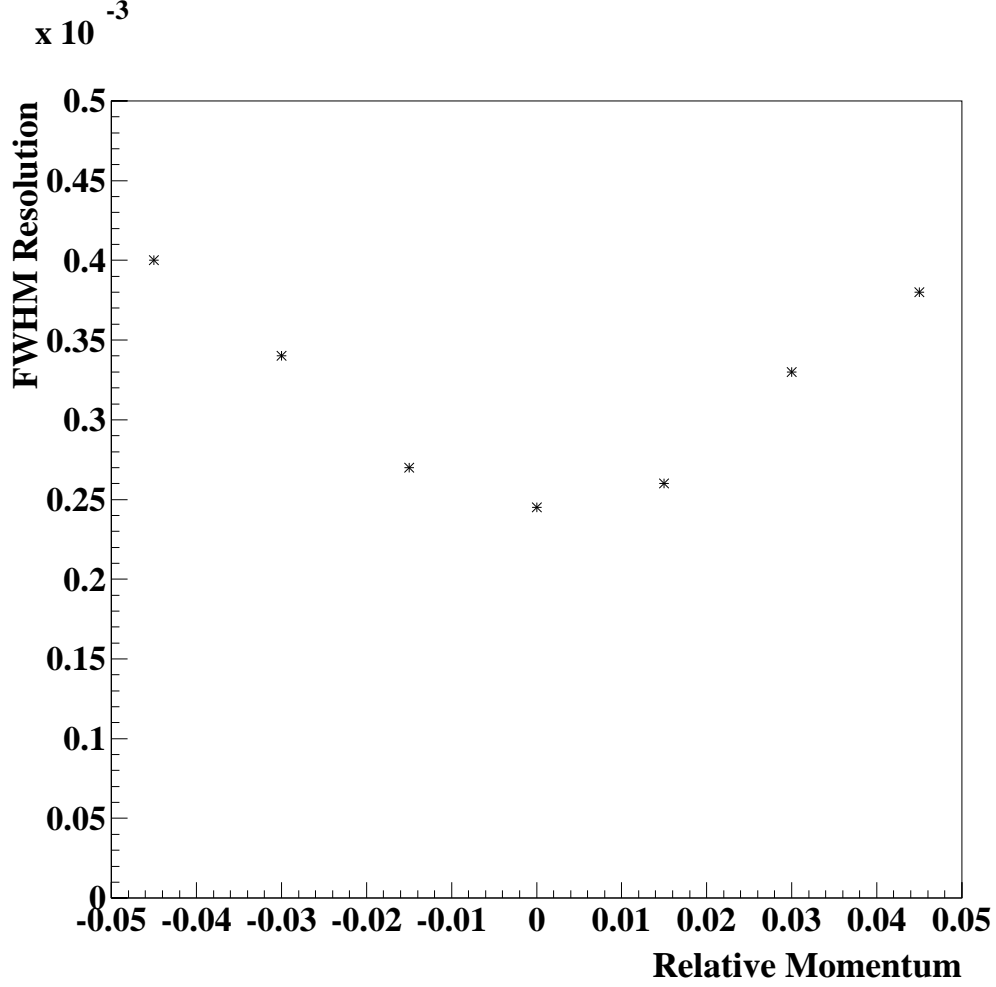


Figure 3-13: Relative momentum resolution across the HRS focal plane.

Figure 3-13 shows the distribution of the relative momentum ( $dp/p$ ) resolution across the HRS focal plane. At the center of the focal plane, the relative momentum resolution is about  $2.5 \times 10^{-4}$ , while at the edge, it is about  $4.0 \times 10^{-4}$ . This is mainly due to the fact that the actual focal plane does not coincide with the first wire plane. Therefore, at the sides of the focal plane, angular information is required to obtain the focal plane position, which introduces an error.

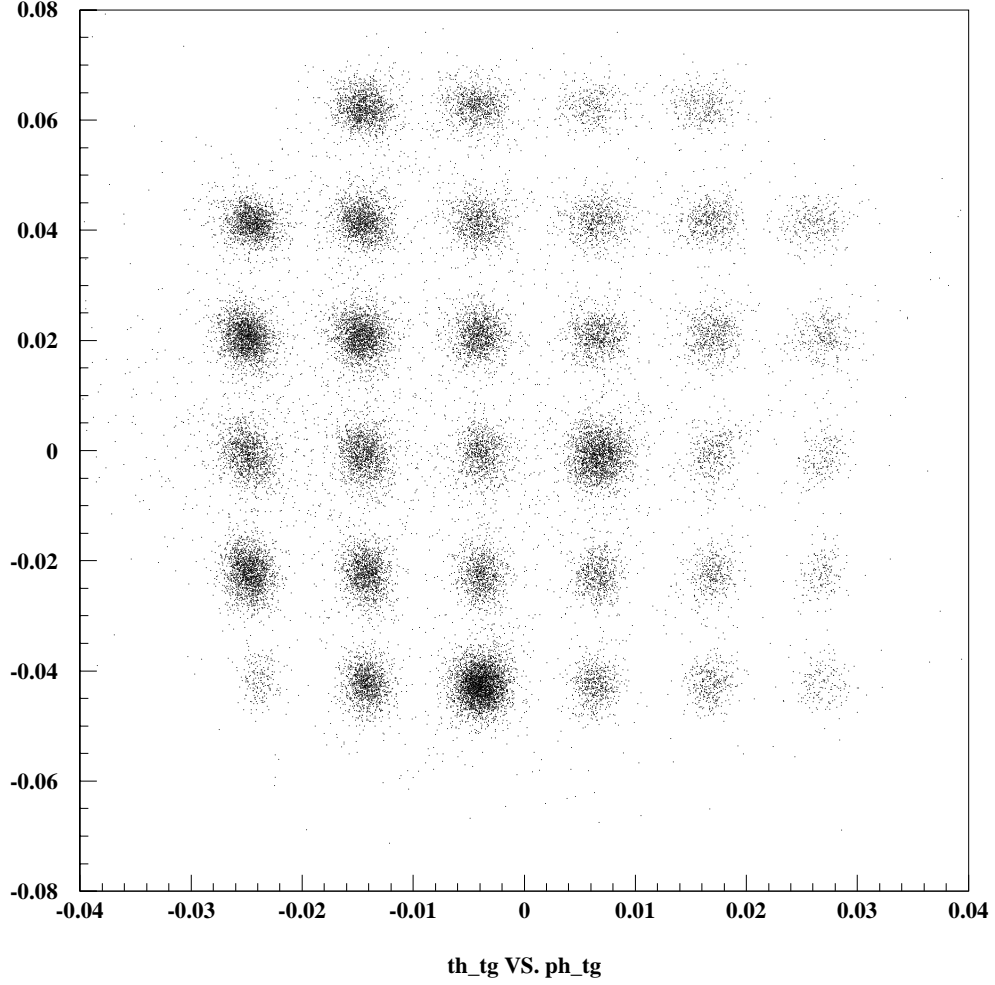


Figure 3-14: HRSE sieve slit image reconstructed using the matrix elements.

Figure 3-14 shows  $\theta_{tg}$  (y-axis) versus  $\phi_{tg}$  (x-axis) spectra for  $^{12}\text{C}(e, e')$  with a sieve slit installed in front of the HRSE. Note that the spectrometer central axis was not pointing at the target, and thus the sieve slit central hole was located at  $\phi_{tg} = 0.007$  and  $\theta_{tg} = 0$ . Another large hole (around  $\phi_{tg} = -0.004$  and  $\theta_{tg} = -0.043$ ) was used for identifying the orientation of the sieve slit.

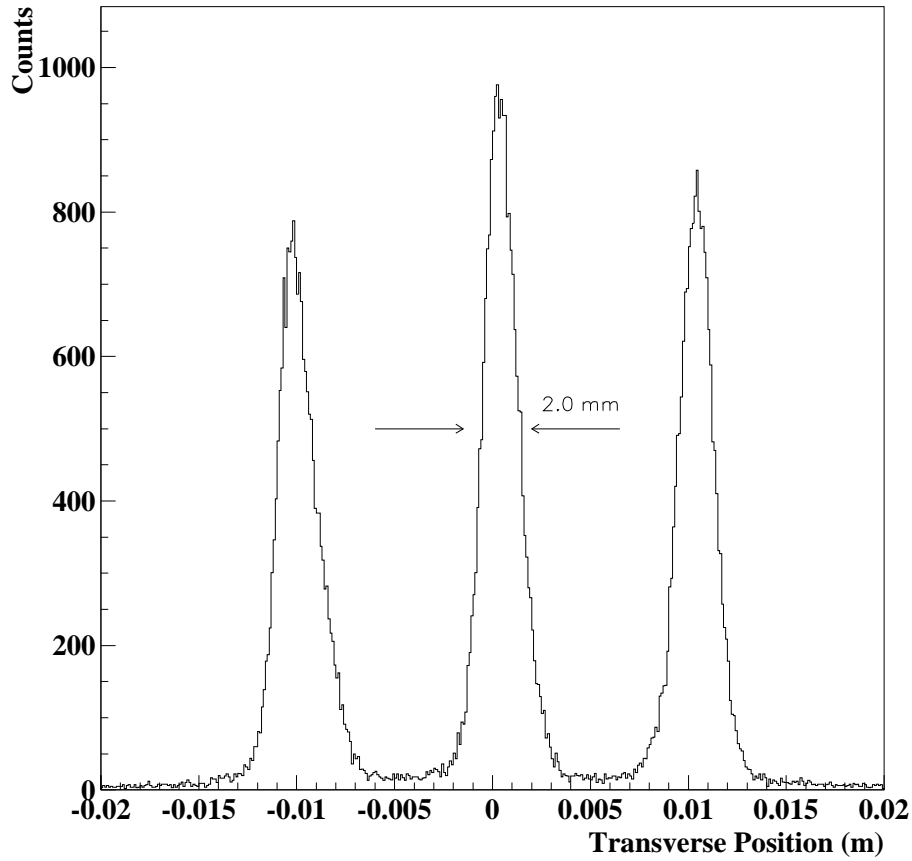


Figure 3-15: HRSE transverse position reconstruction for the three-foil waterfall target.

Figure 3-15 shows the reconstructed transverse position for the waterfall target with the HRSE matrix elements obtained from the optics study. The FWHM transverse position resolution is about 2 mm. The thickness of each foil along the beamline is about 1.3 mm. With the spectrometer sitting at  $23.38^\circ$ , the thickness of the foil is about 0.5 mm in the transverse direction. The three foils can be separated without overlap. The background events between the foils are due to scattering from the air inside the target can.

### 3.3.2 Absolute Momentum Measurement

The relation between the momentum of a particle passing through the spectrometer and the focal plane position is

$$P = \Gamma B [1 + \sum_{i=1}^2 d_i x_{fp}^i] \quad (3.34)$$

where  $B(\text{kG})$  is the dipole field strength,  $d_i (i = 1, 2)$  are the spectrometer dispersion coefficients,  $x_{fp}$  is the kinematically-corrected focal plane position, and  $\Gamma$  is the magnetic constant.

The spectrometer dispersion coefficients  $d_i (i = 1, 2)$  were calibrated by varying the dipole field while keeping the momentum  $P$  constant. To calibrate  $\Gamma$ , electron scattering from a thin carbon target ( $55.8 \text{ mg/cm}^2$ ) was used. For each state of  $^{12}\text{C}$ , the energy  $E_f$  is related to the corresponding excitation energy  $E_x$ , the incoming beam energy  $E_i$ , the mass of target  $M_t$ , and the scattering angle  $\theta$  by

$$E_f = \frac{E_i - E_{loss1} - E_x [1 + \frac{E_x}{2M_t}]}{1 + 2(E_i - E_{loss1}) \sin^2(\theta/2)/M_t} - E_{loss2} \quad (3.35)$$

where  $E_{loss1}$  and  $E_{loss2}$  are the mean energy losses before and after scattering. If the beam energy is known, extraction of  $\Gamma$  is very straightforward. However, since the beam energy was not known precisely enough, an alternative method using the first few states of  $^{12}\text{C}$  and the high momentum resolution of the spectrometers was developed [31]. The idea was to use the energy difference between these states which is known very precisely and can be measured very accurately at the focal plane (see Appendix A).

### 3.3.3 Coincidence Time-of-Flight

The Coincidence Time-of-Flight (CTOF) is the difference in time that one particle took to travel from the target to the focal plane of one spectrometer relative to the

time it took the other particle to travel from the target to the focal plane of the other spectrometer. The CTOF was measured by starting a TDC with the trigger of HRSH and stopping the TDC with the trigger of HRSE.

The CTOF allows for the distinction between a real coincidence event and an accidental coincidence event. A real coincidence event involves two particles emerging from the target at the same instant, and thus a narrow peak is expected in the CTOF spectrum. An accidental coincidence event is caused by two uncorrelated single arm events which fall within the coincidence timing gate, therefore, it will contribute to the continuous flat background in the CTOF spectrum. The ratio of the real coincidence events to the accidental coincidence events depends on the singles rates, and hence the beam current and target thickness. The larger this ratio, the more statistically precise the data. To narrow the width of the CTOF peak and thus increase the real-to-accidental coincidence ratio, several corrections were applied:

- Timing variations in the scintillators. The timing for a single arm trigger is determined by the right-hand side photomultiplier tubes (PMTs) of scintillator plane S2. Therefore, the timing fluctuates with the location of the particle in the S2 plane. This fluctuation can be compensated for by taking a mean-time in the software. The mean-time is the average of the two TDC values with an offset added to center the peak at zero

$$Meantime_i = (TDC_i^L + TDC_i^R)/2 + OFFSET_i. \quad (3.36)$$

The correction to the single arm timing is then given by

$$TDC_i^{corr} = TDC_i^{uncorr} + Meantime_i. \quad (3.37)$$

- Differences in flight-time and flight path-length. The flight-time from the target

to scintillator plane S2 for the central ray is

$$t_0 = \frac{l_0}{\beta_0} \quad (3.38)$$

where  $l_0$  is the path-length from the target to the S2 plane along the central ray ( $\sim 29$  m), and  $\beta_0$  is the velocity of the particle along this central ray. In general, the flight-time from the target to S2 along an arbitrary path through the spectrometer is

$$t = \frac{l_0 + \Delta l}{\beta} \quad (3.39)$$

where  $\Delta l$  is the change in the flight path-length from the central value, and  $\beta$  is the velocity. Thus, the correction to the CTOF for each spectrometer is

$$\Delta t = t - t_0 = l_0 \left( \frac{1}{\beta} - \frac{1}{\beta_0} \right) + \frac{\Delta l}{\beta} \quad (3.40)$$

$\Delta l$  is a function of  $(x_f, y_f, \theta_f, \phi_f)$  and is determined by the spectrometer optics.

- Vertex reconstruction. For a real coincidence event, the two spectrometers will reconstruct the same reaction vertex. Therefore, a cut condition that the two single arm events are from the same waterfall foil increases the real-to-accidental coincidence ratio.

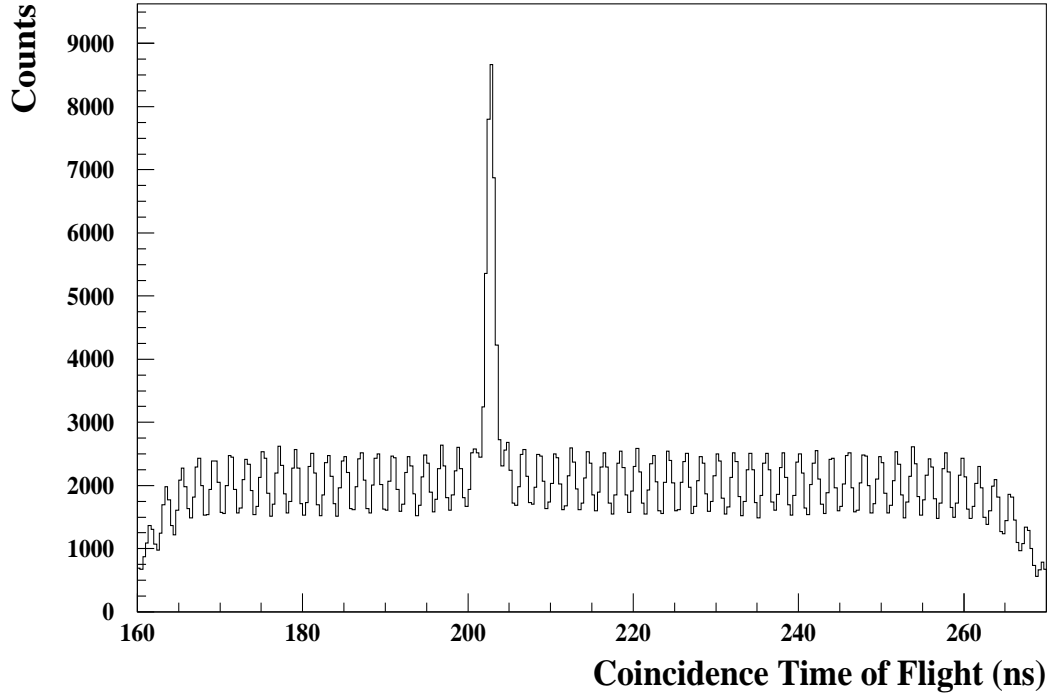


Figure 3-16: Corrected CTOF spectrum.

Figure 3-16 shows the corrected coincidence time-of-flight spectrum. The prominent peak at 206 ns is the real coincidence events, while the background is due to accidental coincidence events. The 2-ns, uniformly-distributed ripples are due to the beam current microstructure (499 MHz).

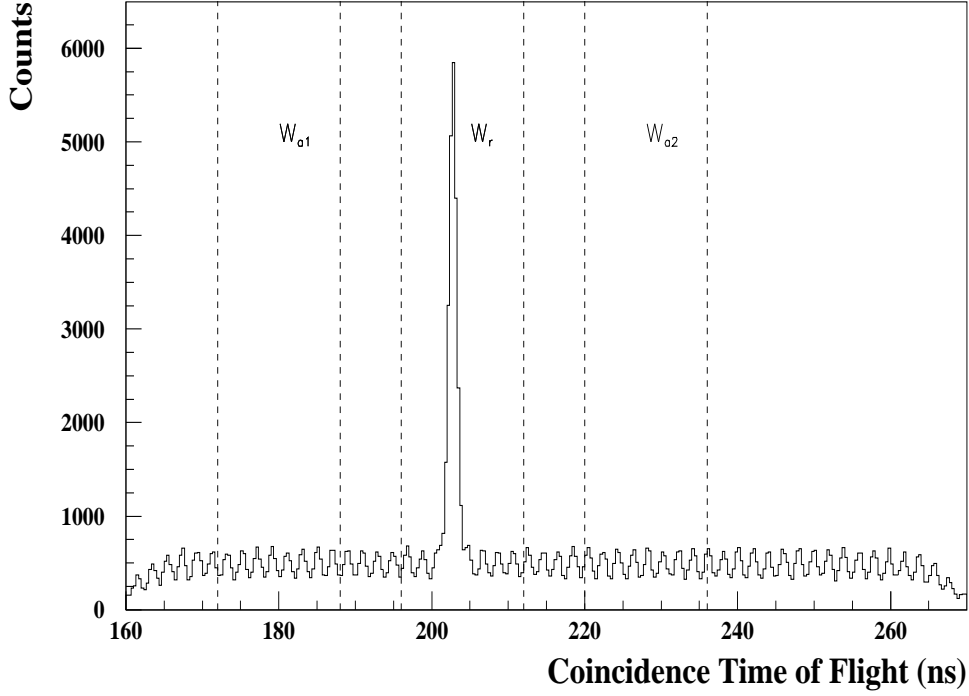


Figure 3-17: Corrected CTOF spectrum with two spectrometers reconstructing the same reaction vertex.

Figure 3-17 shows the corrected coincidence time-of-flight spectrum with the restriction that the two particles came from the same waterfall foil. The signal-to-noise ratio was increased dramatically. The corrected CTOF spectrum has been divided into several time windows for subtracting accidental coincidence events from the data (see Section 3.6). The time window  $W_r$  includes both real and accidental coincidence events, while the time windows  $W_{a1}$  and  $W_{a2}$  include purely accidental coincidence events.

### 3.3.4 Deadtime Correction

There are two deadtime corrections to be made to the data: an electronics deadtime correction and a computer deadtime correction.

Electronics deadtime is due to  $\tau$ , the time duration of the logic pulse passed to the scaler. If two independent pulses arrive at the scaler within a time interval shorter than  $\tau$ , then only one pulse may be recorded. Since the duration of the logic pulses passed to the scalers is less than 100 ns, and the maximum scaler rate for this experiment is a few kHz, so this effect is less than 1% and is neglected.

The computer deadtime refers to events not being recorded due to the fact that the data acquisition system can process at most one event within  $\sim 800 \mu\text{s}$ . This loss of events can be corrected by measuring the trigger input and the trigger output.

The setup of the trigger for this experiment is presented in the following table:

Trigger Type	Event Type	Scaler	Description
Input	N/A	$S_1$	HRSE fires
	N/A	$S_3$	HRSH fires
	N/A	$S_5$	HRSE & HRSH fire
Output	1	$T_1$	ONLY HRSE fires
	3	$T_3$	ONLY HRSH fires
	5	$T_5$	HRSE & HRSH fire

Table 3.1: A summary of trigger setup.  $S_5$  is included into  $S_1$  and  $S_3$ , while  $T_1$ ,  $T_3$ , and  $T_5$  are exclusive. N/A means not applicable.

For the trigger input, a coincidence event is also recorded as two single arm events. Therefore,  $S_5$  is included within  $S_1$  and  $S_3$ . For the trigger output, a coincidence event is not recorded as two single arm events. Thus  $T_1$ ,  $T_3$ , and  $T_5$  are exclusive.

With the deadtime correction taken into account, the total number of HRSE single arm  $(e, e')$  events  $N_{total}^{(e, e')}$  is given by

$$N_{total}^{(e, e')} = \frac{S_1 - S_5}{T_1} N_1^{(e, e')} + \frac{S_5}{T_5} N_5^{(e, e')} \quad (3.41)$$

where  $N_1^{(e, e')}$  is the number of  $(e, e')$  events written to tape as event type 1, and  $N_5^{(e, e')}$

is the number of  $(e, e')$  events written to tape as event type 5. Similarly, the total number of HRS single arm  $(e, p)$  events,  $N_{total}^{(e,p)}$  (after the deadtime correction) is

$$N_{total}^{(e,p)} = \frac{S_3 - S_5}{T_3} N_3^{(e,p)} + \frac{S_5}{T_5} N_5^{(e,p)} \quad (3.42)$$

where  $N_3^{(e,p)}$  is the number of  $(e, p)$  events written to tape as event type 3, and  $N_5^{(e,p)}$  is the number of  $(e, p)$  events written to tape as event type 5. For coincidence events, the deadtime correction is different. The total number of coincidence  $(e, e'p)$  events after the deadtime correction is

$$N_{total}^{(e,e'p)} = \frac{S_5}{T_5} N_5^{(e,e'p)} \quad (3.43)$$

where  $N_5^{(e,e'p)}$  is the number of  $(e, e'p)$  events written to tape as event type 5.

Unfortunately, during the experiment,  $S_5$  was found to be overcounting for some of the 2445 MeV runs. A simple model was used to calculate the deadtime. During this experiment, a large prescale factor ( $\geq 30$ ) was set on  $S_3$  such that the rate for  $T_3$  was less than 10 Hz. Because the large prescale factor acted as a counting clock, the contribution to the deadtime correction of  $T_3$  only came from  $T_1$  and  $T_5$ . The fraction of deadtime for  $T_3$  is

$$dt3 = \dot{T}_1 \Delta t_1 + \dot{T}_5 \Delta t_5 = 1 - \frac{p_3 T_3}{S_3 - S_5}. \quad (3.44)$$

Here  $\Delta t_1$  and  $\Delta t_5$  are the time durations needed for the computer to process a  $T_1$  or  $T_5$  event respectively. Since the prescale factor for  $T_5$  was always set at unity, the contribution to the deadtime correction of  $T_5$  came from  $T_1$ ,  $T_3$ , and  $T_5$ . The fraction of deadtime for  $T_5$  is

$$dt5 = \dot{T}_1 \Delta t_1 + \dot{T}_3 \Delta t_3 + \dot{T}_5 \Delta t_5. \quad (3.45)$$

Here  $\Delta t_3$  is the time duration needed for the computer to process a  $T_3$  event, and  $\dot{T}_3$

is the rate for  $T_3$ . By combining the previous two equations, and noting that  $S_3$  is much larger than  $S_5$ , one gets,

$$dt5 = 1 - \frac{p_3 T_3}{S_3 - S_5} + \dot{T}_3 \Delta t_3 \approx 1 - \frac{p_3 T_3}{S_3} + \dot{T}_3 \Delta t_3. \quad (3.46)$$

Thus, the deadtime correction factor for coincidence events is

$$1/(1 - dt5) = 1/(\frac{p_3 T_3}{S_3} - \dot{T}_3 \Delta t_3). \quad (3.47)$$

$\Delta t_3$  was about 800  $\mu\text{s}$  with an uncertainty of 200  $\mu\text{s}$ . This uncertainty was taken as a systematic error for the deadtime correction which was less than 0.2%.

## 3.4 Spectrometer Efficiency

### 3.4.1 Focal Plane Relative Efficiency

Since the focal plane is not uniformly efficient, its relative efficiency profile must be characterized. The relative efficiency  $\epsilon$  is a function of  $\theta_{tg}$ ,  $\phi_{tg}$ , and  $\delta$ . If a  $\sim 5$  msr collimator is applied,  $\epsilon$  depends only upon  $\delta$ . Because of the similar optical properties, both the HRSE and HRSB are expected to have essentially the same relative efficiency profiles.

The basic idea behind the measurement of the relative efficiency profile for a spectrometer requires a measurement of the same cross section at different positions across the focal plane. Variations of the measured cross section across the focal plane are due to changes of the relative efficiency. In the summer of 1997, for both spectrometers,  $^{16}\text{O}(e, e')$  and  $^{16}\text{O}(e, p)$  spectra in the region where the cross section changes smoothly as a function of  $(\omega, q)$  were measured at 5 different central momenta. A program RELEFF [32] was used to deconvolute the focal plane efficiency from the  $(e, e')$  and  $(e, p)$  spectra. RELEFF approximates the cross section as the sum of

polynomials  $f_n$  up to order  $n$

$$\sigma_{ij} = \sum_n a_n f_n(p_{ij}) \quad (3.48)$$

where  $\sigma_{ij}$  is the cross section and  $p_{ij}$  is the momentum of the  $i^{th}$  channel for the  $j^{th}$  measurement. The polynomials  $f_n$  can be either regular polynomials of the form  $x^n$  or Legendre polynomials. Here, the Legendre polynomials were used.  $\chi^2$  was defined as

$$\chi^2 = \sum_{ij} w_{ij} (C_{ij} - N_j \sigma_{ij} \epsilon_i)^2 \quad (3.49)$$

where  $C_{ij}$  was the number of counts,  $w_{ij}$  was the statistical weight in channel  $i$  for run  $j$ ,  $N_j$  was the normalization factor for run  $j$ , and  $\epsilon_i$  was the relative efficiency of channel  $i$ . Here,  $N_j$  was an arbitrary number which was proportional to the luminosity and inversely proportional to the deadtime correction factor. An iterative procedure was used to determine  $\epsilon_i$  and the coefficients  $a_n$ . The  $\epsilon_i$  were initialized at unity and  $\chi^2$  minimized with respect to  $\{a_n\}$  such that

$$\frac{\partial \chi^2}{\partial a_n} = 0, \quad \forall a_n. \quad (3.50)$$

This resulted in  $n$  linear equations which unambiguously characterized  $\{a_n\}$

$$X_n - \sigma_n M_{nn} a_n = 0 \quad (3.51)$$

where

$$X_n = \sigma_{ij} w_{ij} C_{ij} \epsilon_i N_j f_n(p_{ij}) \quad (3.52)$$

and

$$M_{mn} = \sigma_{ij} w_{ij} (\epsilon_i N_j)^2 f_m(p_{ij}) f_n(p_{ij}). \quad (3.53)$$

The coefficients  $a_m$  were determined by calculating  $M^{-1}X$ . Using these coefficients, new efficiencies were computed according to

$$\epsilon_i = \frac{\sum_j C_{ij}}{\sum_j \sum_n N_j a_n f_n(p_{ij})}. \quad (3.54)$$

The  $\epsilon_i$  so determined were then put back into Equation 3.49. This procedure was repeated until  $\chi^2$  converged. This condition enforced the convergence of  $\epsilon_i$  and  $a_n$ .

The three foils for the waterfall target were treated separately, since they cover different regions in solid angle (see Figure 3-18). Figure 3-19 shows the HRSE  $\theta_{tg}$  and  $\phi_{tg}$  spectra for the central foil. There is an (almost) uniform region between the two vertical lines in the  $\theta_{tg}$  plot. Since the cross section is almost independent of  $\theta_{tg}$ , the two lines in the  $\theta_{tg}$  plot define the “flat” acceptance region in  $\theta_{tg}$ . In the  $\phi_{tg}$  plot, the counting rate drops smoothly as a function of  $\phi_{tg}$  between the two vertical lines due to the change in cross section, while outside this region, the counting rate falls off dramatically due to the sudden drop in the acceptance in  $\phi_{tg}$ . Therefore, the two lines in the  $\phi_{tg}$  plot define the “flat” acceptance region in  $\phi_{tg}$ . Different cuts on solid angle were applied for different foils such that within the different solid angle regions, all the particles with essentially the central momentum ( $dp/p = 0$ ) could reach the focal plane with the equal probability. For the central foil, this solid angle was 4.75 msr, while for the side foil, the solid angle varied depending upon the spectrometer angle. Therefore the relative efficiency presented here is basically the product of the momentum acceptance of the spectrometer and the overall efficiency of the focal plane. The relative efficiency profiles of the HRSE and the HRSB are given in Figure 3-20 and Figure 3-21 respectively. Cuts on the solid angle used for calculating the

relative efficiencies are listed in Table 3.2.

HRSE	Foil 1	$-0.05 < \theta_{tg} < 0.045, -0.019 < \phi_{tg} < 0.024$
	Foil 2	$-0.05 < \theta_{tg} < 0.045, -0.026 < \phi_{tg} < 0.024$
	Foil 3	$-0.05 < \theta_{tg} < 0.045, -0.026 < \phi_{tg} < 0.015$
HRSH	Foil 1	$-0.05 < \theta_{tg} < 0.05, -0.022 < \phi_{tg} < 0.013$
	Foil 2	$-0.05 < \theta_{tg} < 0.05, -0.022 < \phi_{tg} < 0.022$
	Foil 3	$-0.05 < \theta_{tg} < 0.05, -0.005 < \phi_{tg} < 0.022$

Table 3.2: Cuts applied on the soild angle for the different foils. The HRSE was at  $23.38^\circ$ , and the HRSH was at  $46.45^\circ$ . Foil 1 was the downstream foil.

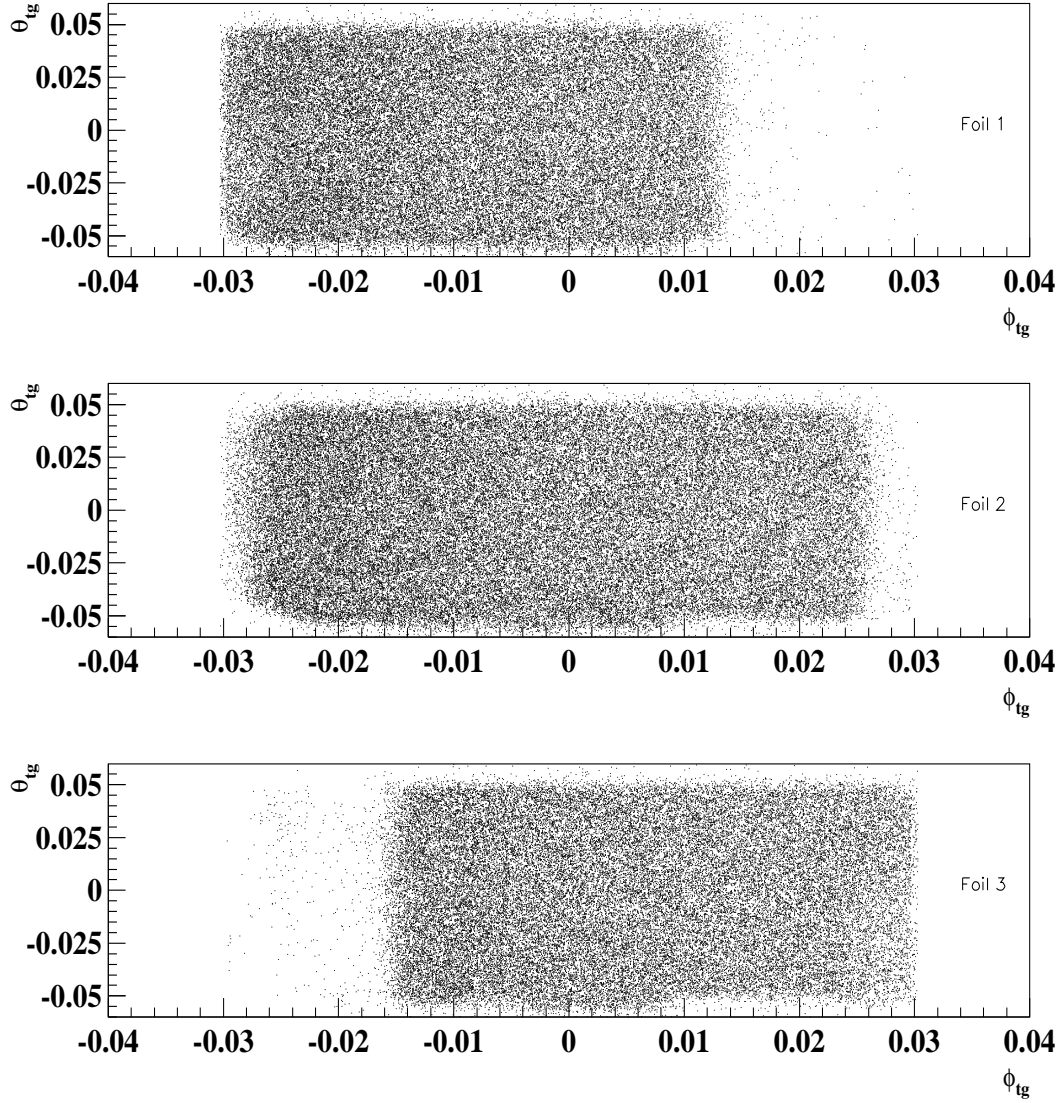


Figure 3-18:  $\theta_{tg}$  vs  $\phi_{tg}$  for the three different foils. The data taken were  $^{16}\text{O}(e, e')$ . The electron beam energy was 1642.5 MeV, and the scattering angle was  $37.17^\circ$ .

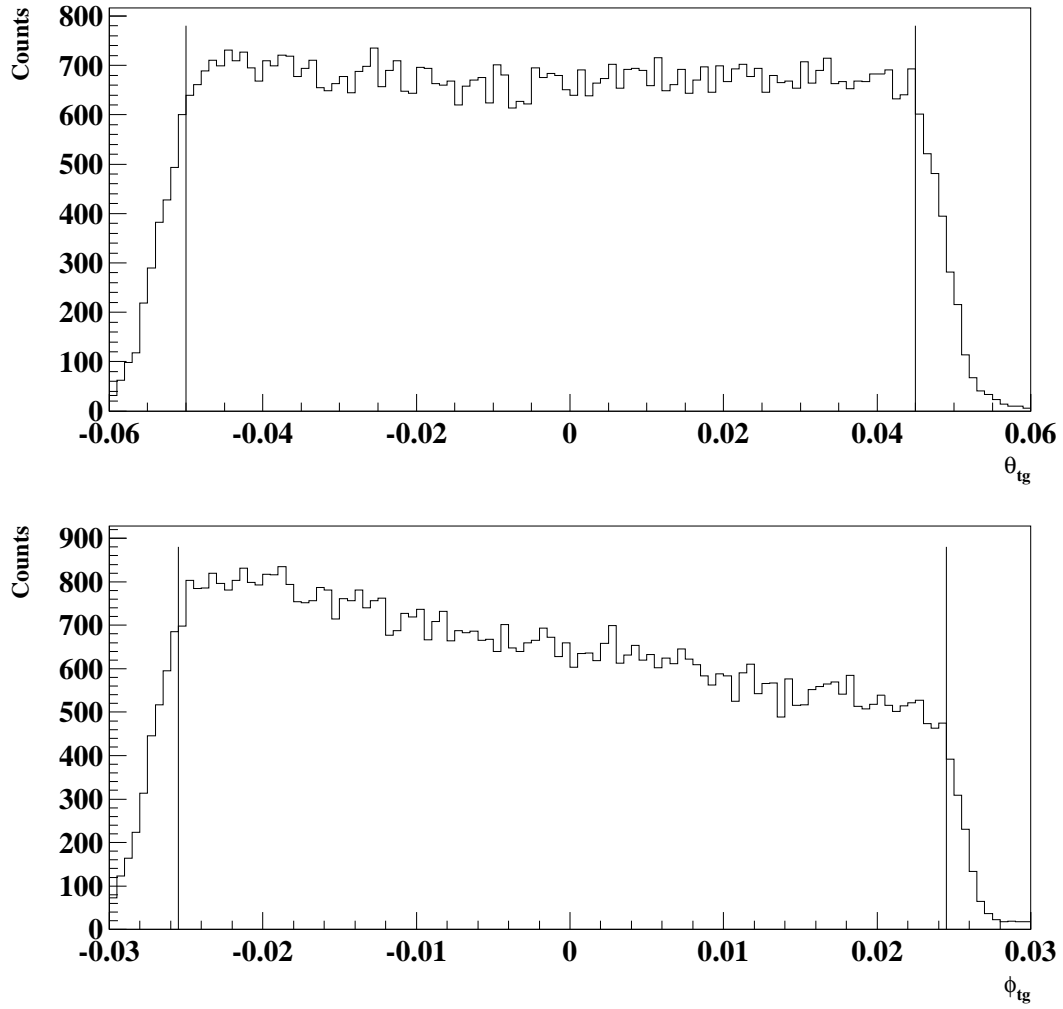


Figure 3-19: HRSE  $\theta_{tg}$  and  $\phi_{tg}$  spectra for the central foil. The ranges within the vertical lines define the “flat” acceptance region in solid angle. For the side foils, the flat solid angle region varies depending upon the angular position of the spectrometer.

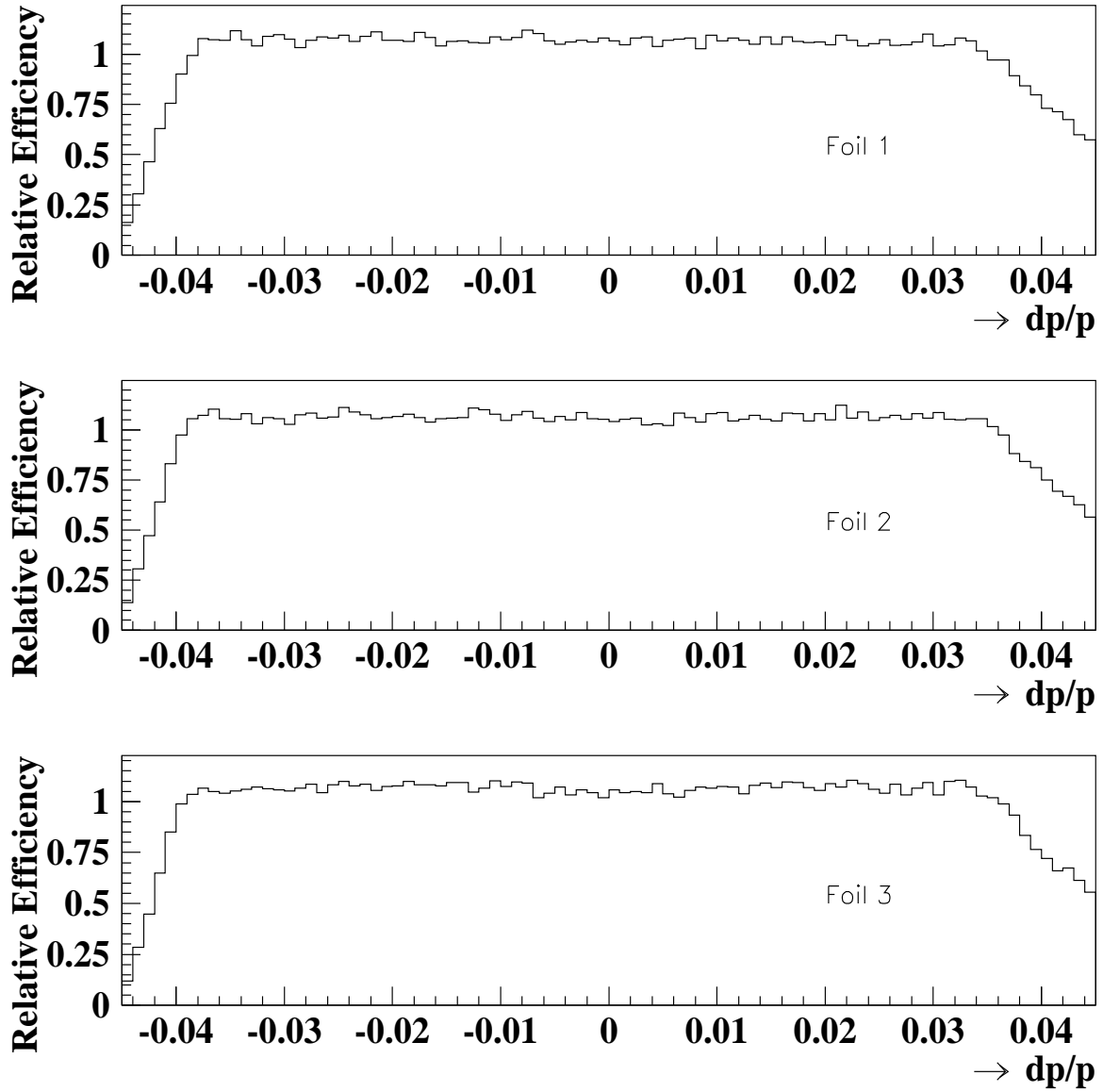


Figure 3-20: Relative efficiency profile of the HRSE for the three water foils. The HRSE was at  $23.38^\circ$ . The solid angles covered by the foils are listed in Table 3.2.

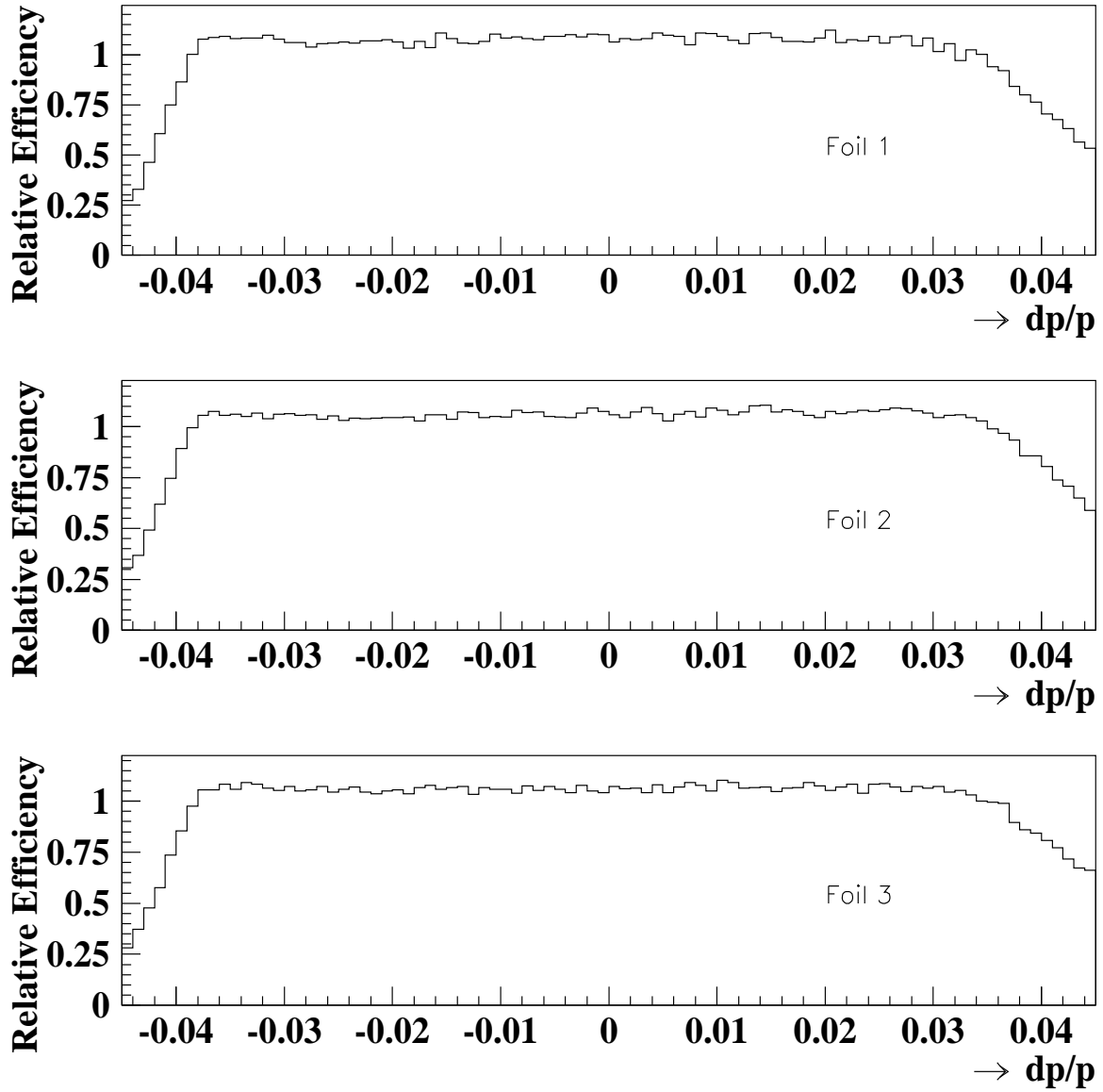


Figure 3-21: Relative efficiency profile of the HRSH for the three water foils. The HRSH was at  $46.45^\circ$ . The solid angles covered by the foils are listed in Table 3.2.

### 3.4.2 Normalization

Measurement of the cross section for the  $(e, e'p)$  reaction requires knowledge of the luminosity  $l$  and the overall coincidence efficiency  $\epsilon$ , where

$$\epsilon = \epsilon_e \epsilon_p \epsilon_{coin}. \quad (3.55)$$

Here  $\epsilon_e$  is the electron single arm efficiency,  $\epsilon_p$  is the proton single arm efficiency, and  $\epsilon_{coin}$  is the coincidence trigger efficiency. In this experiment,  $\epsilon_{coin}\epsilon_p$  was measured with the  $H(e, e'p)$  reaction, while  $l\epsilon_e$  was determined using  $H(e, e')$ .

$H(e, e'p)$  is a two-body reaction. Thus, once the outgoing electron is detected, the momentum and direction of the corresponding proton is known. If this proton is within the acceptance of the hadron arm but not detected, an inefficient event has occurred. The data taken with the HRSH along  $\vec{q}$  at  $E_{beam} = 843.2$  MeV was used for the measurement of  $\epsilon_p\epsilon_{coin}$ . The HRSE was at  $100.7^\circ$ , while the HRSH was at  $23.2^\circ$ . The angular spread of scattered electrons was about 2.5 times as large as the angular spread of protons in both the vertical and transverse directions. The central momenta of both spectrometers were set so that the electrons and protons from the  $H(e, e'p)$  reaction would be detected in the flat efficiency region of the focal plane. There was no prescaling for electron single arm events or coincidence events. A rigid cut was made on the electron arm solid angle to ensure that the proton from each  $H(e, e'p)$  event would reach the focal plane. The following procedure was then applied to obtain  $\epsilon_p\epsilon_{coin}$ :

- A histogram of the kinematically-corrected relative momentum for the coincidence events (Figure 3-22a) was generated.
- A histogram of the kinematically-corrected relative momentum for the electron single arm events (Figure 3-22b) was generated.
- A polynomial was used to fit the background of Figure 3-22b, and the background

was then subtracted (Figure 3-22c).

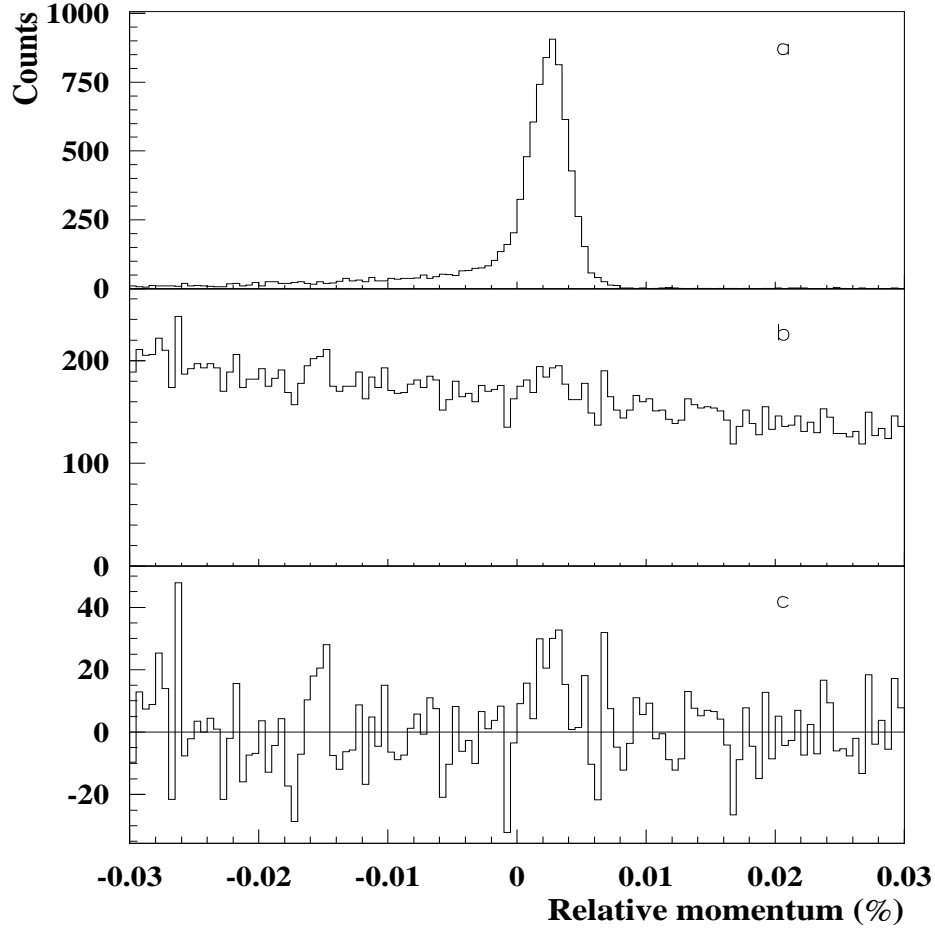


Figure 3-22: Kinematically-corrected relative momentum spectra for  $H(e, e'p)$ . Plot a is for the coincidence events, plot b is for the electron single arm events, and plot c is obtained from plot b after the background subtraction.

The ratio of the integration over the elastic peak range of Figure 3-22c to that for Figure 3-22a is about 1.1%, which indicates that  $\epsilon_p \epsilon_{coin}$  is 98.9%. This inefficiency is reasonably consistent with proton absorption in the material it traverses on the way to the focal plane, as well as the inefficiency in the trigger electronics.

The total number of  $H(e, e')$  events ( $N_H$ ) after deadtime and radiative corrections

applied is

$$N_H = 2l\epsilon_e\sigma_{H(e,e')} \quad (3.56)$$

where the factor of two is due to two protons in each water molecule, and  $\sigma_{H(e,e')}$  is the integrated  $H(e, e')$  cross section. The total number of  $H(e, e')$  events was obtained using the program ALLFIT [33][53]. For the data with the HRSH along  $\vec{q}$ , the peak corresponding to  $H(e, e')$  sits on top of quasielastic peak. ALLFIT was used to fit the  $^{16}\text{O}(e, e')$  background using 4th-order polynomials, integrate the  $H(e, e')$  events, and simultaneously perform the radiative corrections.

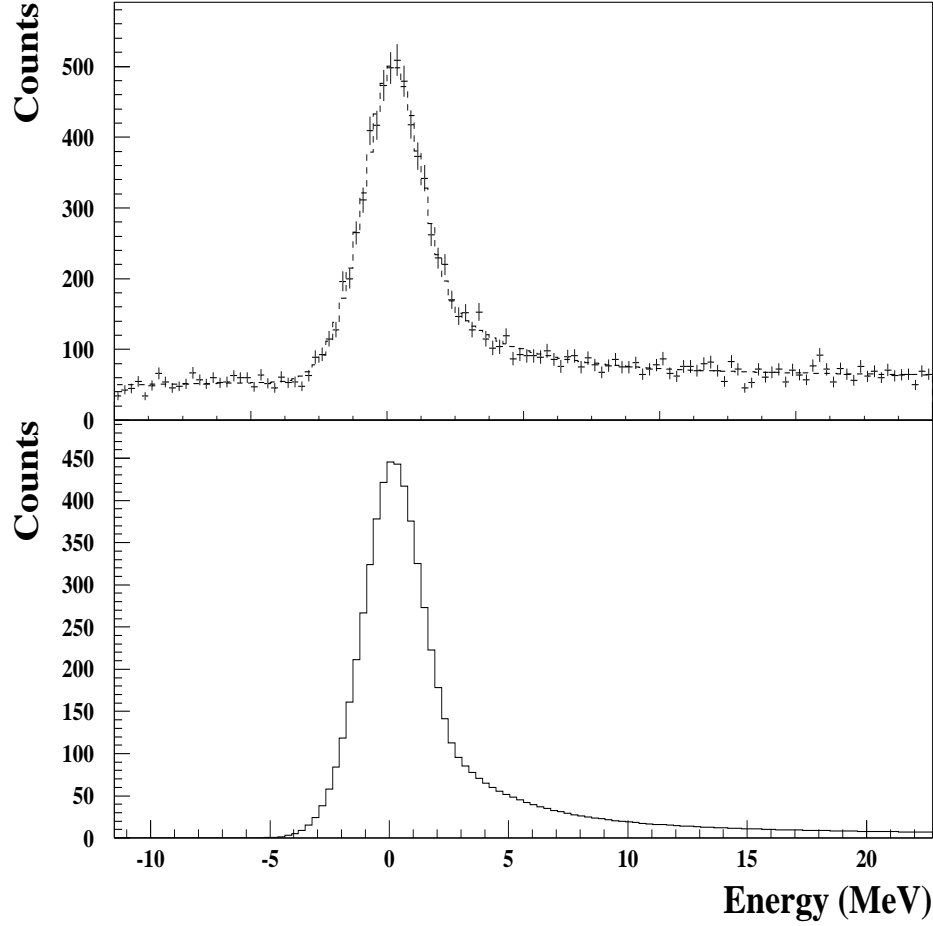


Figure 3-23: Energy transfer spectra for  $H(e, e')$ . The top plot includes quasielastic  $^{16}\text{O}(e, e')$  events, while the bottom plot is obtained after the  $^{16}\text{O}(e, e')$  background is subtracted using ALLFIT [33][53].

The Mainz parametrization [34] for the  $H(e, e')$  cross section was used for normalization

$$\frac{d\sigma}{d\Omega_e} = \frac{\sigma_M}{1 + \frac{2E_i}{M_p} \sin^2 \frac{\theta_e}{2}} \left( \frac{G_E^2 + \tau G_M^2}{1 + \tau} + 2\tau G_M^2 \tan^2 \frac{\theta_e}{2} \right) \quad (3.57)$$

where  $\sigma_M$  is the Mott cross section,  $\theta_e$  is the electron scattering angle,  $E_i$  is the

incident electron beam energy,  $M_p$  is the mass of proton,  $\tau = Q^2/4M_p^2$ , and  $G_E$  and  $G_M$  are the proton electric and magnetic form factors

$$G_E(Q^2) = \frac{0.312}{1 + Q^2/6.0} + \frac{1.312}{1 + Q^2/15.02} - \frac{0.709}{1 + Q^2/44.08} + \frac{0.085}{1 + Q^2/154.2} \quad (3.58)$$

$$\frac{G_M(Q^2)}{\mu} = \frac{0.694}{1 + Q^2/8.5} + \frac{0.719}{1 + Q^2/15.02} - \frac{0.418}{1 + Q^2/44.08} + \frac{0.005}{1 + Q^2/355.4} \cdot \quad (3.59)$$

The cross section integrated over solid angle was calculated. Using this method, the product of the luminosity and the absolute detection efficiency for electrons ( $l\epsilon_e$ ) was obtained for each run.

### 3.4.3 Waterfall Foil Thickness

The thickness of the three waterfall foils was measured once during the experiment. First, by comparing  $^{16}\text{O}(e, e')$  at  $|\vec{q}| = 330 \text{ MeV}/c$  from a solid BeO target to that obtained from the waterfall target, this thickness of the center foil was determined. The thickness of the solid BeO target was  $155.0 \pm 1.5 \text{ mg}/\text{cm}^2$ . By comparing  $\text{H}(e, e')$  from the central foil to the two side foils, the thickness of the side foils was determined. The thickness (along the beam line) of the three foils is presented in Table 3.3.

Foil number	1	2	3
Thickness ( $\text{mg}/\text{cm}^2$ )	$128.8 \pm 3.2$	$130.5 \pm 2.7$	$130.7 \pm 3.3$

Table 3.3: Waterfall foil thickness.

## 3.5 Phase Space Volume Calculation

Cross section is a function of the phase space variables  $\omega$ ,  $Q^2$ ,  $E_{miss}$ , and  $P_{miss}$ . Experimentally, the data were acquired with a finite acceptance. This means the measured cross section is always a cross section averaged over a certain phase space range. The number of counts within the bin  $B(\Delta\omega, \Delta Q^2, \Delta E_{miss}, \Delta P_{miss})$  after the corrections

for deadtime and luminosity have been applied is given by

$$\begin{aligned}
 N_B &= \int_B \frac{d^6\sigma}{d\omega d\Omega_e dE_{miss} d\Omega_p} \epsilon_A d\omega d\Omega_e dE_{miss} d\Omega_p \\
 &= \left\langle \frac{d^6\sigma}{d\omega d\Omega_e dE_{miss} d\Omega_p} \right\rangle_B \int_B \epsilon_A d\omega d\Omega_e dE_{miss} d\Omega_p
 \end{aligned} \tag{3.60}$$

where  $\epsilon_A$  is the six-dimensional efficiency function within the bin  $B$ , and the integration is over the acceptance of the spectrometers. The cross section determined experimentally is

$$\left\langle \frac{d^6\sigma}{d\omega d\Omega_e dE_{miss} d\Omega_p} \right\rangle_B = \frac{N_B}{V_B} \tag{3.61}$$

where the phase space volume is defined by

$$V_B = \int_B \epsilon_A d\omega d\Omega_e dE_{miss} d\Omega_p. \tag{3.62}$$

The measured cross section approaches the theoretical cross section when the latter does not vary within  $B$  or the size of  $B \rightarrow 0$ .

To calculate the phase space volume, the spectrometer efficiency function  $\epsilon_A$  must be known very well. Both the HRSE and HRSB have the feature that the acceptance is flat over approximately 5 msr of solid angle ( $-3.7\%$  to  $+3.3\%$  in  $dp/p$ ). Thus, over this region,  $\epsilon_A$  is just the overall efficiency of the two spectrometers ( $\epsilon_e \epsilon_p \epsilon_{coin}$ ). For this restricted acceptance, the phase space volume can be rewritten as

$$V_B = \epsilon_A V'_B = \epsilon_A \int_B J d\omega d\Omega_e dT_p d\Omega_p \tag{3.63}$$

where  $J$  is the Jacobian

$$\begin{aligned}
J &= \left| \frac{\partial E_{miss}}{\partial T_p} \right| \\
&= \left| \frac{\partial E_{miss}}{\partial p_p} \left[ \frac{\partial p_p}{\partial T_p} \right] \right| \\
&= \left| 1 - \frac{E_p}{E_{rec}} \left( \frac{\vec{p}_p \cdot \vec{p}_{miss}}{p_p^2} \right) \right| \\
&= \left| 1 + \frac{E_p}{E_{rec}} \left( 1 - \frac{q}{p_p} \cos \theta_{pq} \right) \right|.
\end{aligned} \tag{3.64}$$

Note that the Jacobian is essentially unity for the kinematics of this experiment.

A Monte Carlo approach has been taken to calculate the phase space volume.  $N_0$  random samples of  $E_f, \theta_{tg}^e, \phi_{tg}^e, T_p, \theta_{tg}^p$ , and  $\phi_{tg}^p$  are generated within the flat acceptance region of the spectrometers and from these variables, the kinematic quantities  $\omega, Q^2, E_{miss}$  and  $P_{miss}$  are calculated. The number of events  $N_\Delta$  that fall into the bin  $B(\Delta\omega, \Delta Q^2, \Delta E_{miss}, \Delta P_{miss})$  is noted. The phase space volume for the bin  $B$  is thus just

$$V_B = \epsilon_A V'_B = \epsilon_A \frac{N_\Delta}{N_0} \Delta E_f \Delta \Omega_e \Delta T_p \Delta \Omega_p. \tag{3.65}$$

### 3.6 Cross Section Calculation

After all the individual runs were analyzed with ESPACE, the data was sorted into four-dimensional bins  $(\Delta\omega, \Delta Q^2, \Delta E_{miss}, \Delta P_{miss})$ . For each bin, the accidental coincidence events were subtracted from the data. Figure 3-17 shows the corrected CTOF spectrum.  $W_r$  is the width of the time window which covers the prompt peak and the number of events in this region is  $N_r$ .  $W_{a1}$  and  $W_{a2}$  are the widths of the two time windows used for the determination of the number of accidental coincidence events under the prompt peak. The total number of events in these two regions is  $N_a$ . The

number of true coincidence events  $N_t$  is then given by

$$N_t = N_r - N_a \frac{W_r}{W_{a1} + W_{a2}} \quad (3.66)$$

and  $\delta N_t$ , the standard error of  $N_t$  is

$$\delta N_t = \sqrt{N_r^2 + N_a^2 \left( \frac{W_r}{W_{a1} + W_{a2}} \right)^2}. \quad (3.67)$$

The cross section for each  $(\Delta\omega, \Delta Q^2, \Delta E_{miss}, \Delta P_{miss})$  bin is obtained using

$$\left\langle \frac{d^6\sigma}{d\omega d\Omega_e dE_{miss} d\Omega_p} \right\rangle = \frac{\sum_i f_{dt}^i N_t^i(\Delta\omega, \Delta Q^2, \Delta E_{miss}, \Delta P_{miss})}{\sum_i l_i \epsilon_e \epsilon_p \epsilon_{coin} V'(\Delta\omega, \Delta Q^2, \Delta E_{miss}, \Delta P_{miss})} \quad (3.68)$$

where

$f_{dt}^i$  is the deadtime correction factor for run  $i$ ,

$N_t^i$  is the number of true coincidence events from run  $i$ ,

$l_i \epsilon_e$  is the product of the luminosity and the HRSE efficiency for run  $i$  (calculated from  $H(e, e')$ ),

$\epsilon_p \epsilon_{coin}$  is the product of the coincidence trigger efficiency and the HRSH efficiency,  
and

$V'$  is the phase space volume (see Equation 3.63) for bin  $(\Delta\omega, \Delta Q^2, \Delta E_{miss}, \Delta P_{miss})$ .

### 3.7 Radiative Corrections

The electron and proton radiate in the electromagnetic field. The emission and re-absorption of virtual photons corresponds to the vertex correction, mass renormalization, and vacuum polarization of the exchanged photon, and therefore changes the cross section. The radiation of a real photon not only changes the cross section, but also changes the energy and momentum transfer in the  $(e, e'p)$  reaction. Thus, to

compare the measured results directly to a theoretical calculation, it is very important to properly unfold the radiative processes from the data.

### 3.7.1 Theory of Radiative Corrections

Three processes are considered for radiative corrections:

- Internal bremsstrahlung (Schwinger correction [35]), in which the electron radiates real or virtual photons while it interacts with the Coulomb field of the nucleus involved in the  $(e, e'p)$  reaction.
- External bremsstrahlung, in which the electron radiates while it interacts with the Coulomb field of a nucleus other than the one involved in the  $(e, e'p)$  reaction.
- Landau straggling, in which the electron or proton loses energy due to the ionization of the target atoms.

Internal bremsstrahlung, which was first calculated by Schwinger [35] and later improved by Mo and Tsai [36][37], has the largest overall contribution to the radiative correction. These processes are diagrammed in Figure 3-24. Diagrams a and b correspond to the emission of a real photon from the electron before and after the interaction, respectively. If the energy of the real photon ( $E_\gamma$ ) is larger than the cutoff energy  $\Delta E_m$ , then the resulting event will end up in the radiative tail of the missing energy spectrum. In effect, a correction must be made to relocate the event back to the bin in which it should have been registered. Thus, the contribution to the internal bremsstrahlung correction arising from these diagrams depends on the cutoff energy  $\Delta E_m$  - the larger the  $\Delta E_m$ , the smaller the correction. Diagrams c and d correspond to the emission and re-absorption of a virtual photon by the incident or scattered electron, which results in the renormalization of the electron mass. Diagram e shows emission of a virtual photon by the incident electron and reabsorption by the scattered electron. The missing energy of this event is unchanged; however, the 4-

momentum of the exchanged virtual photon is different. This process amounts to an overall renormalization of the vertex, and thus it changes the cross section. Diagram f results in the renormalization of the virtual photon due to the vacuum polarization.

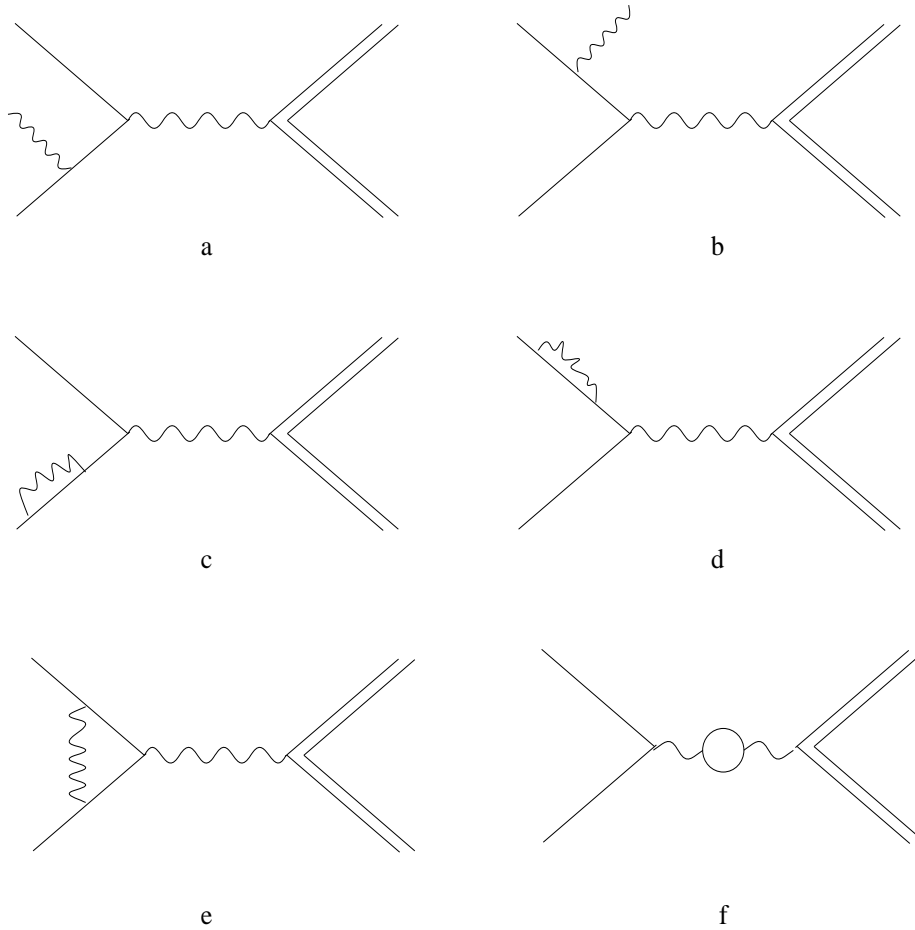


Figure 3-24: Feynman diagrams for internal bremsstrahlung. Diagram a and b correspond to the emission of a real photon from the electron before and after the interaction, respectively. Diagram c and d result in the renormalization of the electron mass. Diagram e amounts to an overall renormalization of the vertex. Diagram f results in the renormalization of the virtual photon due to the vacuum polarization.

The program RADCOR [38][39] uses the formalism proposed by Penner [40] based on [37] for the Schwinger correction. The measured cross section and the cross section with internal bremsstrahlung effects included are related by

$$\sigma_{Schw} = \sigma_{exp} f_{Schw}. \quad (3.69)$$

The correction factor  $f_{Schw}$  is given by

$$f_{Schw} = \frac{e^{\delta_{real}}}{1 - \delta_{virtual}} \quad (3.70)$$

where

$$\delta_{real} = \frac{\alpha}{\pi} \ln\left(\frac{E_i E_f b}{\eta^2 \Delta E_m^2}\right) \left\{ \ln\left(\frac{Q^2}{m_e^2}\right) - 1 \right\} \quad (3.71)$$

$$\delta_{virtual} = -\frac{\alpha}{\pi} \left\{ \frac{13}{6} \left[ \ln\left(\frac{Q^2}{2}\right) - 1 \right] - \frac{17}{18} - \frac{\pi^2}{6} - \frac{1}{2} \ln^2\left(\frac{E_i}{E_f}\right) + L_2(\cos^2 \frac{\theta_e}{2}) \right\} \quad (3.72)$$

with

$$b = 1 + \frac{2\omega}{M} \sin^2\left(\frac{\theta_e}{2}\right) \quad (3.73)$$

$$\eta = 1 + \frac{2E_i}{M} \sin^2\left(\frac{\theta_e}{2}\right) \quad (3.74)$$

and  $L_2$  is the Spence function

$$L_2(x) = - \int_0^x \frac{\ln(1-y)}{y} dy. \quad (3.75)$$

The internal bremsstrahlung described above does not depend upon target thickness. However, with external bremsstrahlung, the electron radiates due to the interactions with the Coulomb field of nuclei other than the nucleus involved in the  $(e, e'p)$  reaction. Therefore, this effect does depend on the amount of material through which the electron passes. The formalism for external bremsstrahlung in RADCOR is given

by Friedrich [41]. The correction factor for external bremsstrahlung,  $f_{ext}$  is

$$f_{ext} = \exp\left\{\frac{t}{X_0}\left[-\left(\zeta - \frac{1}{2}\right) + \zeta \ln\left(\frac{\epsilon}{\Delta E_m}\right) + \zeta \frac{\Delta E_m}{\epsilon} - \frac{1}{2}\left(\frac{\Delta E_m}{\epsilon}\right)^2\right]\right\} \quad (3.76)$$

where

$t$  [g/cm<sup>3</sup>] is thickness of material the electron passes through,

$\epsilon$  [MeV] is the beam energy  $E_i$  if the radiation happens before the interaction, or the final electron energy  $E_f$  if the radiation happens after the interaction,

$\zeta$  is  $\frac{1}{9}[12 + (Z + 1)/(l_1 Z + l_2)]$ , with  $l_1 \approx 5.216 - \frac{1}{3} \ln Z$  and  $l_2 \approx 7.085 - \frac{2}{3} \ln Z$ , and

$X_0$  [g/cm<sup>3</sup>] is the radiation length of the material,  $X_0 = 716.405(A/Z)/[Z(l_1 - f(Z)) + l_2]$ , and  $f(Z) = (Z\alpha)^2\{1.202 + (Z\alpha)^2[-1.0369 + 1.008(Z\alpha)^2/((Z\alpha)^2 + 1)]\}$ .

Charged particles passing through a material can lose energy due to collisions with atomic electrons. The energy transferred to the atomic electrons can lead to excitation of the atom or even ionization. This process is called Landau straggling, and it can shift the missing energy peak. Like external bremsstrahlung, the correction for Landau straggling depends on the target thickness. The correction factor for Landau straggling,  $f_{Land}$  is given by Findlay and Dusautoy [42]

$$f_{Land} = \sum_{i=1}^9 \alpha_i / \sum_{i=1}^9 \alpha_i p(x) \quad (3.77)$$

with

$$\begin{aligned} p(x) &= 1 - \frac{1}{2[1 + \sum_{i=1}^4 \delta_i x^i]^4} \\ x &= \sqrt{2}[\Delta E_m/\zeta - \Lambda - c_i]/d_i \\ d_i &= \sqrt{g_i^2 + 2 \times 10^{-5} Z^{3/4} \lambda / \zeta^2} \\ \zeta &= 0.1536(Z/A)t/\beta^2 \\ \Lambda &= \ln(\zeta\beta^2/(1 - \beta^2)) - 1.8 \ln Z - \beta^2 - 5.1004. \end{aligned}$$

$\lambda$  for an electron or for a proton is given by

$$\begin{aligned}\lambda_{electron} &= \zeta[19.26 + \ln(t/\rho)] \\ \lambda_{proton} &= 2\zeta \ln\left(\frac{\beta^2}{1-\beta^2} - 0.9 \ln Z - \beta^2 + 11.06469\right)\end{aligned}\quad (3.78)$$

where  $\rho$  is the target density in g/cm<sup>3</sup>. The parameters  $g_i$ ,  $\alpha_i$ ,  $c_i$  and  $\delta_i$  are listed in Table 3.4.

$i$	$g_i$	$\alpha_i$	$c_i$	$\delta_i$
1	0.737	0.0271	-1.48	0.196854
2	0.947	0.0798	-0.738	0.115194
3	1.23	0.1085	0.170	0.000344
4	1.68	0.1087	1.33	0.019527
5	2.40	0.0862	2.95	
6	3.68	0.0604	5.39	
7	6.18	0.0396	9.40	
8	12.3	0.0258	16.8	
9	39.7	0.0238	30.8	

Table 3.4: Landau straggling parameters.

### 3.7.2 Procedure of Radiative Correction

In principle, to unfold the radiative tail from the data perfectly using the techniques described in the previous section, knowledge of the cross section at all possible ( $\omega$ ,  $Q^2$ ,  $E_{miss}$ ,  $P_{miss}$ ) values that could cause strength to shift into the acceptance of the experiment is required. This is simply not possible. Fortunately, for response function separation, only a small region of phase space is involved, and for that region, the radiative tail comes mainly from the piece of phase space which is within the experimental acceptance.

The data for the cross section was first sorted into  $(E_{miss}, P_{miss})$  bins. The bin size

was 1 MeV in  $E_{miss}$ , and 5 MeV/c in  $P_{miss}$ . Radiative unfolding of the cross section starts with the row of  $P_{miss}$  bins for  $1p_{1/2}$  state, since no strength can be shifted into this region due to radiation from lower  $E_{miss}$  bins. The cross section for each bin in this row is corrected for radiative processes. The original contents of the bin ( $\sigma_{exp}$ ) is multiplied by the correction factors in the previous section

$$\sigma_0(E_{miss}, P_{miss}) = \sigma_{exp}(E_{miss}, P_{miss}) f(\vec{e}) f(\vec{e}') f(\vec{p}) \quad (3.79)$$

while the cutoff energy is the distance from the peak to the edge of the bin.  $f(\vec{e})$ ,  $f(\vec{e}')$ , and  $f(\vec{p})$  are the radiative correction factors for  $\vec{e}$ ,  $\vec{e}'$ , and  $\vec{p}$

$$f(\vec{e}) = \sqrt{f_{Schw}(\vec{e})} f_{ext}(\vec{e}) f_{Land}(\vec{e}) \quad (3.80)$$

$$f(\vec{e}') = \sqrt{f_{Schw}(\vec{e}')} f_{ext}(\vec{e}') f_{Land}(\vec{e}') \quad (3.81)$$

$$f(\vec{p}) = f_{Land}(\vec{p}). \quad (3.82)$$

The next step is to subtract the tails from this bin. To calculate the radiative tails, the peaking approximation was used; that is, the radiated photon is assumed to be in the direction of the charged particle. Also, the fact that there are actually three tails (one due to radiation by the incoming electron, one due to radiation by the outgoing electron, and one due to Landau straggling of the proton) needs to be taken into account. These three radiative tails can each go in different directions on the  $E_{miss}$  versus  $P_{miss}$  plot. If the radiated photon energy is  $E_\gamma$ , both the missing energy and the missing momentum are modified as follows:

$$E_{miss}^{obs} = E_{miss} + E_\gamma \quad (3.83)$$

$$\vec{P}_{miss}^{obs} = \begin{cases} \vec{P}_{miss} + E_\gamma \hat{k} & \text{if emitted by the incoming electron} \\ \vec{P}_{miss} + E_\gamma \hat{k}' & \text{if emitted by the outgoing electron} \\ \vec{P}_{miss} + E_\gamma \frac{E_p}{p} \hat{p} & \text{if emitted by the ejected proton.} \end{cases} \quad (3.84)$$

The amounts that should be subtracted from the  $i$ th bin due to the radiative tails coming from the first bin are

$$\Delta\sigma_i^{\vec{e}} = \frac{\sigma_0}{6} \left[ \frac{1}{f_i(\vec{e})} - \frac{1}{f_{i-1}(\vec{e})} \right] \left\{ 2 + \frac{1}{f_0(\vec{e}')} + \frac{1}{f_0(\vec{p})} + \frac{2}{f_0(\vec{e}')f_0(\vec{p})} \right\} \quad (3.85)$$

for the tail caused by radiation from the incoming electron,

$$\Delta\sigma_i^{\vec{e}'} = \frac{\sigma_0}{6} \left[ \frac{1}{f_i(\vec{e}')} - \frac{1}{f_{i-1}(\vec{e}')} \right] \left\{ 2 + \frac{1}{f_0(\vec{e})} + \frac{1}{f_0(\vec{p})} + \frac{2}{f_0(\vec{e})f_0(\vec{p})} \right\} \quad (3.86)$$

for the tail caused by radiation from the outgoing electron, and

$$\Delta\sigma_i^{\vec{p}} = \frac{\sigma_0}{6} \left[ \frac{1}{f_i(\vec{p})} - \frac{1}{f_{i-1}(\vec{p})} \right] \left\{ 2 + \frac{1}{f_0(\vec{e}')} + \frac{1}{f_0(\vec{e})} + \frac{2}{f_0(\vec{e}')f_0(\vec{e})} \right\} \quad (3.87)$$

for the tail caused by Landau straggling of the proton.

This process is then repeated for the subsequent  $(E_{miss}, P_{miss})$  bins in a systematic fashion. Figure 3-25 shows the  $^{16}\text{O}(e, e'p)$  cross section plots before and after radiative correction.

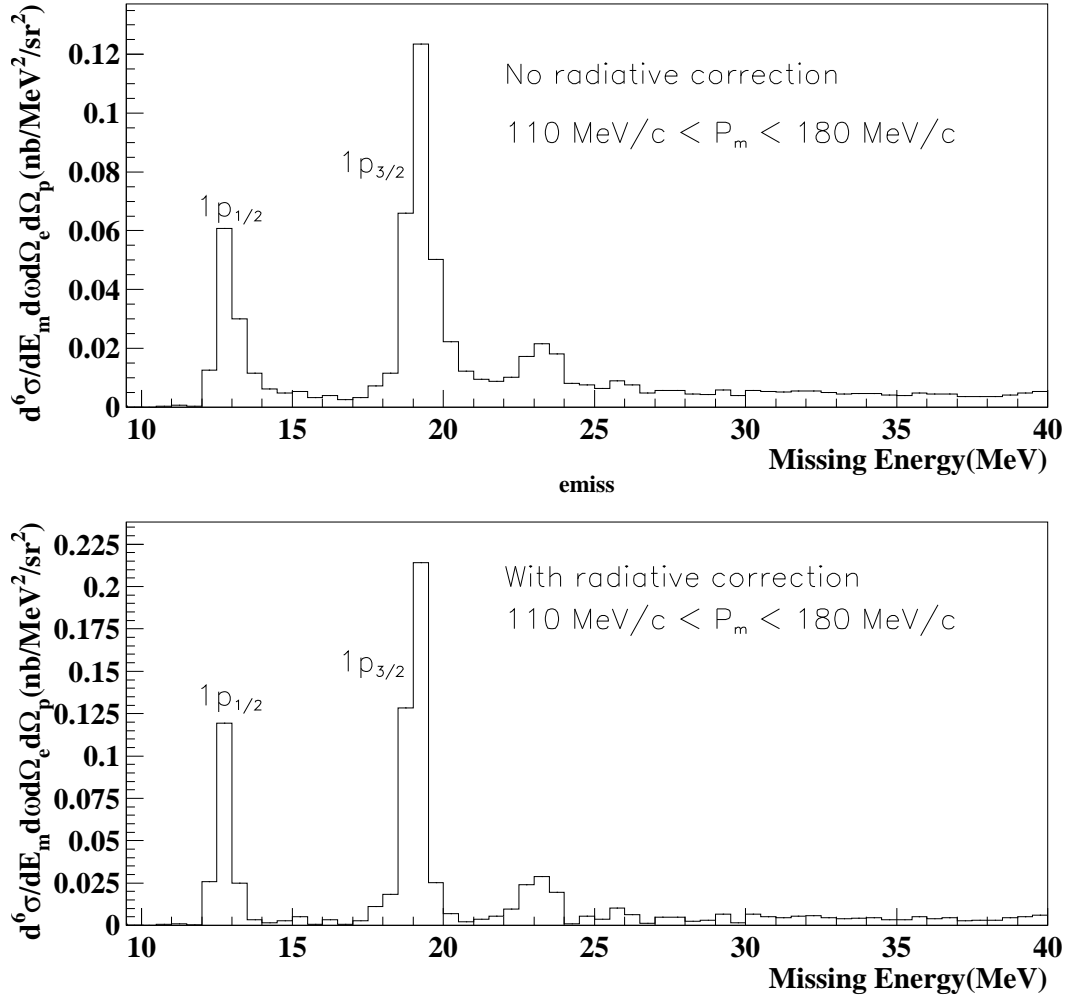


Figure 3-25:  $^{16}\text{O}(e, e'p)$  cross section before and after radiative correction. The beam energy was 843.2 MeV, and  $\theta_{pq} = +8^\circ$ .

## 3.8 Response Function Separation

### 3.8.1 $R_{LT}$ Separation

Data were taken on both sides of  $\vec{q}$  at  $E_{beam} = 2441.6$  MeV ( $\theta_{pq} = \pm 8^\circ, \pm 16^\circ, \pm 20^\circ$ ), and at  $E_{beam} = 1642.5$  MeV ( $\theta_{pq} = \pm 8^\circ$ ). This data set was used to separate the response function  $R_{LT}$ .

The cross section for a well-defined state of  $^{16}\text{O}$  can be written as

$$\frac{d^5\sigma}{d\omega d\Omega_e d\Omega_p} = R \frac{E_p p_p}{(2\pi)^3} \sigma_M [V_L R_L + V_T R_T + V_{LT} R_{LT} \cos \phi + V_{TT} R_{TT} \cos 2\phi] \quad (3.88)$$

where  $R$  is a recoil factor given by

$$R = |1 - \frac{E_p}{E_R} \frac{\vec{p}_p \cdot \vec{p}_R}{\vec{p}_p \cdot \vec{p}_p}|^{-1}. \quad (3.89)$$

For perpendicular kinematics,  $R$  is equal to unity. The kinematic factors  $V_s$  depend only on  $(\omega, Q^2)$ , while the response functions  $R_s$  depend also on  $(E_{miss}, P_{miss})$ . In principle, the response function  $R_{LT}$  can be obtained from two cross sections measured at  $\phi = 0^\circ$  and  $\phi = 180^\circ$  with  $(\omega, Q^2, E_{miss}, P_{miss})$  held constant

$$R_{LT} = \frac{1}{2KV_{LT}} \left( \frac{d^5\sigma}{d\omega d\Omega_e d\Omega_p}(\phi = 0^\circ) - \frac{d^5\sigma}{d\omega d\Omega_e d\Omega_p}(\phi = 180^\circ) \right) \quad (3.90)$$

where

$$K = \frac{E_p p_p}{(2\pi)^3} \sigma_M. \quad (3.91)$$

Since the spectrometers have finite acceptance, matching the phase space  $(\omega, Q^2, P_{miss})$  on both sides of  $\vec{q}$  for each valence state is very important.

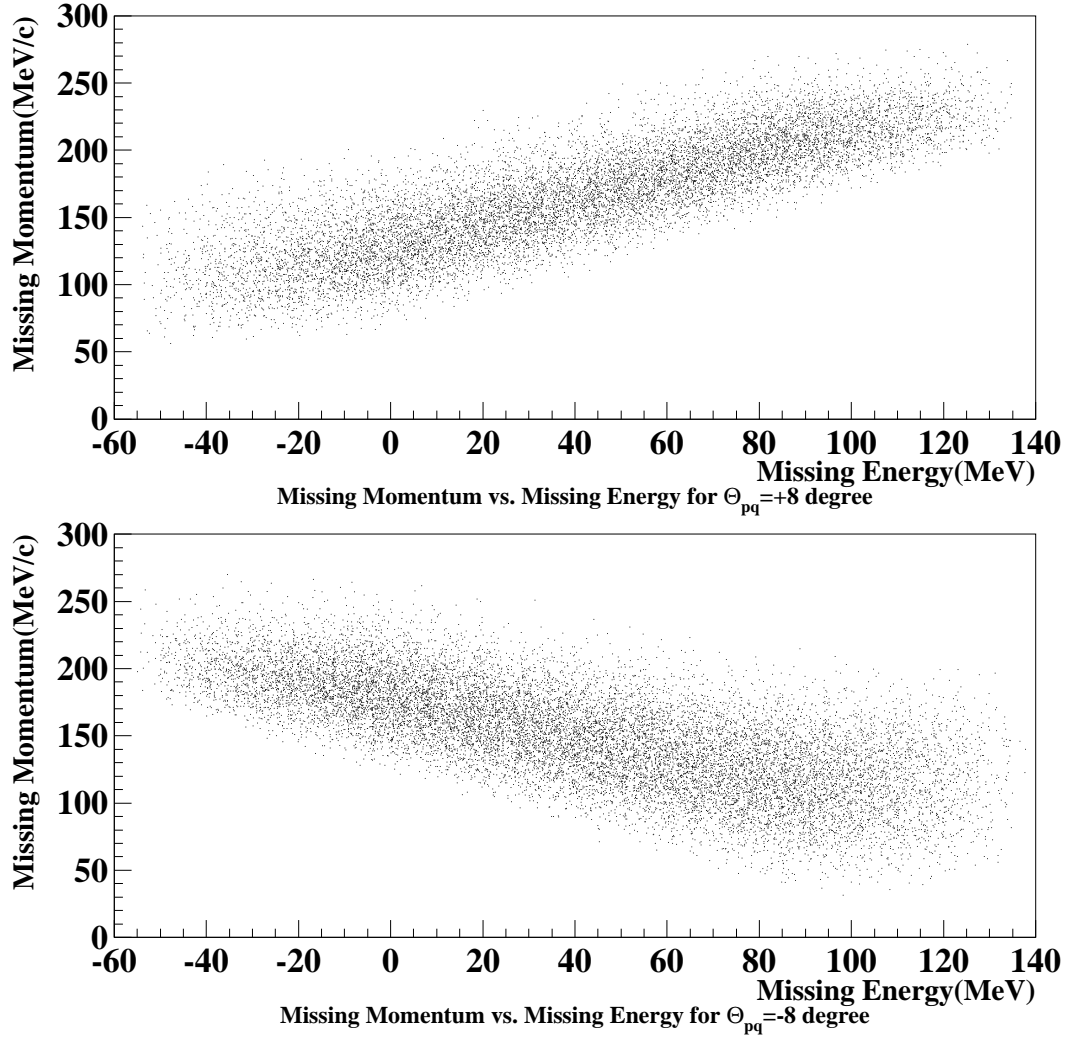


Figure 3-26: A Monte Carlo simulation of the missing momentum vs missing energy plot for  $\theta_{pq} = \pm 8^\circ$ . The density of the dots is proportional to the phase space volume. The shapes of phase space on both sides of  $\vec{q}$  is dramatically different.

In the analysis, the phase space  $(\omega, Q^2, E_{miss}, P_{miss})$  was uniformly binned on both sides of  $\vec{q}$  in the same manner. The bin size was 5 MeV/c in  $P_{miss}$ , 20 MeV in  $\omega$ ,

$0.05 \text{ (GeV/c)}^2$  in  $Q^2$ , and 1 MeV in  $E_{miss}$ . These bins were labeled  $L^j$  and  $R^j$ , where  $j = 1, 2, 3, \dots$ .  $L^j$  was the  $j^{th}$  bin at one side of  $\vec{q}$  and  $R^j$  was the  $j^{th}$  bin at the other side of  $\vec{q}$ .  $L^j$  and  $R^j$  had the same range in  $(\omega, Q^2, E_{miss}, P_{miss})$ . For each valence state, therefore  $E_{miss}$  was fixed, the radiatively-corrected cross section and the phase space volume on both sides of  $\vec{q}$  were calculated for each grid bin in  $\omega, Q^2$  and  $P_{miss}$ . Among all the bins at both side of  $\vec{q}$  ( $L^j$  and  $R^j, j = 1, 2, 3, \dots$ ), the largest phase space volume  $V^{max}$  was obtained. The  $j^{th}$  pair of bins ( $L^j$  and  $R^j$ ) were selected for the  $R_{LT}$  separation only if their phase space volumes were simultaneously larger than 50% of  $V^{max}$ . For the selected  $i^{th}$  pair of bins, the response function  $R_{LT}^i$  is calculated as the following

$$R_{LT}^i = \frac{\sigma^i(0^\circ) - \sigma^i(180^\circ)}{2K^i V_{LT}^i} \quad (3.92)$$

where

$$\delta R_{LT}^i = \frac{\sqrt{(\delta\sigma^i(0^\circ))^2 + (\delta\sigma^i(180^\circ))^2}}{2K^i V_{LT}^i}. \quad (3.93)$$

The averaged response function  $R_{LT}$  is therefore

$$R_{LT} = \frac{1}{N} \sum_{i=1}^N R_{LT}^i \quad (3.94)$$

where

$$\delta R_{LT} = \frac{1}{N} \sqrt{\sum_{i=1}^N (\delta R_{LT}^i)^2} \quad (3.95)$$

and the averaged kinematic quantities  $\bar{\omega}$ ,  $\bar{Q}^2$  and  $\bar{P}_{miss}$  are just

$$\bar{\omega} = \frac{1}{N} \sum_{i=1}^N \omega^i, \bar{Q}^2 = \frac{1}{N} \sum_{i=1}^N Q^{2i}, \bar{P}_{miss} = \frac{1}{N} \sum_{i=1}^N P_{miss}^i \quad (3.96)$$

where  $\omega^i$ ,  $P_{miss}^i$ , and  $Q^{2i}$  are the central values of the  $i^{th}$  pair of selected bins.

### 3.8.2 $R_{L+TT}$ , $R_T$ Separation

Data were taken at  $E_{beam} = 2441.6$  MeV ( $\theta_{pq} = \pm 8^\circ, \pm 16^\circ$ ), at  $E_{beam} = 1642.5$  MeV ( $\theta_{pq} = \pm 8^\circ$ ), and at  $E_{beam} = 843.2$  MeV ( $\theta_{pq} = +8^\circ, +16^\circ$ ). These data sets were used to separate  $R_{L+TT}$  and  $R_T$ .

From the sum of the cross sections measured on both sides of  $\vec{q}$  with  $\omega$ ,  $Q^2$ ,  $E_{miss}$ , and  $P_{miss}$  fixed, one can obtain

$$\begin{aligned} V_L R_L + V_T R_T + V_{TT} R_{TT} &= V_L \left( R_L + \frac{V_{TT}}{V_L} R_{TT} \right) + V_T R_T \\ &= \frac{\sigma(0^\circ) + \sigma(180^\circ)}{2K} \\ &= \Sigma_1, \end{aligned} \tag{3.97}$$

and

$$\delta \Sigma_1 = \frac{\sqrt{(\delta \sigma^i(0^\circ))^2 + (\delta \sigma^i(180^\circ))^2}}{2K} \tag{3.98}$$

From the cross section measured at the same  $(\omega, Q^2, E_{miss}, P_{miss})$ , but a different beam energy (a different electron scattering angle  $\theta_e$ ), one has

$$\begin{aligned} V_L R_L + V'_T R_T + V'_{LT} R_{LT} + V_{TT} R_{TT} &= V_L \left( R_L + \frac{V_{TT}}{V_L} R_{TT} \right) + V'_{LT} R_{LT} + V'_T R_T \\ &= \frac{\sigma'(0^\circ)}{K'} \end{aligned} \tag{3.99}$$

where  $\sigma'(0^\circ)$  is the cross section and  $K'$  is the kinematic factor at the different beam energy. Recall the expression for  $R_{LT}$  from Equation 3.90

$$\begin{aligned} V_L \left( R_L + \frac{V_{TT}}{V_L} R_{TT} \right) + V'_T R_T &= \frac{\sigma'(0^\circ)}{K'} - V'_{LT} R_{LT} \\ &= \Sigma_2 \end{aligned} \tag{3.100}$$

and

$$\delta\Sigma_2 = \sqrt{\frac{(\delta\sigma'(0))^2}{K'^2} + V'^2_{LT}(\delta R_{LT})^2}. \quad (3.101)$$

$R_L + \frac{V_{TT}}{V_L}R_{TT}$  and  $R_T$  may then be separated by combining Equations 3.97 and 3.100,

$$R_L + \frac{V_{TT}}{V_L}R_{TT} = \frac{V_T\Sigma_2 - V'_T\Sigma_1}{V_L(V_T - V'_T)} \quad (3.102)$$

$$\delta(R_L + \frac{V_{TT}}{V_L}R_{TT}) = \frac{\sqrt{V_T^2(\delta\Sigma_2)^2 + V'^2_T(\delta\Sigma_1)^2}}{V_L|V_T - V'_T|} \quad (3.103)$$

$$R_T = \frac{\Sigma_1 - \Sigma_2}{V_T - V'_T} \quad (3.104)$$

$$\delta R_T = \frac{\sqrt{(\delta\Sigma_1)^2 + (\delta\Sigma_2)^2}}{|V_T - V'_T|}. \quad (3.105)$$

In this experiment, the ranges of  $\omega$  and  $Q^2$  sampled at  $E_{beam} = 843.2$  MeV are much smaller than those at  $E_{beam} = 2441.6$  MeV. Therefore, much of the data at  $E_{beam} = 2441.6$  MeV was neglected to match the phase space for the 843.2 MeV beam energy data. Data were taken on only one side of  $\vec{q}$  ( $\phi = 0^\circ$ ) at the 843.2 MeV beam energy, and on both sides of  $\vec{q}$  ( $\phi = 0^\circ$  and  $\phi = 180^\circ$ ) for 2441.6 MeV beam energy. Only those data that overlap in  $\omega$ ,  $Q^2$  and  $P_{miss}$  were used for the response function separation. After the phase space matching was performed for the three data sets, the range for both  $\omega$  and  $Q^2$  was  $\sim\pm 3\%$ , while that for  $P_{miss}$  was  $\sim\pm 15$  MeV/c. Due to limited statistics, a single bin in  $(\omega, Q^2, P_{miss})$  was made for the matched data.

Data were also taken at  $\theta_{pq} = \pm 8^\circ$  with 1642.5 MeV beam. Therefore, in addition to Equations 3.97 and 3.100, an additional equation arises

$$\begin{aligned} V_L(R_L + \frac{V_{TT}}{V_L}R_{TT}) + V'_T R_T &= \frac{\sigma''(0^\circ) + \sigma''(180^\circ)}{2K''} \\ &= \Sigma_3 \end{aligned} \quad (3.106)$$

where  $\sigma''(0^\circ)$  and  $\sigma''(180^\circ)$  are the cross sections measured on both sides of  $\vec{q}$ , and  $K''$  is the kinematic factor at  $E_{beam} = 1642.5$  MeV. By plotting  $\Sigma/V_L$  as a function of  $V_T/V_L$  and fitting a line to the data points,  $R_L + \frac{V_{TT}}{V_L}R_{TT}$  (the intersection of the line with the  $y$ -axis) and  $R_T$  (the slope of the line) may be extracted.

### 3.8.3 $R_L, R_T$ Separation

The cross sections were measured with the HRS placed along  $\vec{q}$  at three beam energies, 843.2 MeV, 1642.5 MeV and 2441.6 MeV. Figure 3-27 shows a scatterplot of missing energy and missing momentum for a beam energy of 843.2 MeV, and the HRS along  $\vec{q}$ . Due to the huge number of events in the  $H(e, e'p)$  radiative tail, a cut on missing momentum ( $45 \text{ MeV}/c < p_{miss} < 60 \text{ MeV}/c$ ) was applied to obtain the  $^{16}\text{O}$   $1p$ -shell knockout events. Note that although the HRS was along  $\vec{q}$ , this data set was not in parallel kinematics. Because the proton momentum  $\vec{p}_p$  and  $\vec{q}$  have about the same magnitude, the missing momentum ( $45 \text{ MeV}/c < p_{miss} < 60 \text{ MeV}/c$ ) arises from the angle between them, not from the difference of the magnitudes of the vectors. As the azimuthal angle  $\phi$  varies from 0 to  $2\pi$ , the contribution from  $R_{LT}$  and  $R_{TT}$  after averaging over the acceptance is negligible, and only  $R_L$  and  $R_T$  survive. Therefore as

$$\frac{d^5\sigma}{d\omega d\Omega_e d\Omega_p} / \left( \frac{E_p p_p}{(2\pi)^3} \sigma_M V_L \right) = R_L + \frac{V_T}{V_L} R_T \quad (3.107)$$

a straight line is fit for the cross sections at the three beam energies as a function of  $V_T/V_L$ , so that  $R_L$  and  $R_T$  can be obtained.

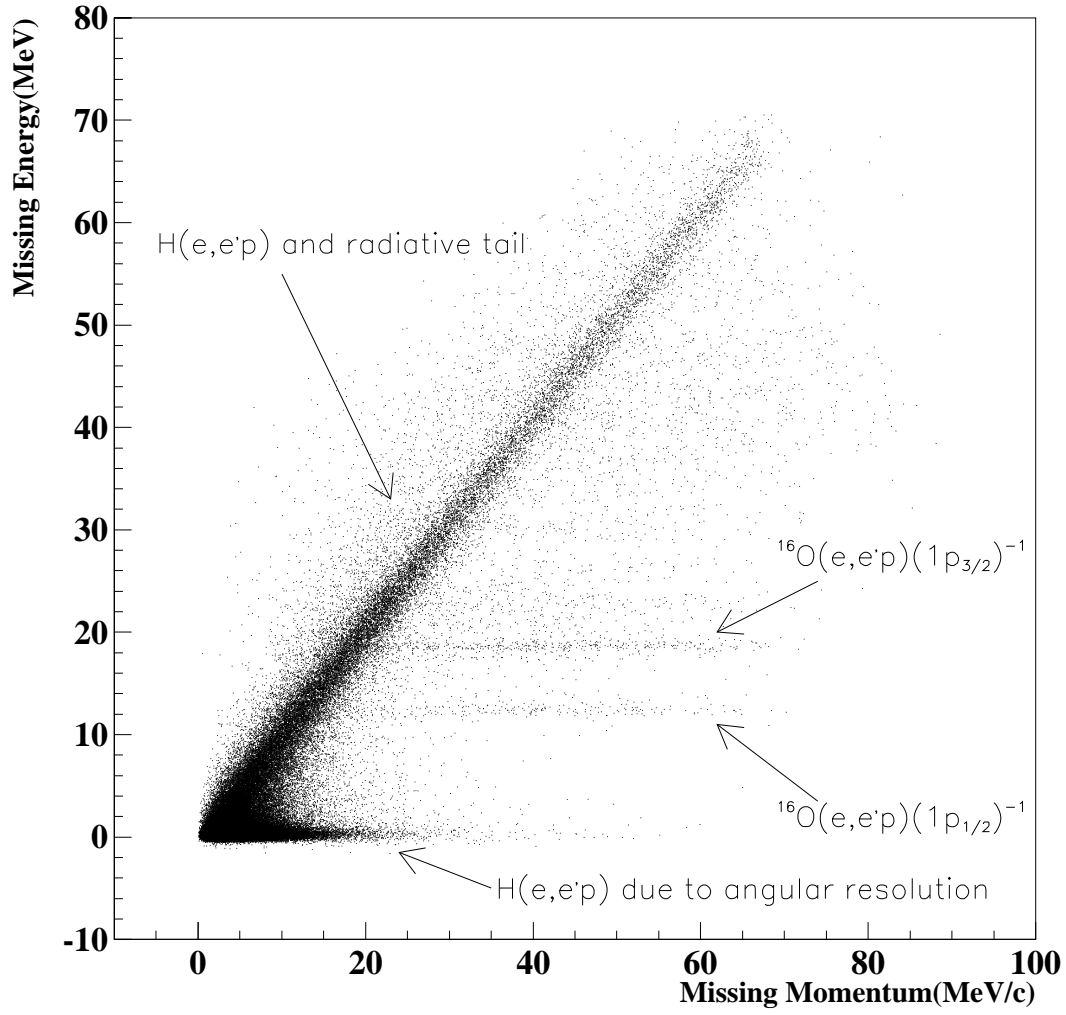


Figure 3-27: Missing energy vs. missing momentum for the HRSH along  $\vec{q}$  at  $E_{beam} = 843.2$  MeV.

The phase space ranges and the averaged kinematical variables used to calculate the cross sections are listed in Table 3.5 and Table 3.6.

Beam Energy (MeV)	$\omega$ (MeV)	$Q^2$ (GeV/c) <sup>2</sup>	$p_{miss}$ (MeV/c)
843.2	$432 < \omega < 440$	$0.79 < Q^2 < 0.83$	$45 < p_{miss} < 60$
1642.5	$410 < \omega < 433$	$0.81 < Q^2 < 0.83$	$45 < p_{miss} < 60$
2441.6	$410 < \omega < 436$	$0.80 < Q^2 < 0.83$	$45 < p_{miss} < 60$

Table 3.5: Phase space ranges used to calculate the cross sections for the HRSH along  $\vec{q}$ .

Beam Energy (MeV)	$\bar{\omega}$ (MeV)	$\bar{Q}^2$ (GeV/c) <sup>2</sup>	$\bar{p}_{miss}$ (MeV/c)
843.2	436.0	0.81	52.5
1642.5	421.5	0.82	52.5
2441.6	423.0	0.815	52.5

Table 3.6: The averaged phase space variables for the data set.

Note that the data from three beam energies have slightly different  $\bar{\omega}$  and  $\bar{Q}^2$ . This is due to the fact that the shape of the phase space at each beam energy is dramatically different. The ranges of the phase space at 1642.5 MeV and 2441.6 MeV are slightly different ( $\omega$  shifted by  $\sim 3\%$ ) so that the phase space volume is flat as a function of  $\omega$ ,  $P_{miss}$ , and  $E_{miss}$ . This makes the cross sections less sensitive to all the systematic uncertainties. Theoretically,  $\sigma/K\sigma_{Mott}$  (the measured cross section divided by the kinematic factor and Mott cross section) may vary by 3-5% if  $\omega$  is changed by 3%. This 3-5% variation in  $\sigma/K\sigma_{Mott}$  is taken as a systematic uncertainty, and is still smaller than the statistical error. Therefore, the separation of the response functions  $R_L$  and  $R_T$  is still meaningful.

Figure 3-28 shows the cross sections as a function of  $V_T/V_L$ . The response functions  $R_L$  and  $R_T$  may be obtained by fitting a line to the data points. The slope of each line is  $R_T$ , and the intersection of each line with  $y$ -axis is  $R_L$ .

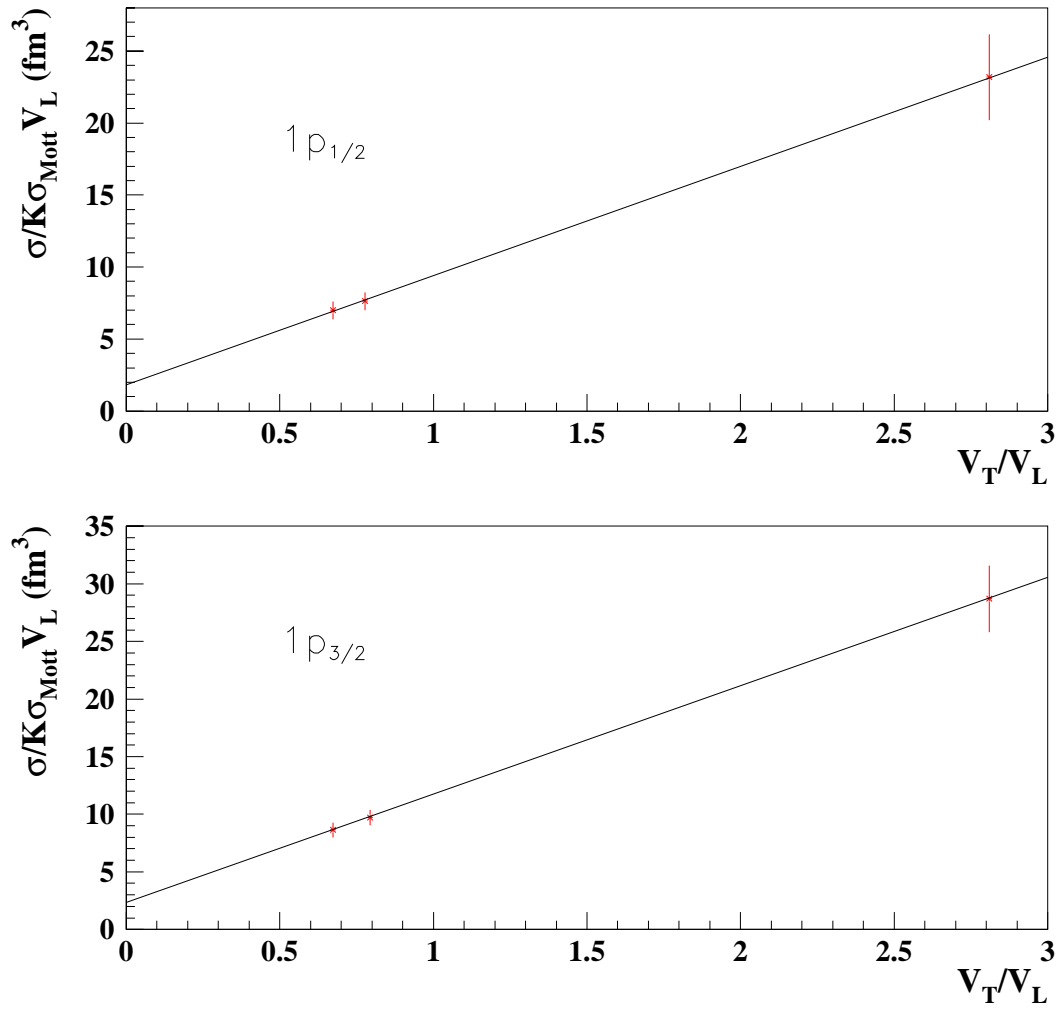


Figure 3-28: Cross sections divided by the kinematic factor and Mott cross section as a function of  $V_T/V_L$ . The slope of the lines is  $R_T$ , and the intersection of the lines with the  $y$ -axis is  $R_L$ .

## Chapter 4

# Results and Conclusion

### 4.1 Experimental Results and Systematic Uncertainties

The final cross sections are presented in Table 4.1 and Table 4.2.

Beam Energy (MeV)	$d^5\sigma/d\omega d\Omega_e d\Omega_p$ (nb/MeV·sr <sup>2</sup> )		$P_{miss}$ (MeV/c)
	$1p_{1/2}$	$1p_{3/2}$	
2441.6	$1.503 \pm 0.138$	$1.854 \pm 0.150$	52.5
1642.5	$(5.827 \pm 0.486) \times 10^{-1}$	$(7.418 \pm 0.514) \times 10^{-1}$	52.5
843.2	$(9.219 \pm 1.180) \times 10^{-2}$	$(1.143 \pm 0.115) \times 10^{-1}$	52.5

Table 4.1: Measured  $^{16}\text{O}(e, e'p)(1p)^{-1}$  cross sections for the HRSB along  $\vec{q}$ .

Table 4.1 shows the measured  $^{16}\text{O}(e, e'p)(1p)^{-1}$  cross sections with the HRSB along  $\vec{q}$  at three incident beam energies. With the cuts applied to remove the radiative tail from  $\text{H}(e, e'p)$ , the missing momentum is perpendicular to  $\vec{q}$ , and the contribution to the cross section from  $R_{LT}$  and  $R_{TT}$  average to zero. The proton kinetic energy is 427 MeV. Recall the cut conditions and the averaged  $\omega$  and  $Q^2$  for each data point are listed in Table 3.5 and Table 3.6.

	$1p_{1/2}$		$1p_{3/2}$	
Beam Energy (MeV)	$d^5\sigma/d\omega d\Omega_e d\Omega_p$ (nb/MeV·sr <sup>2</sup> )	$P_{miss}$ (MeV/c)	$d^5\sigma/d\omega d\Omega_e d\Omega_p$ (nb/MeV·sr <sup>2</sup> )	$P_{miss}$ (MeV/c)
2441.6	$(5.654 \pm 0.452) \times 10^{-3}$	-330.0	$(2.143 \pm 0.081) \times 10^{-2}$	-330.0
	$(3.028 \pm 0.287) \times 10^{-2}$	-279.0	$(1.672 \pm 0.051) \times 10^{-1}$	-276.0
	$1.461 \pm 0.026$	-149.0	$2.995 \pm 0.038$	-149.0
	$1.538 \pm 0.051$	-60.0	$2.621 \pm 0.065$	-60.0
	$1.598 \pm 0.046$	60.0	$2.236 \pm 0.054$	60.0
	$0.906 \pm 0.027$	149.0	$1.574 \pm 0.037$	149.0
	$(1.433 \pm 0.286) \times 10^{-2}$	279.0	$(2.878 \pm 0.509) \times 10^{-2}$	276.0
	$(2.315 \pm 1.088) \times 10^{-3}$	355.0	$(5.418 \pm 1.116) \times 10^{-3}$	355.0
1642.5	$0.525 \pm 0.031$	-148.0	$1.039 \pm 0.036$	-146.0
	$0.295 \pm 0.032$	148.0	$0.516 \pm 0.037$	146.0
843.2	$(7.894 \pm 0.570) \times 10^{-2}$	-150.0	$(1.467 \pm 0.076) \times 10^{-1}$	-150.0
	$(1.161 \pm 0.340) \times 10^{-3}$	-275.0	$(5.847 \pm 0.640) \times 10^{-3}$	-275.0

Table 4.2: Measured  $^{16}\text{O}(e, e'p)(1p)^{-1}$  cross sections in perpendicular kinematics.

The measured  $^{16}\text{O}(e, e'p)(1p)^{-1}$  cross sections in perpendicular kinematics are listed in Table 4.2. The average  $\omega$  is 436 MeV, the average  $Q^2$  is 0.8 (GeV/c)<sup>2</sup> and the kinetic energy of proton  $T_p$  is 427 MeV. A positive missing momentum means the azimuthal angle  $\phi = 0^\circ$  ( $\theta_p < \theta_q$ ).

The final response functions are listed in Table 4.3, Table 4.4, and Table 4.5.

	$1p_{1/2}$		$1p_{3/2}$	
$R_L + \frac{V_{TT}}{V_L} R_{TT}$ (fm <sup>3</sup> )	$0.56 \pm 0.49$	$(0.86 \pm 3.0) \times 10^{-2}$	$2.2 \pm 0.75$	$0.20 \pm 0.055$
$R_T$ (fm <sup>3</sup> )	$6.075 \pm 0.61$	$0.122 \pm 0.04$	$10.35 \pm 1.04$	$0.291 \pm 0.077$
$P_{miss}$ (MeV/c)	149.0	279.0	148.0	276.0

Table 4.3: Response functions  $R_L + \frac{V_{TT}}{V_L} R_{TT}$  and  $R_T$  for the  $1p$  states of  $^{16}\text{O}$ .

Table 4.3 lists the separated response functions  $R_L + \frac{V_{TT}}{V_L} R_{TT}$  and  $R_T$  for the  $1p$  states of  $^{16}\text{O}$ . The average  $\omega$  is 436 MeV, the average  $Q^2$  is 0.8 (GeV/c)<sup>2</sup>, and the

proton kinetic energy is 427 MeV.

	$1p_{1/2}$		$1p_{3/2}$	
Beam Energy (MeV)	$R_{LT}$ (fm <sup>3</sup> )	$P_{miss}$ (MeV/c)	$R_{LT}$ (fm <sup>3</sup> )	$P_{miss}$ (MeV/c)
2441.6	$0.117 \pm 0.134$	60.0	$-0.754 \pm 0.165$	60.0
	$-0.999 \pm 0.066$	149.0	$-2.56 \pm 0.096$	148.0
	$-0.0289 \pm 0.0073$	279.0	$-0.25 \pm 0.013$	276.0
	$(-1.847 \pm 2.999) \times 10^{-3}$	345.0	$(-1.50 \pm 0.3) \times 10^{-2}$	345.0
1642.5	$-1.198 \pm 0.235$	148.0	$-2.82 \pm 0.292$	147.0

Table 4.4: Response function  $R_{LT}$  for the  $1p$  states of  $^{16}\text{O}$ .

Table 4.4 lists the separated response function  $R_{LT}$  for the  $1p$  states of  $^{16}\text{O}$ . The average  $\omega$  is 436 MeV, the average  $Q^2$  is  $0.8 \text{ (GeV/c)}^2$ , and the proton kinetic energy is 427 MeV. The response function  $R_{LT}$  for the  $1p$  states has been measured twice using two different beam energies 2441.6 MeV and 1642.5 MeV at a missing momentum  $\sim 150 \text{ MeV/c}$ . The results from the two measurements agree within one standard deviation. This indicates the systematic error for this experiment is very small.

	$1p_{1/2}$	$1p_{3/2}$
$R_L \text{ (fm}^3\text{)}$	$1.82 \pm 1.17$	$2.35 \pm 1.18$
$R_T \text{ (fm}^3\text{)}$	$7.58 \pm 1.42$	$9.40 \pm 1.39$
$P_{miss}$	52.5	52.5

Table 4.5: Response functions  $R_L$  and  $R_T$  for the  $1p$  states of  $^{16}\text{O}$ .

Table 4.5 lists the separated response functions  $R_L$  and  $R_T$  for the data taken with the HRS along  $\vec{q}$ . The average  $P_{miss}$  is 52.5 MeV/c. Recall the average  $\omega$  and  $Q^2$  are listed in Table 3.6.

The measured left-right asymmetry ( $A_{LT}$ ) is listed in Table 4.6.

	$1p_{1/2}$		$1p_{3/2}$	
Beam Energy (MeV)	$A_{LT}$	$P_{miss}$ (MeV/c)	$A_{LT}$	$P_{miss}$ (MeV/c)
2441.6	$0.019 \pm 0.017$	60.0	$-0.079 \pm 0.017$	60.0
	$-0.232 \pm 0.016$	149.0	$-0.306 \pm 0.013$	148.0
	$-0.359 \pm 0.084$	279.0	$-0.689 \pm 0.039$	276.0
	$-0.135 \pm 0.215$	345.0	$-0.394 \pm 0.084$	345.0
1642.5	$-0.250 \pm 0.018$	148.0	$-0.306 \pm 0.035$	147.0

Table 4.6:  $A_{LT}$  for the  $1p$  states of  $^{16}\text{O}$ .

$A_{LT}$  is defined as

$$A_{LT} = \frac{\sigma(\phi = 0^\circ) - \sigma(\phi = 180^\circ)}{\sigma(\phi = 0^\circ) + \sigma(\phi = 180^\circ)}, \quad (4.1)$$

where  $\phi = 0^\circ$  means  $\theta_q > \theta_p$ . The average  $\omega$  is 436 MeV, the average  $Q^2$  is 0.8 (GeV/c)<sup>2</sup>, and the proton kinetic energy is 427 MeV. At missing momentum  $\sim 150$  MeV/c, the agreement between the two  $A_{LT}$  measurements at beam energies of 2441.6 MeV and 1642.5 MeV indicates that the systematic error for this experiment is very small.

A quantitative estimate of the systematic errors in this experiment is listed in Table 4.7.

Quantity	Uncertainty	% effect on cross section
Beam energy	0.2 %	0.4
Electron scattering angle	0.3 mr	0.3
Proton scattering angle	0.3 mr	0.4
Proton solid angle	2.0 %	2.0
Luminosity (relative)	1.7 %	1.7
Luminosity (absolute)	4.0 %	4.0
Total uncertainty		4.8

Table 4.7: A summary of the systematic errors in E89-003.

The total systematic error for the  $^{16}\text{O}(e, e'p)$  cross section is a little less than 5%. It is dominated by the uncertainty of  $H(e, e')$  cross section, which has been used to obtain the absolute luminosity. The uncertainty from different quantities in Table 4.7 contributes differently to the error of the response functions. Since the uncertainty in absolute luminosity applies to each cross section measurement equally, its contribution to the error in the separated response functions is just itself, 4.0%. For the remaining quantities in Table 4.7, the uncertainties randomly influence each cross section measurement; therefore, they contribute to the error of response functions in the same manner as the statistical uncertainty.

## 4.2 Comparison with Theories

At present, two DWIA calculations are available for the kinematics of this experiment. One was performed by Kelly [33] with a non-relativistic approach, and the other was performed by Van Orden [43] in a fully-relativistic approach.

### 4.2.1 NRDWIA from Kelly

The calculation by Kelly used the program LEA [33]. The details of this calculation are described in [6][17]. Some main features are presented here:

- Coulomb Distortion. The effect of Coulomb distortion is included in LEA in the Effective Momentum Approximation

$$\vec{q}_{eff} = \vec{q} + \frac{3\alpha Z}{2R_Z E_i} (\vec{q} - \omega \frac{\vec{k}_f}{|\vec{k}_f|}) \quad (4.2)$$

where  $R_Z$  is the RMS radius and  $E_i$  is the incident beam energy.

- Bound State Wavefunction. LEA calculates the proton bound state wave function by solving the Schrödinger equation

$$[-\frac{\hbar^2}{2M_p} \nabla^2 + V^Z(r) + V^C(r) + V^{LS}(r) \vec{L} \cdot \vec{\sigma}] \phi_b = E_b \phi_b \quad (4.3)$$

where

$$V^Z(r) = \frac{\alpha(Z-1)}{2R_Z^3} (3R_Z^2 - r^2) \quad (4.4)$$

$$V^C(r) = -V_0 f(r) \quad (4.5)$$

$$V^{LS}(r) = -V_0^{LS} \frac{2}{r} \frac{df(r)}{dr} \quad (4.6)$$

with

$$f(r) = \frac{1}{1 + e^{\frac{r-R}{a}}}. \quad (4.7)$$

To correct for the nonlocality effect, the radial wave function has been multiplied by the Perey factor [44]

$$P(r) = [1 + \frac{\mu}{2\hbar^2} \beta^2 V_0 f(r)]^{-1/2} \quad (4.8)$$

where  $\mu$  is the reduced mass (see Equation 1.28), and the nonlocality parameter  $\beta$  is chosen to be 0.85 fm.

- Ejectile Distortion. The final state interaction between the proton and the resid-

ual nucleus has been described by the global Dirac optical potential EDAD1[20], which is obtained by fitting proton elastic scattering data in the energy range 20-1040 MeV for  $^{12}\text{C}$ ,  $^{16}\text{O}$ ,  $^{40}\text{Ca}$ ,  $^{90}\text{Zr}$ , and  $^{208}\text{Pb}$ . The proton kinetic energy for this experiment is about 433 MeV, which is right within the energy range this potential was determined. The Dirac spinor  $\Psi(\vec{r})$  satisfies the Dirac equation

$$[\vec{\alpha} \cdot \vec{p}_p + \beta(m_p + S)]\Psi = (E - V - V^Z)\Psi \quad (4.9)$$

where  $S$  is the scalar potential,  $V$  is the vector potential, and  $V^Z$  is the coulomb potential. Both  $S$  and  $V$  have the form

$$U = U_1^R f(x) + iU_1^I f(x) + U_2^R \frac{df(x)}{dx} + iU_2^I \frac{df(x)}{dx} \quad (4.10)$$

with

$$f(x) = [(1 + e^x)(1 + e^{-x})]^{-1} \quad (4.11)$$

$$x = (r - R)/a. \quad (4.12)$$

Each of the four components of the scalar and vector potentials can be expanded into polynomials in terms of  $A$  and  $E$ . By eliminating the lower component  $\psi_-(\vec{r})$  of the spinor  $\Psi(\vec{r})$ , the Dirac equation becomes an equivalent Schrödinger equation

$$[\nabla^2 + k^2 - 2\mu(U^Z + U^C + U^{LS} \vec{L} \cdot \vec{\sigma})]\phi = 0 \quad (4.13)$$

where the upper component  $\psi_+(\vec{r})$  of spinor  $\Psi(\vec{r})$  is related to  $\phi$  by the Darwin

transformation

$$\psi_+(\vec{r}) = B^{1/2}\phi \quad (4.14)$$

$$B = 1 + \frac{S - V - V^Z}{E + m_p} \quad (4.15)$$

and the equivalent Schrödinger potentials are then

$$U^Z = \frac{E}{\mu}V^Z \quad (4.16)$$

$$U^C = \frac{E}{\mu}\left[V + \frac{m_p}{E} + \frac{S^2 - V^2}{2E} - \frac{V^Z(V^Z + 2V)}{2E}\right] + U^D \quad (4.17)$$

$$U^D = \frac{1}{2\mu}\left[-\frac{1}{2r^2B}\frac{d}{dr}(r^2B') + \frac{3}{4}\left(\frac{B'}{B}\right)^2\right] \quad (4.18)$$

$$U^{LS} = -\frac{1}{2\mu}\frac{B'}{rB}. \quad (4.19)$$

- Current Operator. The current operator for a free nucleon is

$$\Gamma_1^\mu = \gamma^\mu G_M(Q^2) - \frac{P^\mu}{2M}F_2(Q^2) \quad (4.20)$$

where  $P^\mu = P_i^\mu + P_f^\mu$  is the sum of the proton initial and final 4-momentum, and  $G_M(Q^2)$  and  $F_2(Q^2)$  are the form factors. In this calculation, the off-shell extrapolation is obtained by replacing the energy transfer and momenta by

$$(\omega, \vec{q}) \rightarrow (\bar{\omega}, \vec{q}) \quad (4.21)$$

$$P^\mu \rightarrow \bar{P}^\mu = (\bar{E} + E_f, \vec{p}_i + \vec{p}_f) \quad (4.22)$$

in the nucleon current operator. Here  $\bar{E}$  and  $\bar{\omega}$  are defined as

$$\bar{E} = \sqrt{M^2 + P_{miss}^2} \quad (4.23)$$

$$\bar{\omega} = \sqrt{M^2 + p_f^2} - \bar{E}. \quad (4.24)$$

However, the form factors are still evaluated at the asymptotic momentum transfer  $Q^2 = \vec{q}^2 - \omega^2$ . Therefore, the current operator becomes

$$\bar{\Gamma}_1^\mu = \gamma^\mu G_M(Q^2) - \frac{\bar{P}^\mu}{2M} F_2(Q^2). \quad (4.25)$$

This NRDWIA calculation has been compared  $^{16}\text{O}(e, e'p)(1p)^{-1}$  cross section measurement by Leuschner *et al.* [11] The parameters for the bound state wave functions obtained from this comparison are shown in Table 4.8.

	$1p_{1/2}$	$1p_{3/2}$
Binding Energy $E_b$	12.127 MeV	18.447 MeV
RMS Radius $R_Z$	3.024 fm	3.024 fm
Central Well Depth $V_0$	51.582 MeV	61.164 MeV
Spin-Orbit Well Depth $V_0^{LS}$	6.50 MeV	6.50 MeV
Radius $R$	1.36 fm	1.25 fm
Diffuseness $a$	0.65 fm	0.65 fm
Spectroscopic factors	0.75	0.64

Table 4.8: Parameters used for calculating the bound states.

This calculation was also performed for the kinematics of the data taken by Blomqvist *et al.* [15] The calculation overestimates the distorted momentum distribution for  $^{16}\text{O}(e, e'p)(1p)^{-1}$  by almost a factor of 2.0 (see Figure 1-12).

#### 4.2.2 RDWIA from Van Orden

The calculation of Van Orden is described in detail in [45][46]. It employs a relativistic quantum field theory for the bound state and a relativistic optical potential formalism to describe the final state interaction. The bound state wave functions are calculated using relativistic Hartree equations derived from full quantum field theory [47]. In this theory, the nucleons interact through the exchange of  $\sigma$ ,  $\omega$ ,  $\pi$ ,  $\rho$  and  $\gamma$ ; therefore, there

is no need to introduce static potentials. The model parameters are determined from the bulk properties of nuclear matter. This method is claimed to give good agreement with the existing data on charge density distributions, neutron densities, RMS radii of the ground states of spherical nuclei, and the observed spin-orbit splitting between single particle levels [48]. This agreement may be attributed to the fact that the non-local, non-central, and density-dependent effects arise when the relativistic potentials are reduced to non-relativistic form. The final state interaction is described in a relativistic manner as discussed in [49].

The spectroscopic factors folded into the Van Orden calculations to compare with the data are 0.61 for both  $1p_{1/2}$  and  $1p_{3/2}$  states.

#### 4.2.3 Comparison with the Calculations

The data from this experiment have been compared with calculations from Kelly and Van Orden. In Kelly's calculation, the spectroscopic factors are 0.75 for  $1p_{1/2}$  and 0.65 for  $1p_{3/2}$ , while in Van Orden's calculation, the spectroscopic factors for both  $1p_{1/2}$  and  $1p_{3/2}$  are 0.61 .

The standard DWIA calculation with a one-body current operator does not conserve current. This violation is due to the many-body currents associated with the interactions which establish the mean field and the binding energy. There are several ways to restore the current. Each prescription is associated with a gauge. The prescription

$$J_q \rightarrow \frac{\omega}{q} J_0 \quad (4.26)$$

in which the longitudinal current is replaced by the charge operator is associated with the Coulomb gauge. Similarly, the prescription

$$J_0 \rightarrow \frac{q}{\omega} J_q \quad (4.27)$$

is associated with the Weyl gauge. Finally, the prescription associated with the Landau gauge is

$$J_\mu \rightarrow J_\mu + \frac{J \cdot q}{Q^2} q_\mu. \quad (4.28)$$

In principle, the three gauges are equivalent. They should give the same results if the current is conserved. Therefore, a comparison of the calculations based on different gauges should provide a rough test of the uncertainty introduced into the calculations by the violation of current conservation.

The RDWIA calculations of Van Orden using the Coulomb gauge and the Weyl gauge have been applied to the quasielastic  $^{16}\text{O}(e, e'p)(1p)^{-1}$  reaction at a proton kinetic energy 135 MeV [45]. A quantity  $C_{test}$  was defined as

$$C_{test} = \frac{R_L - \tilde{R}_L}{R_L + \tilde{R}_L} \quad (4.29)$$

where  $R_L$  is obtained using Coulomb gauge, and  $\tilde{R}_L$  is obtained using Weyl gauge. The calculations show that the quantity  $C_{test}$  is about 10% when  $R_L$  is at its maximum.

A similar test was performed for the NRDWIA calculations of Kelly using the Coulomb gauge and the Weyl gauge for the quasielastic  $^{16}\text{O}(e, e'p)(1p)^{-1}$  reaction.  $\omega$  is 150 MeV,  $q$  is 525 MeV/c, and the proton kinetic energy is about 135 MeV. The quantities  $C_L$  and  $C_{LT}$  are defined as

$$C_L = \frac{R_L - \tilde{R}_L}{R_L + \tilde{R}_L} \quad (4.30)$$

$$C_{LT} = \frac{R_{LT} - \tilde{R}_{LT}}{R_{LT} + \tilde{R}_{LT}} \quad (4.31)$$

where  $R_L$  and  $R_{LT}$  are obtained using the Coulomb gauge, while  $\tilde{R}_L$  and  $\tilde{R}_{LT}$  are obtained using Weyl gauge. The results are shown in Figure 4-1 and Figure 4-2.

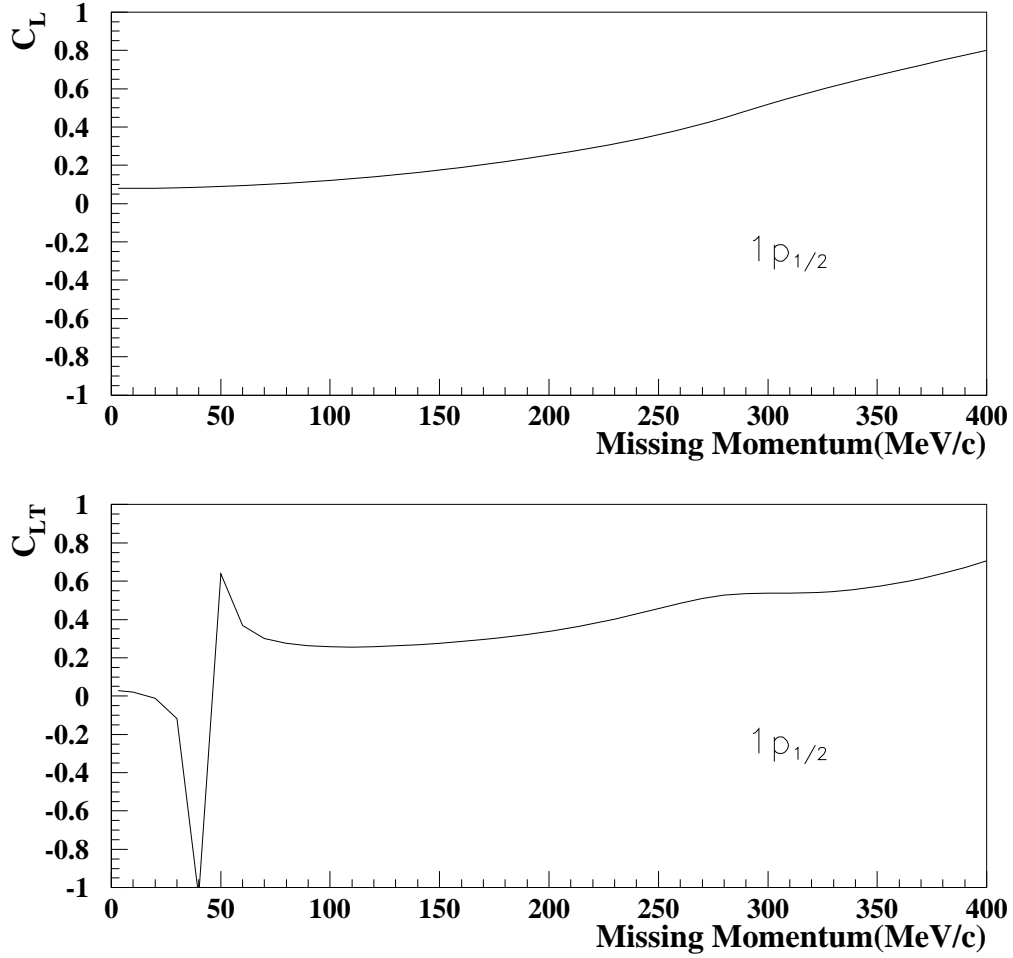


Figure 4-1: Comparison of the NRDWIA calculations of Kelly using the Coulomb gauge and the Weyl gauge for the  $1p_{1/2}$  state.  $\omega$  is 150 MeV,  $q$  is 525 MeV/c, and the proton kinetic energy is about 135 MeV.

The difference between Kelly's NRDWIA calculations using the Coulomb gauge and the Weyl gauge for the  $1p_{1/2}$  state is about 20% at the maxima of the response functions  $R_L$  and  $R_{LT}$ . At low missing momentum, this difference is small for  $R_L$ ,

but large for  $R_{LT}$ . At high missing momentum, this difference increases as a function of missing momentum, and can be as high as 60% when the missing momentum is around 400 MeV/c.

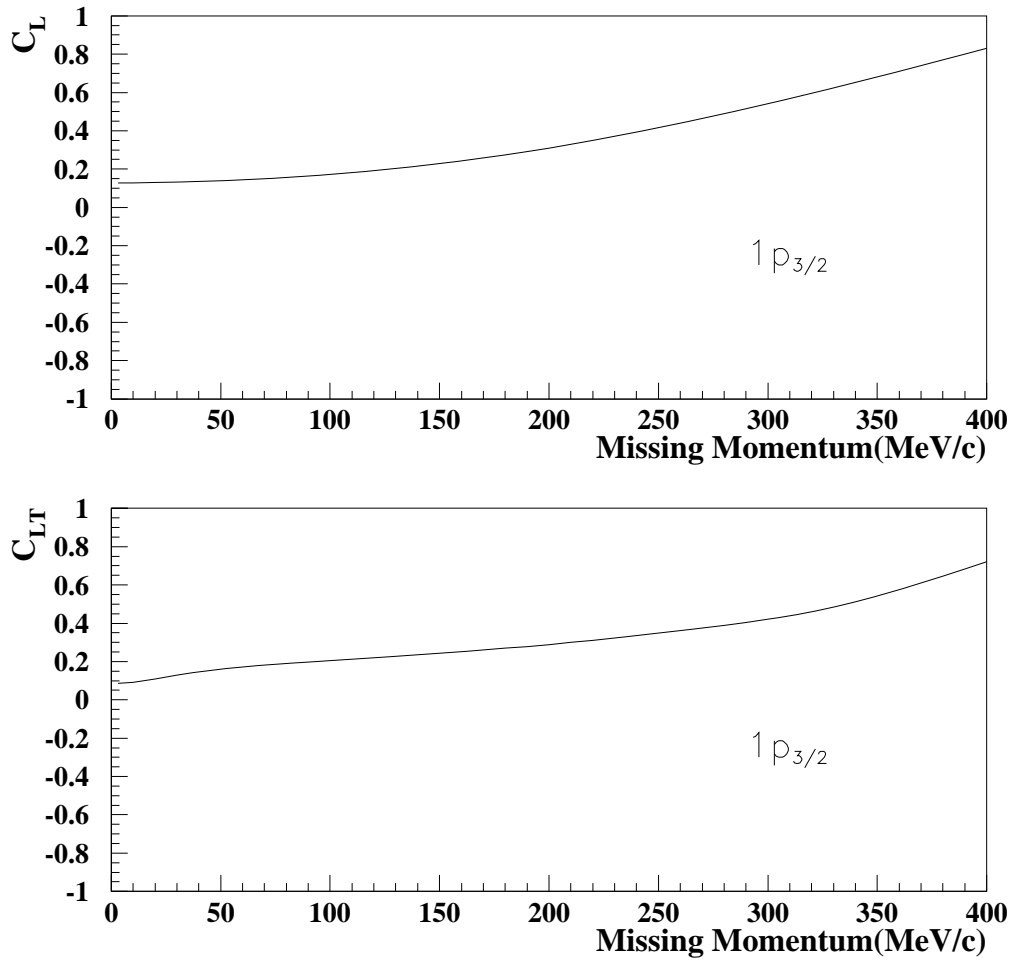


Figure 4-2: Comparison of the NRDWIA calculations of Kelly using the Coulomb gauge and the Weyl gauge for the  $1p_{3/2}$  state.  $\omega$  is 150 MeV,  $q$  is 525 MeV/c, and the proton kinetic energy is about 135 MeV.

The difference between Kelly's NRDWIA calculations using the Coulomb gauge and the Weyl gauge for the  $1p_{3/2}$  state is about 20% at the maxima of the response functions  $R_L$  and  $R_{LT}$ . This difference increases as a function of missing momentum and can reach 70% when the missing momentum is around 400 MeV/c.

The test shows that RDWIA calculations conserve current better than the NRDWIA calculation. This may be due to the fact that part of the meson exchange currents is introduced when the RDWIA calculation is reduced to a non-relativistic form.

The left-right asymmetry ( $A_{LT}$ ) measured in the experiment is compared with the NRDWIA calculations from Kelly using the Coulomb, Weyl and Landau gauges. The comparison is shown in Figure 4-3.

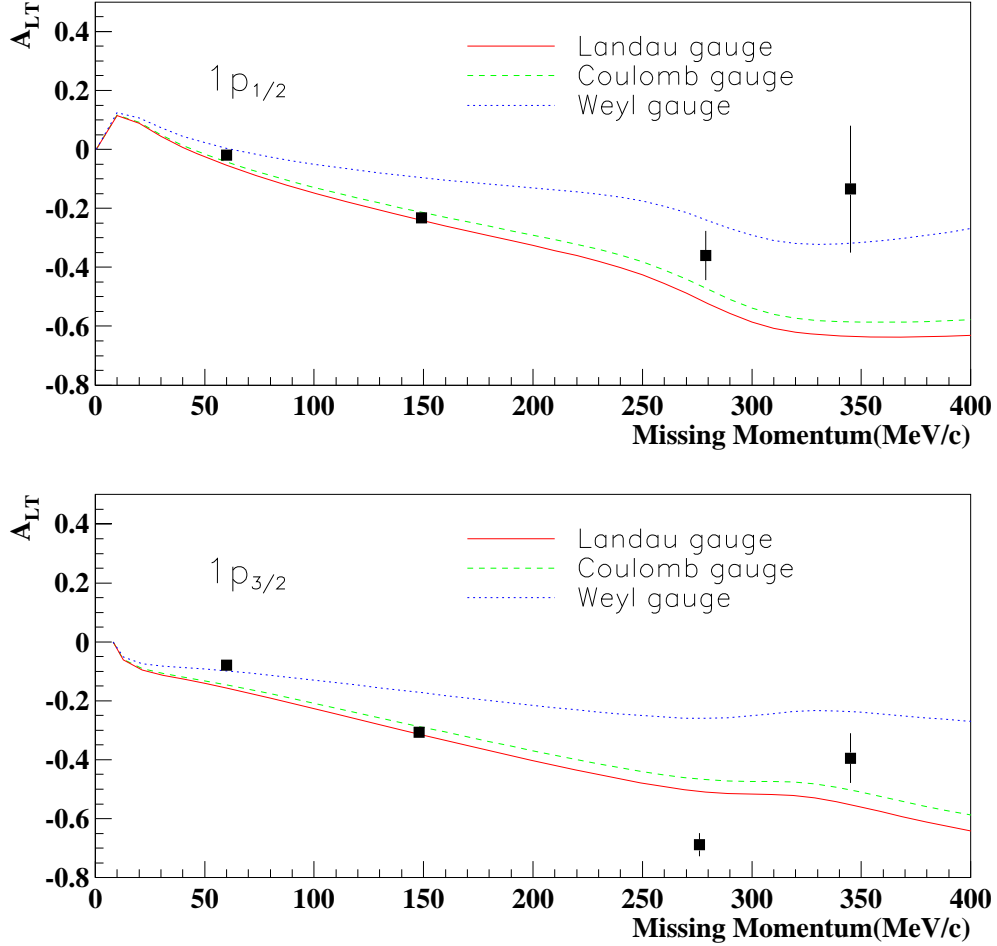


Figure 4-3: Comparison of the left-right asymmetry with the non-relativistic DWIA calculations of Kelly using the Landau gauge, the Coulomb gauge, and the Weyl gauge.

The NRDWIA calculations using the Coulomb gauge and the Landau gauge give similar results for  $A_{LT}$ . The data is not precise enough to separate these two calculations. However, the Weyl gauge produces very different results. The data do not support the calculations using the Weyl gauge.

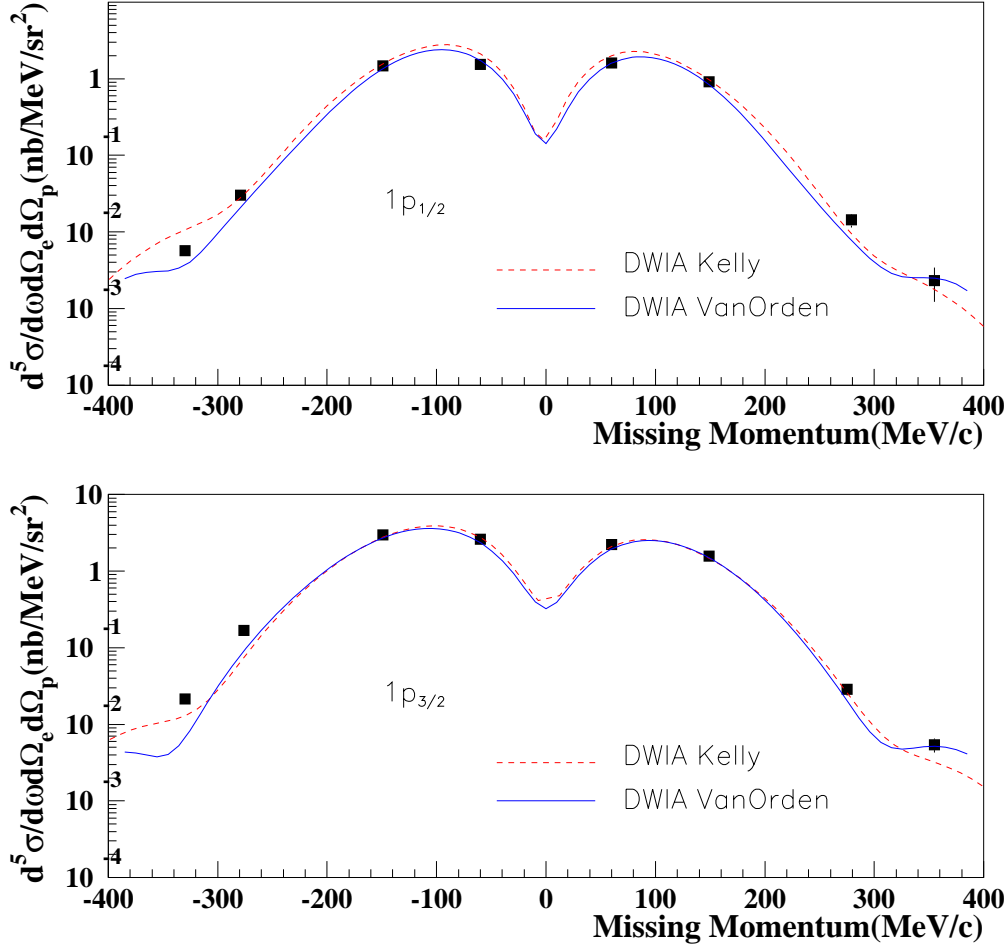


Figure 4-4: Comparison of the cross sections with the DWIA calculations. The beam energy is 2441.6 MeV, the average  $\omega$  is 436 MeV, the average  $Q^2$  is 0.8 (GeV/c)<sup>2</sup>, and the proton kinetic energy is 427 MeV. The calculations used the Coulomb gauge.

Figure 4-4 shows the comparison of the measured cross section with the DWIA calculations. The data is in good agreement with both DWIA calculations for missing momentum less than 280 MeV/c. The consistency between the data and the

DWIA calculation from Kelly indicates that this data set agrees with the data from Leuschner *et al.*[11], but disagrees with the data from Blomqvist *et al.*[15] At missing momentum larger than 280 MeV/c, neither of the DWIA calculations agrees with the data consistently.

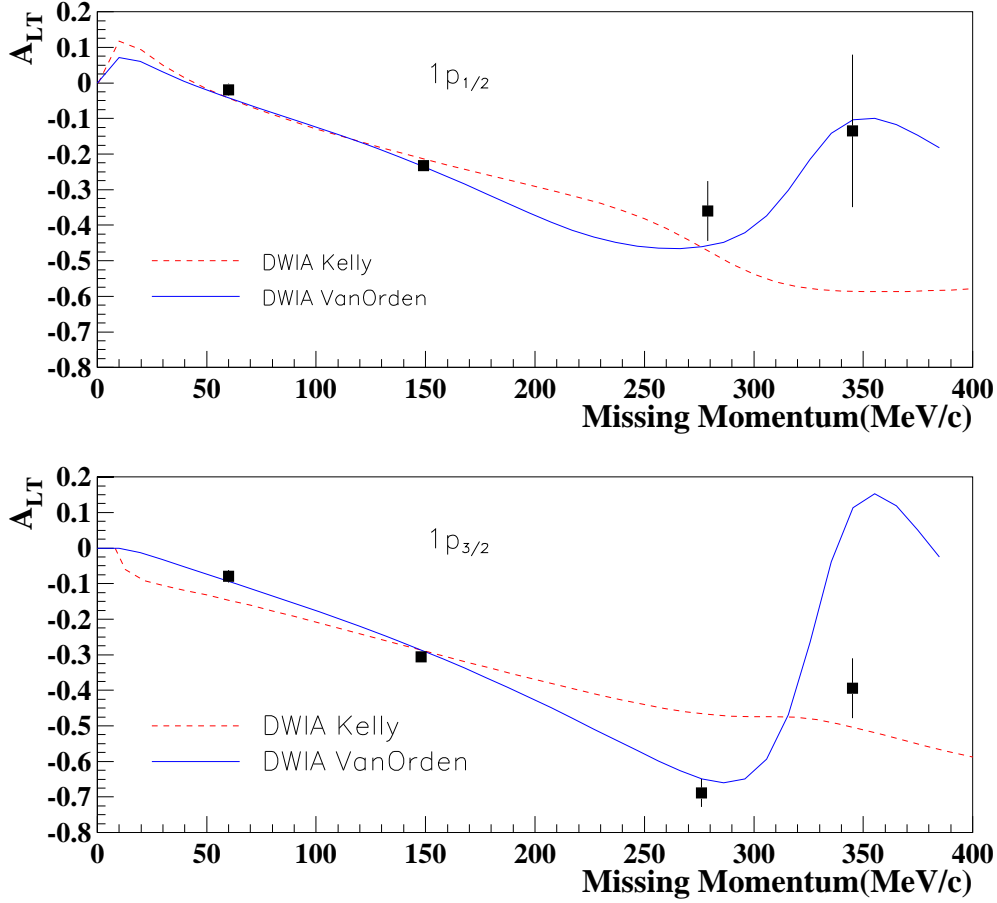


Figure 4-5: Comparison of the left-right asymmetry with the DWIA calculations. The beam energy is 2441.6 MeV, the averaged  $\omega$  is 436 MeV, the averaged  $Q^2$  is  $0.8 \text{ (GeV/c)}^2$  and the proton kinetic energy is 427 MeV. The calculations used Coulomb gauge.

Figure 4-5 shows a comparison of the left-right asymmetry with the DWIA calculations from Kelly and Van Orden. The data is in good agreement with the RDWIA calculation from Van Orden except for the  $1p_{3/2}$  state at a missing momentum of 345

MeV/c. The two calculations differ tremendously at large missing momentum. The data favors the RDWIA calculation of Van Orden.

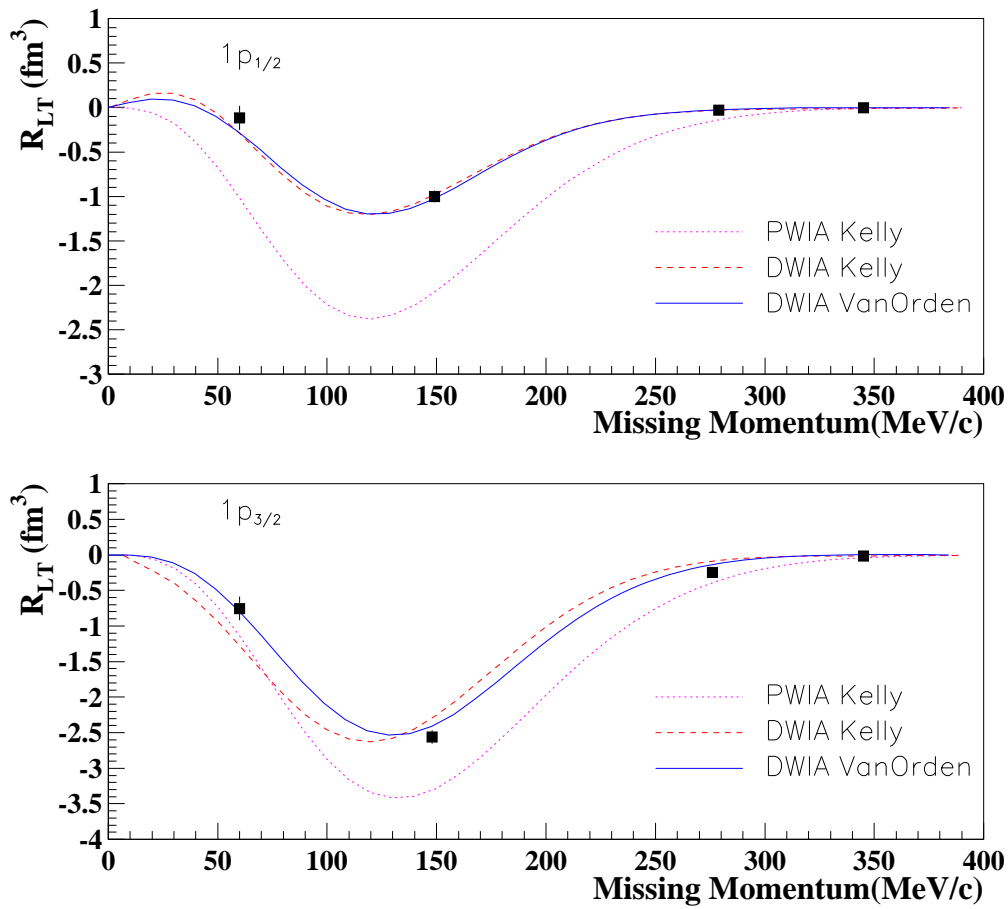


Figure 4-6: Comparison of  $R_{LT}$  with the calculations. The beam energy is 2441.6 MeV, the average  $\omega$  is 436 MeV, the average  $Q^2$  is 0.8 (GeV/c)<sup>2</sup>, and the proton kinetic energy is 427 MeV. The calculations used Coulomb gauge.

Figure 4-6 shows a comparison of the response function  $R_{LT}$  with the calculations.

For the low missing momentum data points ( $\sim 60$  MeV/c and  $\sim 149$  MeV/c), the data agrees very well with both DWIA calculations, except at a missing momentum of  $\sim 60$  MeV/c, where the NRDWIA calculation from Kelly overstates the  $R_{LT}$  for the  $1p_{3/2}$  state.

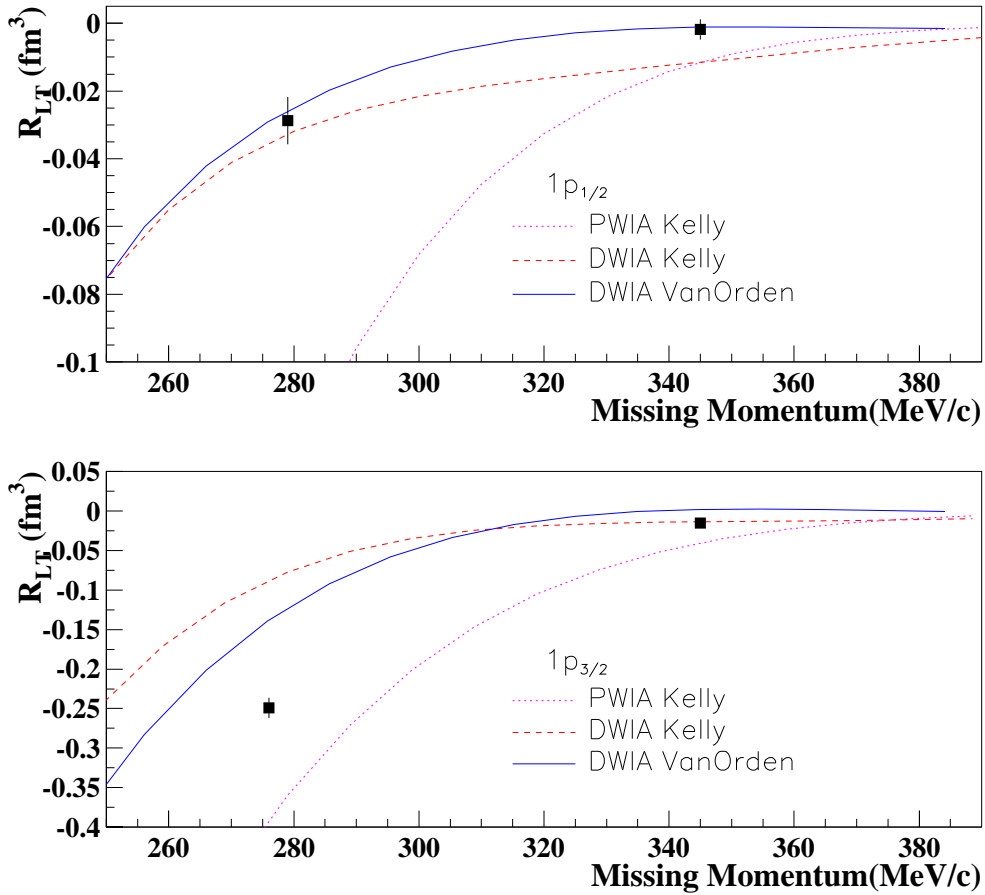


Figure 4-7: An enlargement of the high missing momentum region of Figure 4-6.

Figure 4-7 is an enlargement of the high missing momentum region of Figure 4-

6. For the  $1p_{1/2}$  state,  $R_{LT}$  agrees reasonably with both DWIA calculations. For the  $1p_{3/2}$  state,  $R_{LT}$  agrees only with the DWIA calculation of Kelly at 345 MeV/c missing momentum.

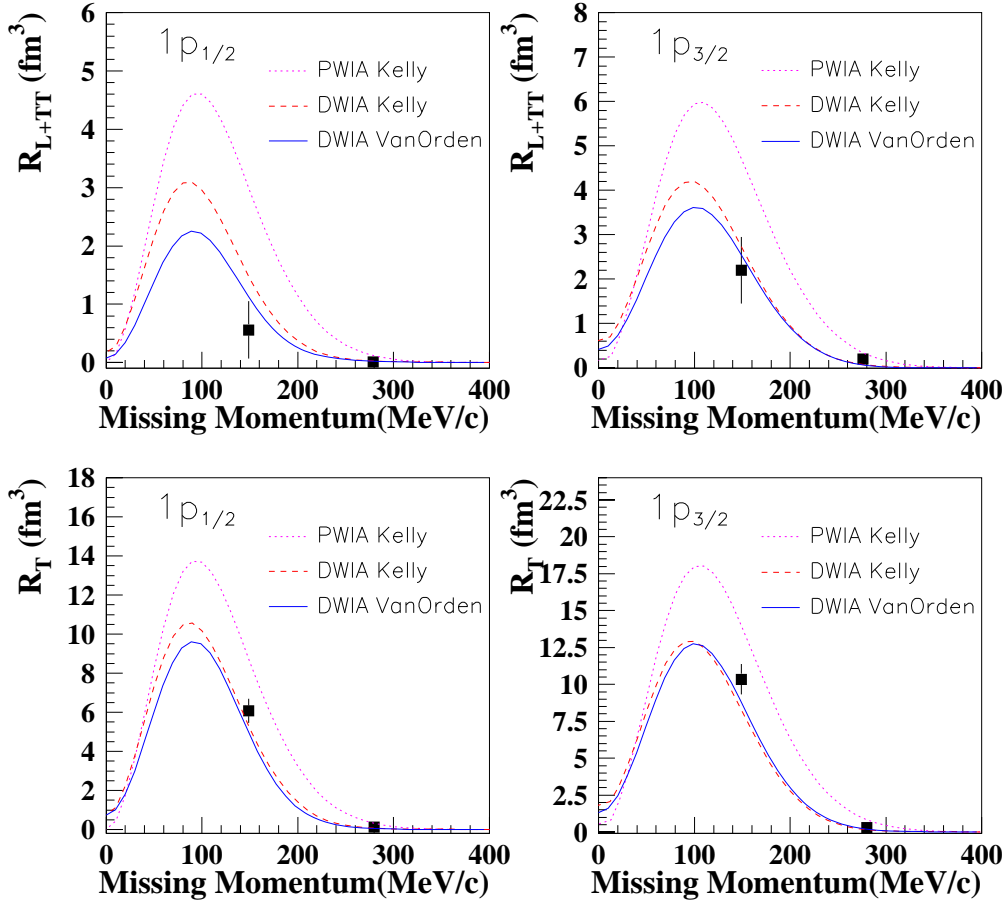


Figure 4-8: Comparison of  $R_{L+TT}$  and  $R_T$  with the calculations. The Coulomb gauge was used.

Figure 4-8 shows a comparison of separated  $R_{L+TT}$  and  $R_T$  with the calculations.

At a missing momentum of  $\sim 149$  MeV/c, the data agree very well with both DWIA calculations.

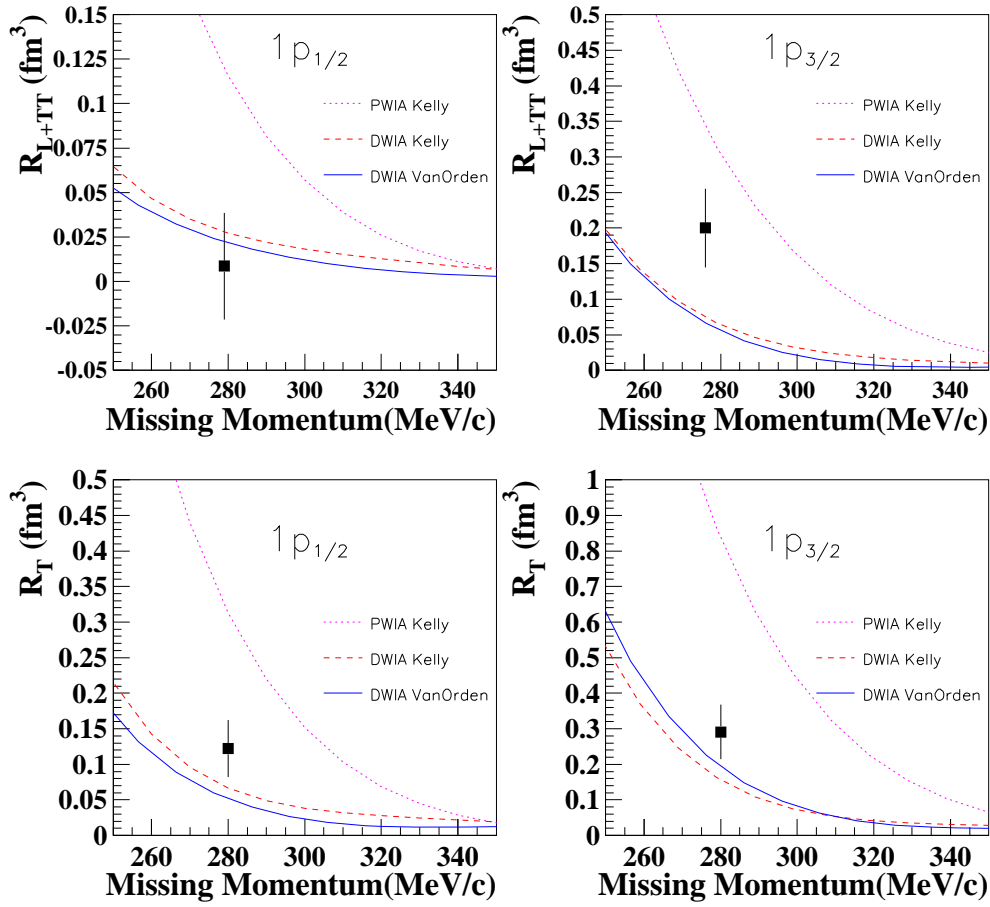


Figure 4-9: An enlargement of the high missing momentum region of Figure 4-8.

Figure 4-9 is an enlargement of the high missing momentum region of Figure 4-8. Except the fact that  $R_{L+TT}$  lies away from both DWIA calculations for the  $1p_{3/2}$  state, the data agrees with both DWIA calculations reasonably well.

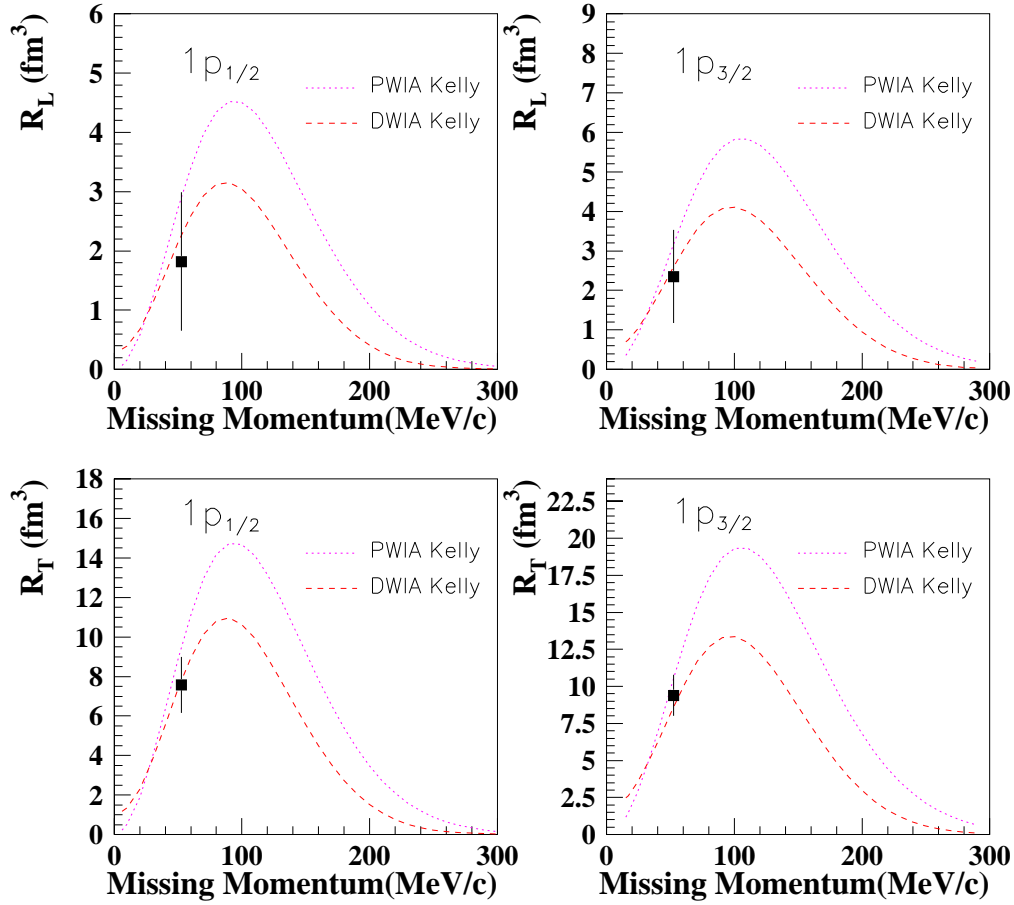


Figure 4-10: Comparison of  $R_L$  and  $R_T$  with the calculations of Kelly. The calculations used the Coulomb gauge.

Figure 4-10 shows the comparison of separated  $R_L$  and  $R_T$  with the calculations of Kelly. Because of a cut on missing momentum to remove the  $H(e, e'p)$  radiative tail, this data set is not in truly parallel kinematics. The data agree with the DWIA calculation.

### 4.3 Summary and Conclusions

Cross sections for the  $^{16}\text{O}(e, e'p)$  reaction have been measured in the quasielastic region with  $Q^2 = 0.8 \text{ (GeV/c)}^2$  in perpendicular kinematics. The three beam energies (843.2 MeV, 1642.5 MeV and 2441.6 MeV) were employed to separate the response functions  $R_{L+TT}$ ,  $R_T$ , and  $R_{LT}$  for  $1p_{1/2}$  and  $1p_{3/2}$  states.  $R_{LT}$  and  $A_{LT}$  are obtained up to 345 MeV/c in missing momentum.  $R_{L+TT}$  and  $R_T$  are separated up to 279 MeV/c in missing momentum.  $R_L$  and  $R_T$  are separated at 52.5 MeV/c in missing momentum for the data taken with hadron arm along  $\vec{q}$ .

The results have been compared to a non-relativistic calculation from Kelly and a relativistic calculation from Van Orden. The conclusions can be summarized as follows:

- $R_{LT}$  and  $A_{LT}$  have been measured with 2441.6 MeV beam and 1642.5 MeV beam at  $\theta_{pq} = 8^\circ$  (missing momentum  $\sim 150 \text{ MeV/c}$ ). The two measurements are in good agreement. This indicates that the systematic error for this experiment is very small.
- Cross sections measured with 2441.6 MeV incident beam agree with the standard DWIA calculations (both relativistic and non-relativistic) with spectroscopic factors between 60 and 75% for the  $1p_{1/2}$  and  $1p_{3/2}$  states for missing momentum less than 280 MeV/c. This data set is in good agreement with the data of Leuschner *et al.*[11], but disagrees with the data of Blomqvist *et al.*[15] At missing momentum larger than 280 MeV/c, neither of the DWIA calculations can predict the cross section for the  $1p$  states in a consistent manner.
- The separated response functions  $R_{L+TT}$ ,  $R_T$ , and  $R_{LT}$  agree reasonably well with the standard DWIA calculations (both relativistic and non-relativistic) with spectroscopic factors between 60 and 75% for the  $1p_{1/2}$  and  $1p_{3/2}$  states for missing momentum less than 150 MeV/c. Neither of the DWIA calculations is

consistent with all the data points for a missing momentum of 280 MeV/c. The separated  $R_L$  and  $R_T$  at 52.5 MeV/c missing momentum agree with the DWIA calculation of Kelly.

- The left-right asymmetry measurement is compared to the non-relativistic DWIA calculations from Kelly using the Landau gauge, the Coulomb gauge, and the Weyl gauge. The calculations using the Coulomb gauge and the Weyl gauge give similar results. The measured left-right asymmetry is not precise enough to distinguish between them. However, the Weyl gauge produces very different results. The data does not support the calculation using the Weyl gauge.
- The left-right asymmetry measurement has been compared to the non-relativistic DWIA calculation of Kelly and the relativistic DWIA calculation of Van Orden. These two calculations differ tremendously at high missing momentum. The data favors the relativistic calculation.

This experiment has provided a theoretically challenging and experimentally unique data set for the study of the quasielastic  $^{16}\text{O}(e, e'p)(1p)^{-1}$  reaction at high missing momentum  $Q^2 = 0.8 \text{ (GeV/c)}^2$  (the  $s$ -state and continuum of  $^{16}\text{O}$  have also been probed [58]). Future work should include a statistically more precise measurement of  $A_{LT}$  at higher missing momentum so that the relativistic effects in the  $(e, e'p)$  reaction will be investigated.

## Appendix A

# Beam Energy Measurement

### A.1 Introduction

Two identical spectrometers, HRSE and HRSH, each with a nominal relative momentum resolution of  $2.5 \times 10^{-4}$ , are used to detect electrons and hadrons respectively in Hall A. Three methods used to determine the incident beam energy are reported. They are called the  $^{12}\text{C}(e, e')$  *Technique*, the  $H(e, e'p)$  *Scattering Angle Technique*, and the  $(e, e'p)$  *Missing Energy Technique*.

### A.2 Beam Energy Measurement

#### A.2.1 $^{12}\text{C}(e, e')$ Technique

At present,  $^{12}\text{C}(e, e')$  is the most accurate measurement available for the beam energy determination in Hall A. It is also used to calibrate the spectrometer constants and dispersion coefficients needed to calculate the scattered electron energy  $E_f$ . The standard *differential recoil* procedure [53] does not supply enough precision without a large momentum transfer at the beam energies used at Jefferson Lab. For most nuclei, the counting rate is so low (due to the very small form factor) that the elastic

peak position cannot be determined accurately without an enormous amount of beam time. Therefore, an alternative technique using the excited states of  $^{12}\text{C}$  and the high momentum resolution of the spectrometers has been developed.

The relation between the scattered electron energy/momentum  $E_f/P_f$  and the focal plane position is (for extremely relativistic electrons)

$$E_f = P_f = \Gamma B \left[ 1 + \sum_{i=1}^2 d_i x_{fp}^i \right] \quad (\text{A.1})$$

where

$\Gamma$  [MeV/kG] is the magnetic constant,

$B$  [kG] is the dipole field strength,

$d_i (i = 1, 2)$  [ $\text{m}^{-i}$ ] are the spectrometer dispersion coefficients, and

$x_{fp}$  [m] is the kinematically-corrected focal plane position.

For each state of  $^{12}\text{C}$ , the energy  $E_f$  is related to the corresponding excitation energy  $E_x$  and incoming beam energy  $E_i$  by

$$E_f = \frac{E_i - E_{loss1} - E_x \left[ 1 + \frac{E_x}{2M_t} \right]}{f_{rec}} - E_{loss2} \quad (\text{A.2})$$

where

$M_t$  [MeV] is the mass of the target nucleus,

$f_{rec}$  is the recoil factor,  $f_{rec} = 1 + 2(E_i - E_{loss1}) \sin^2(\theta/2)/M_t$ ,

$E_{loss1}$  [MeV] is the mean energy loss before the scattering,

$E_{loss2}$  [MeV] is the mean energy loss after the scattering,  $E_{loss1,2} = 0.154(Z/A)t_{1,2}(19.6 + \ln(t_{1,2}/\rho))$ ,

$t_{1,2}$  [g/cm<sup>2</sup>] are the effective thicknesses of the material the electron passes through,  
 and  
 $\rho$  [g/cm<sup>3</sup>] is the density of the material.

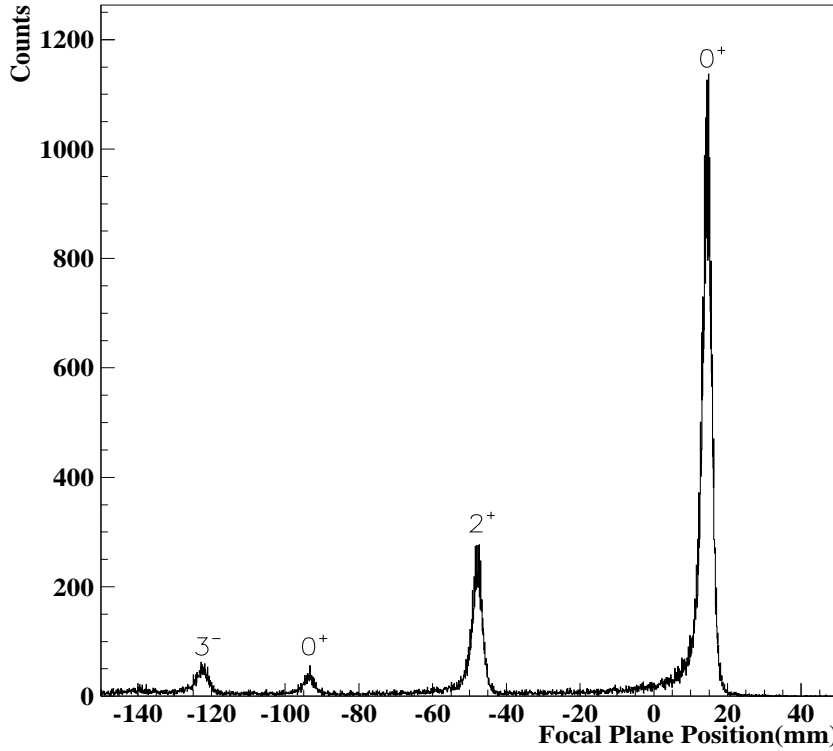


Figure A-1:  $^{12}\text{C}(e, e')$  spectrum at the HRSE focal plane. The nominal beam energy is 845 MeV, and the scattering angle is  $16^\circ$ . The four states are the ground state  $0^+$ , and the excited states  $2^+$  ( $4.4390 \text{ MeV} \pm 0.3 \text{ keV}$ ),  $0^+$  ( $7.6542 \text{ MeV} \pm 0.2 \text{ keV}$ ), and  $3^-$  ( $9.6410 \text{ MeV} \pm 5.0 \text{ keV}$ ) [55].

By varying the dipole field  $B$  and the quadrupole fields to maintain the same tune for the spectrometer, the elastic peak position on the focal plane may be shifted. Using (A.1), the dispersion coefficients  $d_i$  ( $i = 1, 2$ ) can be extracted without knowledge of either the beam energy  $E_i$  or the magnetic constant  $\Gamma$ . The results that follow are not affected by including a third order term in  $x_{fp}$ . The coefficient  $d_3$  is the same size as its error bar.

The difference between the ground state and the excited  $3^-$  state for a fixed B field is given by

$$\frac{E_x[1 + \frac{E_x}{2M_t}]}{f_{rec}} = \Gamma B(\sum_{i=1}^2 d_i x_1^i - \sum_{i=1}^2 d_i x_2^i) \quad (\text{A.3})$$

and therefore

$$\Gamma = \frac{E_x[1 + \frac{E_x}{2M_t}]}{f_{rec}B(\sum_{i=1}^2 d_i x_1^i - \sum_{i=1}^2 d_i x_2^i)} \quad (\text{A.4})$$

where  $x_1$  and  $x_2$  are the focal plane coordinates for these two states.

For a beam energy  $E_i = 845$  MeV and a scattering angle  $\theta = 16^\circ$ ,  $f_{rec} = 1.0029$ . It is very insensitive to either the incident beam energy or the scattering angle. For example, if the incident beam energy changes by 1%,  $f_{rec}$  changes by only  $3 \times 10^{-5}$ , while if the scattering angle is off by 1 mrad,  $f_{rec}$  is only affected by  $1 \times 10^{-5}$ . Therefore, using (A.4),  $\Gamma$  may be extracted, and then using (A.1) and (A.2), the beam energy  $E_i$  may be calculated. This procedure is performed in an iterative manner. In practice, a global least-squares fit is applied to (A.1), (A.2), and (A.4) for all the data points to obtain  $\Gamma$ ,  $d_i (i = 1, 2)$ , and the beam energy  $E_i$ .

In April 1997,  $^{12}\text{C}(e, e')$  data were taken simultaneously for both spectrometers with  $\Delta B/B = -4.5\%$ ,  $-3.0\%$ ,  $-1.5\%$ ,  $0\%$ ,  $1.5\%$ ,  $3.0\%$ , and  $4.5\%$ . The HRSE angle was  $16.024^\circ$  while the HRSB angle was  $16.020^\circ$ . The angles of the spectrometers were surveyed to better than 0.5 mrad. A  $55.8 \text{ mg/cm}^2$   $^{12}\text{C}$  target was chosen so that the energy loss in the target ( $\sim 61$  keV) as well as radiative effects were small. For each  $\Delta B/B$ , more than 150,000 events were collected for each arm. Two NMR probes located on the high field side and the low field side were used to measure the average dipole field for the HRSE, while there was only one NMR probe located on the low field side for the HRSB dipole. According to HRSB dipole field mapping, the ratio of the average field to the low field is 1.0665 [56][57]. The B field was known to better

than  $1 \times 10^{-5}$ .

Since the FWHM relative momentum resolution is  $2.5$  to  $4 \times 10^{-4}$  for the HRS, the peak width (FWHM) on the focal plane is  $3$  to  $5$  mm. The resolution change [50] along the focal plane indicates a less than  $0.2$  mm shift in the physical meaning of the maximum likelihood of each peak. However, this shift should track with the resolution and can be described by the quadratic term. The systematic shift of the peak due to the wire positioning is less than  $0.05$  mm. Thus, the peak position can be determined to  $< 0.5$  mm, or  $< 35$  keV. The excitation energy uncertainty is less than  $5$  keV. The contribution to the overall error from other sources is very small. The highest excitation energy is  $9.641$  MeV, and therefore the relative error in the beam energy is  $\sim 36 \text{ keV} / 9.641 \text{ MeV} = 3.7 \times 10^{-3}$  for each measurement. To good approximation, the resulting uncertainty from the  $6$  independent  $\Delta B/B$  data points is  $3.7 \times 10^{-3} / \sqrt{6} = 1.5 \times 10^{-3}$ .

Run #	HRSE B (kG)	HRSH B (kG)	$J^P$	Excitation (MeV)	HRSE $x_{fp}$ (m)	HRSH $x_{fp}$ (m)
6640	3.16670	2.96950	$0^+$	0.0000	0.53401	0.53224
			$2^+$	4.4390	0.47718	0.47535
			$0^+$	7.6540	0.43511	0.43409
			$3^-$	9.6410	0.40916	0.40788
6644	3.21660	3.01628	$0^+$	0.0000	0.36505	0.36240
			$2^+$	4.4390	0.30665	0.30318
			$0^+$	7.6540	0.26372	0.25977
			$3^-$	9.6410	0.23707	0.23268
6649	3.26634	3.06280	$0^+$	0.0000	0.18949	0.18375
			$2^+$	4.4390	0.12927	0.12289
			$0^+$	7.6540	0.08474	0.07809
			$3^-$	9.6410	0.05704	0.04992
6656	3.31585	3.10940	$0^+$	0.0000	0.01467	0.00798
			$2^+$	4.4390	-0.04778	-0.05486
			$0^+$	7.6540	-0.09338	-0.10133
			$3^-$	9.6410	-0.12226	-0.13056
6658	3.36577	3.15610	$0^+$	0.0000	-0.16212	-0.17277
			$2^+$	4.4390	-0.22679	-0.23779
			$0^+$	7.6540	-0.27392	-0.28632
			$3^-$	9.6410	-0.30383	-0.31615
6665	3.41547	3.20270	$0^+$	0.0000	-0.34166	-0.35599
			$2^+$	4.4390	-0.40799	-0.42322
			$0^+$	7.6540	-0.45729	-0.47308
			$3^-$	9.6410	-0.48754	-0.50421
6672	3.46518	3.24940	$0^+$	0.0000	-0.52528	-0.54633

Table A.1:  $^{12}\text{C}(e, e')$  data for HRSE and HSRH.

The least-squares fits were applied to the HRSE data and HRSH data listed in Table A.1. The  $\chi^2$ -test for each arm independently indicated that run 6644 was

suspect ( $\chi^2 \sim 9$ ), and it was removed from the data set. The final results (including the uncertainties) are summarized in Table A.2 and Table A.3.

	From HRSE	From HRSH
Beam Energy	$842.5 \pm 1.7$ MeV	$843.9 \pm 1.6$ MeV
$\chi^2$	1.42	1.20
Averaged Beam Energy	$843.2 \pm 1.2$ MeV	
Nominal Beam Energy	845.0 MeV	

Table A.2: Beam energy from  $^{12}\text{C}(e, e')$ .

	$\Gamma$ (MeV/kG)	$d_1$ ( $\times 10^{-2}$ m $^{-1}$ )	$d_2$ ( $\times 10^{-2}$ m $^{-2}$ )
HRSE	$253.22 \pm 0.36$	$8.506 \pm 0.017$	$1.025 \pm 0.019$
HRSH	$270.21 \pm 0.38$	$8.409 \pm 0.017$	$1.098 \pm 0.024$

Table A.3: Magnetic constants and dispersion coefficients for HRS.

If the hadron arm dipole low field is scaled to the average field by the factor of 1.0665,  $\Gamma$  for the HRSH becomes 253.36 MeV/kG, which agrees with  $\Gamma$  for the HRSE to  $6 \times 10^{-4}$ . One factor which might contribute to this difference is that the position of the VDC pair with respect to the central ray might be different for the two arms. For each spectrometer, a fixed point on the first wire plane was chosen as the origin of the focal plane coordinate system [50]. The coordinate of the intersection of the central ray and the focal plane depends on where the VDCs are placed. If the VDC pair is shifted by a small amount, all the parameters will be changed accordingly.

Consider a shift of  $x_0$  from the true central ray,

$$\begin{aligned}
E_f &= \Gamma B[1 + d_1 x_{fp} + d_2 x_{fp}^2] \\
&= \Gamma B[1 + d_1(x_{fp} - x_0 + x_0) + d_2(x_{fp} - x_0 + x_0)^2] \\
&= \Gamma B[1 + d_1(x'_{fp} + x_0) + d_2(x'_{fp} + x_0)^2] \\
&= \Gamma' B[1 + d'_1 x'_{fp} + d'_2 x'^2_{fp}]
\end{aligned} \tag{A.5}$$

while

$$\Gamma' = \Gamma[1 + d_1 x_0 + d_2 x_0^2] \tag{A.6}$$

$$d'_1 = (d_1 + 2d_2 x_0)/(1 + d_1 x_0 + d_2 x_0^2) \tag{A.7}$$

$$d'_2 = d_2/(1 + d_1 x_0 + d_2 x_0^2) \tag{A.8}$$

$$x'_{fp} = x_{fp} - x_0. \tag{A.9}$$

The position of the central ray in each of the spectrometers, as described by the VDC pair, is correct to better than 5 mm [59][60], which implies an uncertainty of  $4 \times 10^{-4}$  in  $\Gamma$ . Thus, the two dipoles are identical within  $7 \times 10^{-4}$ .

### A.2.2 H( $e, e'p$ ) Scattering Angle Technique

For the H( $e, e'p$ ) reaction, the beam energy  $E_i$  can be calculated from the proton mass  $M_p$ , the electron scattering angle  $\theta_e$ , the proton scattering angle  $\theta_p$ , and the energy loss before the scattering  $E_{loss}$ , according to

$$E_i = M_p \left( \cot \frac{\theta_e}{2} \cot \theta_p - 1 \right) + E_{loss}. \tag{A.10}$$

This method is totally independent of any other technique. However, the uncertainty in the beam energy is very sensitive to the knowledge of the spectrometer angles

$$\Delta E_i = -\frac{M_p \cot \theta_p}{2 \sin^2 \frac{\theta}{2}} \Delta \theta_e \quad (\text{A.11})$$

$$\Delta E_i = -\frac{M_p \cot \frac{\theta_e}{2}}{\sin^2 \theta_p} \Delta \theta_p. \quad (\text{A.12})$$

As an example, for the kinematics of E89-003, a one mrad uncertainty in angle could shift the beam energy by 0.5%. Thus, by comparing with the results from other methods, this technique can be used to determine the systematic uncertainty in the angular measurements.

The scattering angle of the particle  $\theta$  can be reconstructed from the spectrometer central angle  $\Theta_0$  and  $(\theta_{tg}, \phi_{tg})$  [52] according to

$$\theta = \arccos \frac{\cos \Theta_0 - \phi_{tg} \sin \Theta_0}{\sqrt{1 + \theta_{tg}^2 + \phi_{tg}^2}}, \quad (\text{A.13})$$

where  $\theta_{tg}$  and  $\phi_{tg}$  are the angles of the particle track with respect to the spectrometer central ray in the dispersive and transverse directions. The centroid of the resulting distribution (using (A.10) on an event-by-event basis) is the beam energy. A Monte Carlo simulation shows that the radiative tail can slightly shift the distribution ( $\sim 0.5$  MeV). Therefore, only those events under the elastic peak (within  $\pm 3\sigma$ ) are selected to avoid this effect.

Figures A-2, A-3, and A-4 show the reconstructed beam energies from  $\text{H}(e, e'p)$  data taken with the waterfall target [23] during E89-003. The width of the distributions is mostly due to multiple scattering. The extracted beam energies along with the uncertainty from the Gaussian fit are summarized in Table A.4.

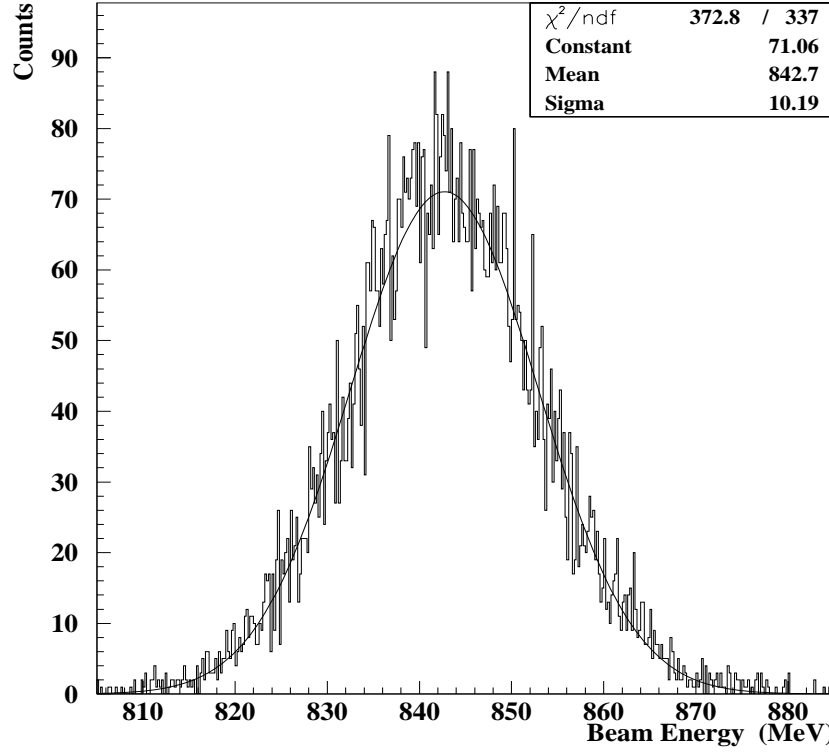


Figure A-2: Beam energy from  $\text{H}(e, e'p)$  ( $\theta_e = 100.70^\circ$ ,  $\theta_p = -23.20^\circ$ ).

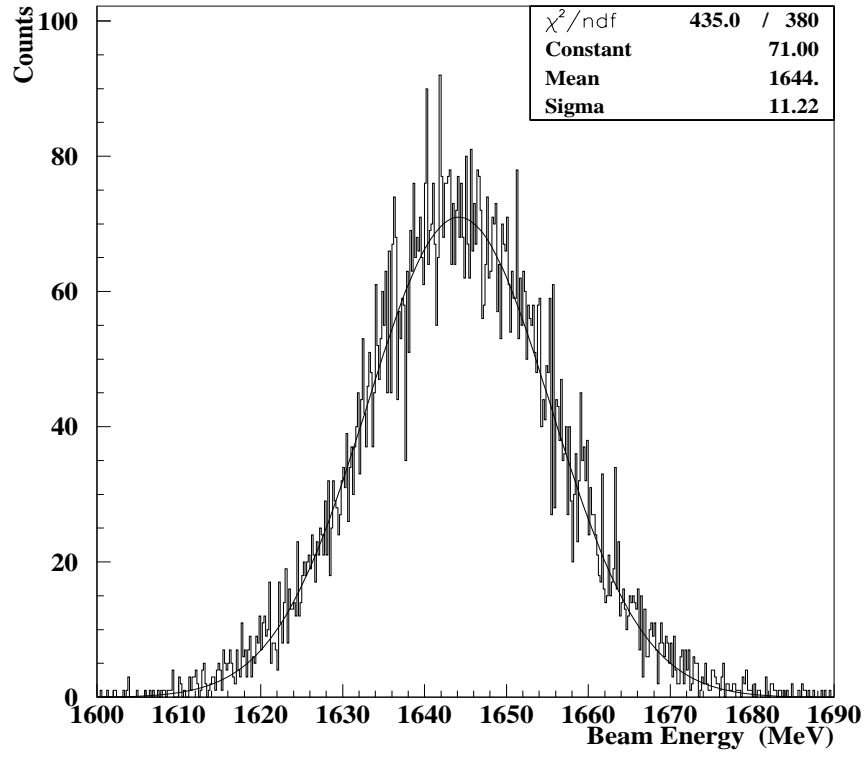
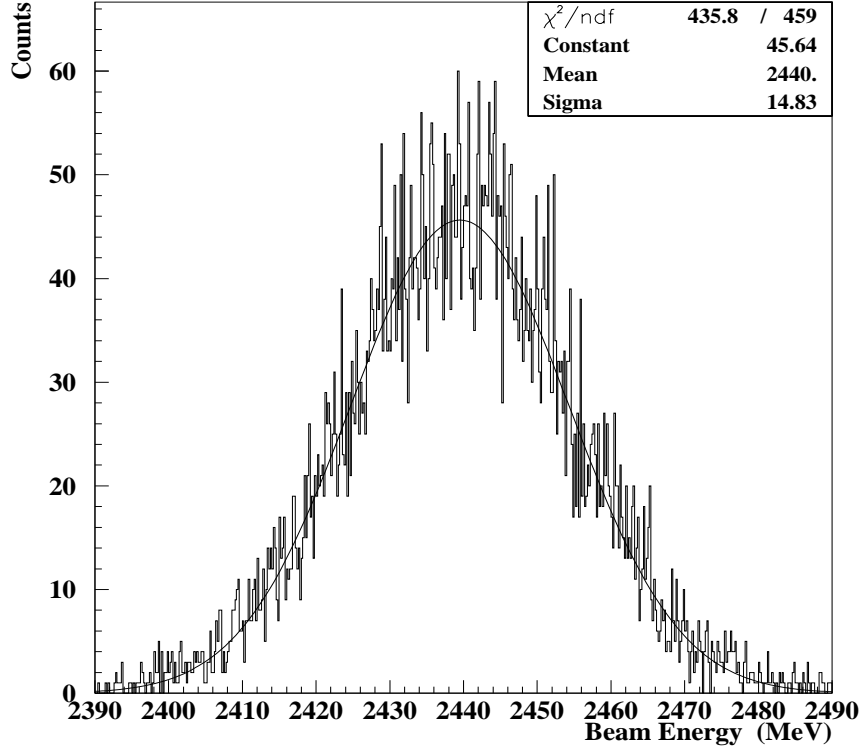


Figure A-3: Beam energy from  $\text{H}(e, e'p)$  ( $\theta_e = 37.17^\circ$ ,  $\theta_p = -46.45^\circ$ ).

Figure A-4: Beam energy from  $H(e, e'p)$  ( $\theta_e = 23.38^\circ$ ,  $\theta_p = -52.50^\circ$ ).

Nominal Beam Energy (MeV)	From $H(e, e'p)$ (MeV)
845.0	$842.7 \pm 0.1$
1645.0	$1644.1 \pm 0.1$
2445.0	$2439.9 \pm 0.2$

Table A.4: Beam energies from  $H(e, e'p)$ .

The angles  $\theta_e$  and  $\theta_p$  were measured by surveying the sieve slit central hole positions with respect to the beam line. The uncertainty in  $\theta_e$  and  $\theta_p$  from the survey was less than 0.5 mrad [61]. This results in a beam energy uncertainty of less than  $2.5 \times 10^{-3}$ .

**A.2.3  $^{16}\text{O}(e, e'p)$  Missing Energy Technique**

The missing energy technique relies on the calibration of the magnetic constants from  $^{12}\text{C}(e, e')$  to determine the beam energy. For the  $^{16}\text{O}(e, e'p)$  reaction

$$E_{miss} = E_i - E_f - T_p - T_{A-1} - E_{loss1} - E_{loss2} \quad (\text{A.14})$$

$$T_p = \sqrt{M_p^2 + p_p^2} - M_p \quad (\text{A.15})$$

$$T_{A-1} = (\vec{q} - \vec{p}_p)^2 / 2M_{A-1}^* \quad (\text{A.16})$$

and conservation of energy requires

$$E_{miss} = M_{A-1}^* + M_p - M_A \quad (\text{A.17})$$

where

$E_{miss}$  is the missing energy,

$E_i$  is the incident electron energy,

$E_f$  is the scattered electron energy,

$T_p$  is the kinetic energy of the knocked-out proton,

$T_{A-1}$  is the kinetic energy of the recoil nucleus (insensitive to the beam energy),

$E_{loss1}$  is the energy loss of electron before the scattering,

$E_{loss2}$  is the total energy loss of both the electron and the proton after the scattering,

$\vec{q}$  is the momentum transfer,

$\vec{p}_p$  is the proton momentum,

$M_{A-1}^*$  is the mass of the recoil nucleus, and

$M_A$  is the mass of the target.

Thus, the missing energy is just the binding energy of the knocked-out proton. For  $^{16}\text{O}$ , the  $1p_{1/2}$  proton binding energy is 12.1 MeV and the  $1p_{3/2}$  proton binding energy is 18.4 MeV. From the  $^{16}\text{O}(e, e'p)$   $1p_{1/2}$ -shell knockout events, the beam energy  $E_i$  (MeV) can be reconstructed using

$$E_i = 12.1 \text{ MeV} + E_f + T_p + T_{A-1} + E_{loss1} + E_{loss2} \quad (\text{A.18})$$

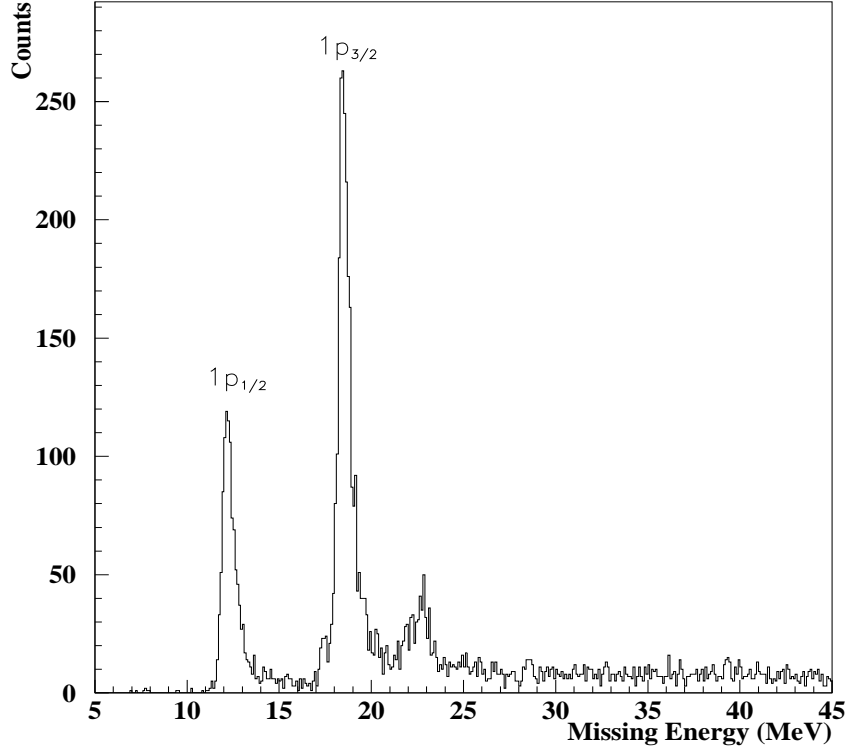
where  $E_f$ ,  $T_p$ , and  $T_{A-1}$  are calculated using the scattered electron momentum  $\vec{p}_e$  and the knocked out proton momentum  $\vec{p}_p$

$$|\vec{p}_{e,p}| = \Gamma_{e,p} B_{e,p} \left[ 1 + \sum_{i=1}^2 d_i^{e,p} (x_{fp}^{e,p})^i \right] \quad (\text{A.19})$$

where  $(e, p)$  represent HRSE and HRSH respectively.

The error in the reconstructed beam energy depends on the error in  $\Gamma_e$  and  $\Gamma_h$  coming from the  $^{12}\text{C}(e, e')$  data, and is given by

$$\delta E_i = \frac{\delta \Gamma_e}{\Gamma_e} E_f + \frac{\delta \Gamma_p}{\Gamma_p} \frac{p_p^2}{T_p + M_p}. \quad (\text{A.20})$$

Figure A-5: Missing energy spectrum for  $^{16}\text{O}(e, e'p)$ .

Figures A-6, A-7, and A-8 show the beam energies calculated for a sampling of each run period of E89-003 using the  $^{16}\text{O}(e, e'p)$  missing energy technique. The first uncertainty quoted arises from the uncertainties in  $\Gamma_e$  and  $\Gamma_p$ , and the second uncertainty quoted indicates the beam energy fluctuation from run-to-run.

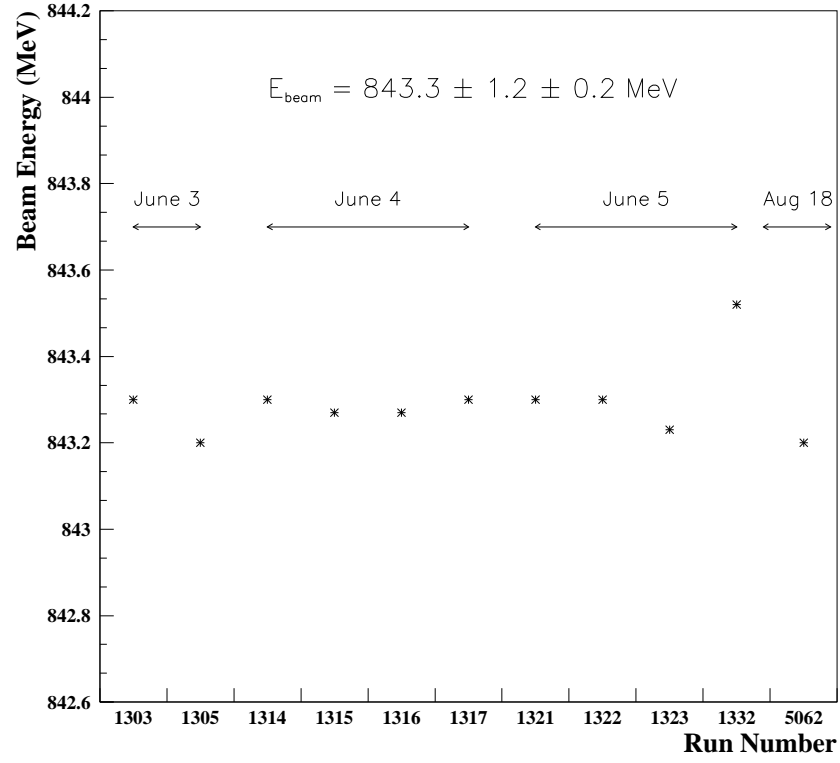


Figure A-6: Beam energy for nominal 845 MeV runs.

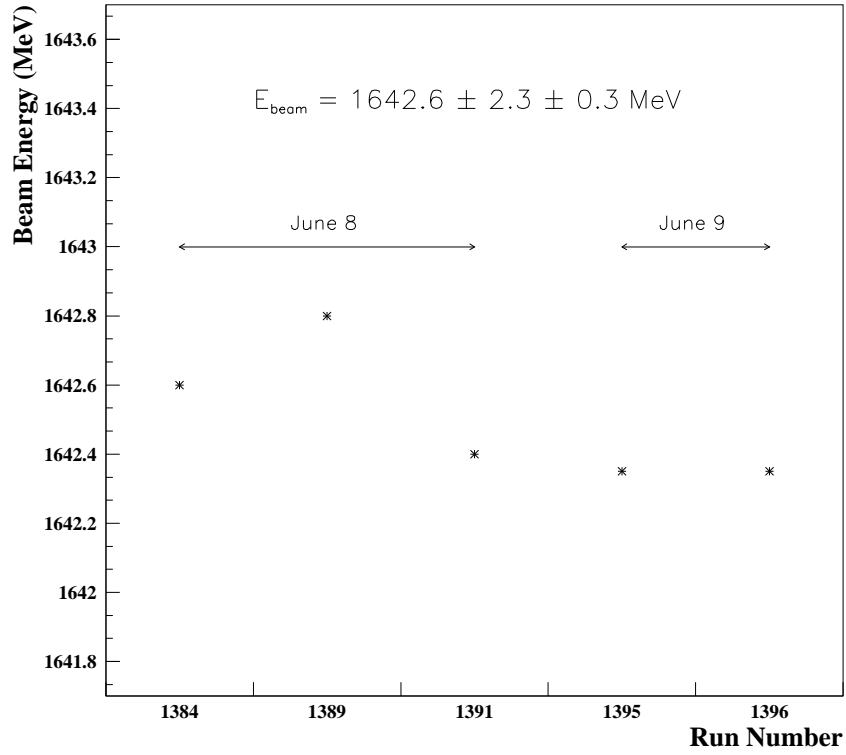


Figure A-7: Beam energy for nominal 1645 MeV runs.

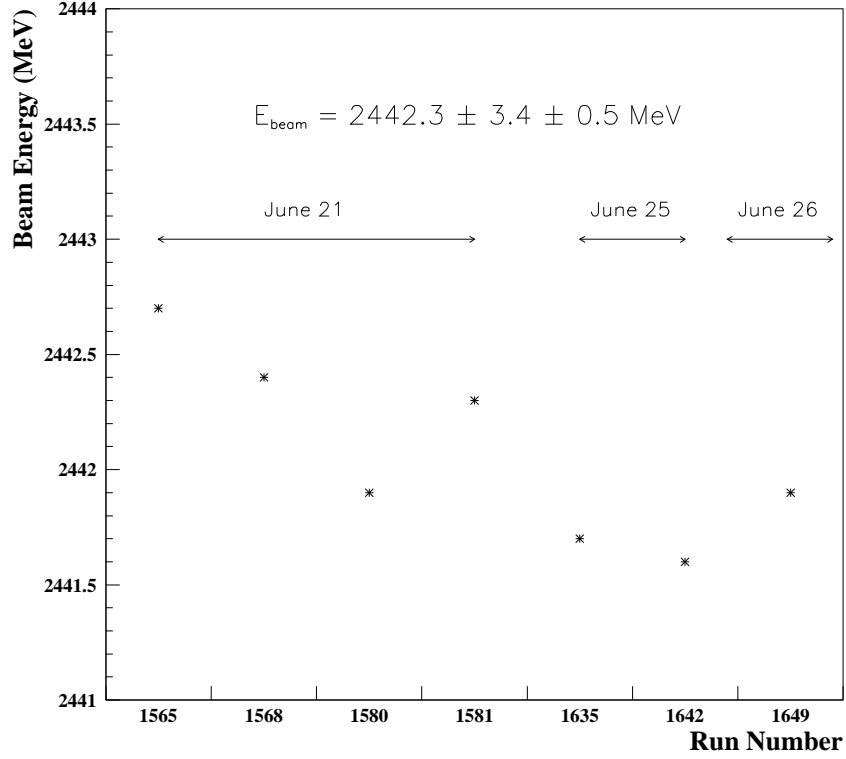


Figure A-8: Beam energy for nominal 2445 MeV runs.

Nominal Beam Energy (MeV)	Beam Energy from $^{16}\text{O}(e, e'p)$ (MeV)
845.0	$843.3 \pm 1.2 \pm 0.2$
1645.0	$1642.6 \pm 2.3 \pm 0.3$
2445.0	$2442.3 \pm 3.4 \pm 0.5$

Table A.5: Beam energies from the  $^{16}\text{O}(e, e'p)$  missing energy technique.

### A.3 Conclusions

Nominal (MeV)	From $^{12}\text{C}(e, e')$ (MeV)	From $\text{H}(e, e'p)$ (MeV)	From $^{16}\text{O}(e, e'p)$ (MeV)	$\Delta\theta$ (mrad)
845.0	$843.2 \pm 1.2$	$842.7 \pm 0.1$	$843.3 \pm 1.2 \pm 0.2$	0.3
1645.0	N/A	$1644.1 \pm 0.1$	$1642.5 \pm 2.3 \pm 0.3$	-0.3
2445.0	N/A	$2439.9 \pm 0.2$	$2442.3 \pm 3.4 \pm 0.5$	0.3

Table A.6: A comparison of beam energies from the presented methods.

Table A.6 lists the beam energies determined using the different methods.  $\Delta\theta$  is the maximum angular discrepancy by comparing the results from the  $\text{H}(e, e'p)$  technique and the results from the  $^{16}\text{O}(e, e'p)$  missing energy technique. For E89-003, the beam energies were obtained to  $1.5 \times 10^{-3}$  by combining  $^{12}\text{C}(e, e')$  and  $^{16}\text{O}(e, e'p)$  missing energy measurements. The beam energy shift from run-to-run during the entire experiment was less than  $2 \times 10^{-4}$ . The deviation of the measured beam energies from the nominal beam energies (provided by the Machine Control Center) is about  $2.0 \times 10^{-3}$ . The agreement to within  $1 \times 10^{-3}$  of the beam energies extracted from the  $\text{H}(e, e'p)$  technique with the results from the other methods implies that the systematic uncertainty for the angle determination is less than 0.3 mrad.

## Appendix B

### Matrix Elements of HRSs

The matrix elements obtained from the optics study with  $^{12}\text{C}(e, e')$  at 845 MeV beam energy and  $16^\circ$  scattering angle are listed in the following tables.

$Q_{ijkl}$	i=0	i=1	i=2	i=3
$t_{i000}$	-1.0027E+00	-3.3012E-01	-3.2536E-02	1.2912E-03
$y_{i000}$	-7.2837E-03	3.2563E-03		
$p_{i000}$	-2.1774E-03	-8.9684E-04		
$D_{i000}$		8.5060E-02	1.0250E-02	
$D_{i100}$	-3.5017E-02	2.6963E-01	4.2004E-02	-2.4595E-02
$D_{i200}$	-1.4479E+00	5.7568E-01		
$D_{i002}$	2.4081E-01	-7.7477E-02	-6.7727E-01	
$D_{i020}$	3.6117E-01	-7.5655E-01	-7.9962E-01	
$D_{i011}$	2.6138E-01	6.8103E-01		
$D_{i300}$	2.4742E+01			
$D_{i120}$	-3.1889E+01	1.9336E+01		
$D_{i102}$	-2.6759E+01			
$D_{i111}$	-1.5159E+01	-9.0963E+01		
$D_{i400}$	1.9030E+03			
$D_{i202}$	-9.9579E+02			
$D_{i220}$	-1.6571E+03			
$D_{i211}$	1.9152E+03			
$T_{i100}$	-2.2707E+00	4.9131E-01	1.4908E-02	
$T_{i200}$	-7.2421E+00	2.6135E+00		
$T_{i002}$	1.2824E-01	4.1137E-01	3.6680E+00	
$T_{i020}$	-4.2284E-01	-3.6365E-01		

Table B.1: HRSE matrix elements obtained at 845 MeV beam energy.

$Q_{ijkl}$	i=0	i=1	i=2	i=3
$T_{i011}$	1.0730E+00	-1.4196E+00	-3.7090E+00	
$T_{i120}$	2.5136E+01			
$T_{i102}$	2.0016E+01	-5.1216E+01		
$T_{i300}$	1.0336E+02			
$T_{i040}$	5.9637E+02			
$T_{i022}$	1.0304E+03			
$T_{i111}$	-2.1599E+01			
$T_{i202}$	-5.4090E+02			
$T_{i013}$	-1.0237E+03			
$T_{i031}$	-1.4686E+03			
$T_{i400}$	5.0437E+03			
$P_{i001}$	-6.9215E-01	-9.8569E-02	2.6903E-01	-1.0106E-01
$P_{i010}$	-3.2907E-01	2.7852E-01	-9.4349E-02	1.2984E-01
$P_{i101}$	5.9176E+00	-7.4720E-01	2.6263E+00	
$P_{i110}$	3.0497E+00	-1.4259E-01	-7.7373E+00	
$P_{i012}$	-3.9218E+00	5.1591E+01		
$P_{i003}$	1.6310E+01	-3.0004E+01		
$P_{i201}$	3.1715E+00	-1.5169E+02		
$P_{i210}$	-9.3060E+01	7.9745E+01		
$P_{i030}$	-5.3575E+00			

Table B.2: HRSE matrix elements obtained at 845 MeV beam energy.

$P_{i021}$	-1.7005E+01	-1.0125E+02		
$P_{i103}$	-8.3756E+02			
$P_{i310}$	-1.8746E+03			
$P_{i112}$	1.2034E+03			
$P_{i121}$	-7.0797E+02			
$Y_{i001}$	6.6644E-01	-1.2792E+00	-5.9088E-01	1.0070E-01
$Y_{i010}$	-1.1716E+00	-7.3591E-01	2.0473E-01	
$Y_{i101}$	-5.5873E-01	-5.2015E+00	-4.7578E+00	
$Y_{i110}$	-1.2006E+01	-7.4347E-01		
$Y_{i012}$	4.9334E+00			
$Y_{i003}$	2.2622E+01			
$Y_{i201}$	4.5543E+02	2.3879E+02		
$Y_{i210}$	3.1102E+02	-9.1130E+01		
$Y_{i030}$	4.7275E+01			
$Y_{i021}$	6.1093E+01	1.8791E+02		
$Y_{i103}$	-7.9386E+02			
$Y_{i130}$	1.0332E+03			
$Y_{i112}$	1.8212E+03			
$Y_{i301}$	3.4467E+03			
$Y_{i310}$	2.0201E+03			
$Y_{i121}$	-2.0668E+03			

Table B.3: HRSE matrix elements obtained at 845 MeV beam energy.

$Q_{ijkl}$	i=0	i=1	i=2	i=3
$t_{i000}$	-1.0050E+00	-3.3613E-01	-4.0828E-02	4.1021E-03
$y_{i000}$	-2.8496E-03	-2.0963E-03		
$p_{i000}$	-1.5000E-03	3.7015E-03	5.4167E-04	-3.8885E-02
$D_{i000}$		8.4090E-02	1.0980E-02	
$D_{i100}$	-3.6552E-02	2.8788E-01	4.5414E-02	-2.4305E-01
$D_{i200}$	-1.8889E+00	2.3637E-01	4.2717E+00	
$D_{i002}$	6.5985E-03	3.4792E-01	-7.3869E-01	
$D_{i020}$	5.7923E-01	6.7117E-01	3.6213E-01	
$D_{i011}$	4.7218E-01	2.4993E-02	-5.0836E-01	
$D_{i300}$	3.0423E+01	-4.5712E+01		
$D_{i120}$	-6.6381E+00	5.4344E+01		
$D_{i102}$	-2.0548E+01	-8.2423E+00		
$D_{i111}$	-2.3487E+01	-3.6214E+01		
$D_{i400}$	2.1520E+03			
$D_{i202}$	-3.8587E+02			
$D_{i220}$	-4.8900E+02			
$D_{i022}$	-1.5905E+02			
$T_{i100}$	-2.2896E+00	5.0418E-01	3.5689E-02	-7.0449E-01
$T_{i200}$	-3.6320E+00	1.0594E+00	-1.2168E+00	
$T_{i002}$	9.2892E-01	-9.9527E-01	5.6382E-01	
$T_{i020}$	1.9557E-01	-5.5917E-01	1.8563E+00	
$T_{i011}$	2.3203E-01	-2.2600E+00		

Table B.4: HRSH matrix elements obtained at 845 MeV beam energy.

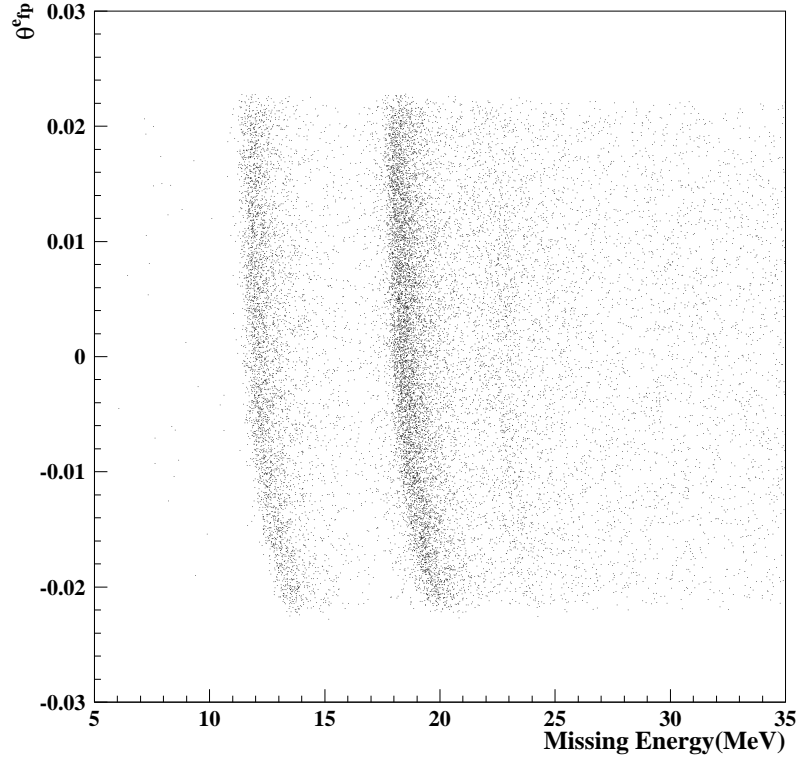
$Q_{ijkl}$	i=0	i=1	i=2	i=3
$T_{i120}$	-3.5913E+01	-5.0596E+01		
$T_{i102}$	7.0259E+00	-1.1836E+01		
$T_{i300}$	2.6225E+01	2.0447E+02		
$T_{i040}$	4.3965E+02			
$T_{i220}$	-2.6534E+03			
$T_{i022}$	6.7276E+02			
$T_{i111}$	-1.6025E+01			
$T_{i202}$	4.1458E+02			
$T_{i013}$	-9.8358E+02			
$T_{i031}$	-8.3672E+02			
$T_{i400}$	-3.2178E+03			
$P_{i010}$	-2.6977E-01	3.5996E-01	-2.9549E-01	-4.1009E-01
$P_{i001}$	-6.3921E-01	-1.3752E-01	2.5155E-01	3.3808E-02
$P_{i101}$	1.0219E+00	6.6895E+00		
$P_{i110}$	4.1184E+00	-1.4942E+00	-3.6635E+00	
$P_{i012}$	-2.7086E+01	9.6591E+01	6.8284E+01	
$P_{i003}$	2.2081E+01	-1.7388E+01		
$P_{i201}$	-4.4012E+01	-1.1585E+02		
$P_{i210}$	-8.0492E+01	4.5335E+01		
$P_{i030}$	-5.2006E+01	-6.8045E+01		

Table B.5: HRSH matrix elements obtained at 845 MeV beam energy.

$P_{i021}$	7.2137E+01	7.0909E+01		
$P_{i103}$	-8.0018E+02			
$P_{i310}$	-1.2265E+03			
$P_{i112}$	1.6526E+03			
$P_{i121}$	4.2314E+02			
$Y_{i001}$	7.2375E-01	-1.2442E+00	-6.1419E-01	-5.1404E-02
$Y_{i010}$	-1.3038E+00	-7.2763E-01	1.9965E-01	2.8169E-01
$Y_{i101}$	-2.6824E+00	-7.7489E+00		
$Y_{i110}$	-1.4394E+01	-5.8599E-01	-2.1977E+00	
$Y_{i012}$	1.2734E+02	-1.4658E+02		
$Y_{i003}$	-2.7597E+01	1.5418E+02		
$Y_{i201}$	4.4010E+02			
$Y_{i210}$	2.3204E+02	-1.4032E+02		
$Y_{i030}$	1.0307E+02	6.0966E+01		
$Y_{i021}$	-9.2602E+01	4.1490E+01		
$Y_{i103}$	7.4580E+02			
$Y_{i112}$	-8.2829E+02			
$Y_{i301}$	6.7646E+03			
$Y_{i310}$	4.2477E+03			

Table B.6: HRSH matrix elements obtained at 845 MeV beam energy.

During the experiment E89-003, data were taken at different nominal incident beam energies: 845 MeV, 1645 MeV, and 2445 MeV. The outgoing proton momentum was fixed at 972 MeV/c; however, the scattered electron momentum varied from 400 MeV/c, 1200 MeV/c to 2000 MeV/c. When the matrix elements obtained at 845 MeV were used for different central momenta, the missing energy resolution for  $^{16}\text{O}(e, e'p)$  became worse than what was expected. A dependence of missing energy on the  $\theta_{fp}^e$  was found.

Figure B-1: Missing energy vs  $\theta_{fp}^e$ .

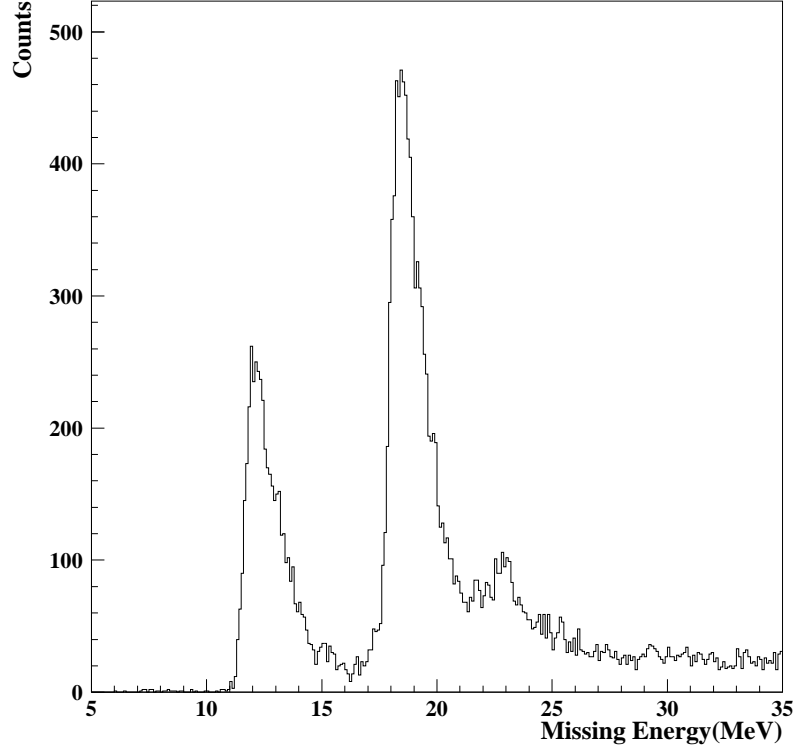


Figure B-2: Missing energy spectrum from  $^{16}\text{O}(e, e'p)$  at nominal 2445 MeV incident beam using the matrix elements obtained at 845 MeV. The FWHM missing energy resolution from the  $1p$ -shell is about 1.7 MeV.

This indicates a nonlinearity in the dipole field (the change of the dipole index). Since the angular reconstruction was not affected, only the matrix elements associated with the momentum reconstruction (the terms for the aberration correction) were modified.

If the energy loss of the particles in the target is ignored, the missing energy for  $^{16}\text{O}(e, e'p)$  is defined as

$$E_{miss} = E_{beam} - P_0^e c(1 + \delta_e) - T_p - T_R, \quad (\text{B.1})$$

where  $E_{beam}$  is the beam energy,  $P_0^e$  is the electron arm central momentum,  $\delta$  is the electron relative momentum,  $T_p$  is the proton kinetic energy, and  $T_R$  is the recoil energy. For the valence states, the missing energy spectrum should be a peak located at the binding energy of the state in question. Since the proton central momentum 972 MeV/c is close to the momentum 845 MeV/c where the optics study was performed, one can assume the reconstruction of the proton momentum is not changed. Therefore, the reconstruction of the scattered electron momentum has to be modified to remove the dependence of the missing energy on  $\theta_{fp}$ . One can use  $\delta'$  instead of  $\delta$  with

$$\delta'_e = \delta_e + f_1\theta_{fp}^e + f_2\theta_{fp}^{e2} \quad (\text{B.2})$$

so that the missing energy

$$E'_{miss} = E_{beam} - P_0^e c(1 + \delta') - T_p - T_R \quad (\text{B.3})$$

$$= E_{miss} - P_0^e (f_1\theta_{fp} + f_2\theta_{fp}^2) \quad (\text{B.4})$$

is independent of  $\theta_{fp}^e$ .  $f_1, f_2$  were obtained by using a second order polynomial to fit the curve of missing energy vs  $\theta_{fp}$ . Therefore, the matrix elements  $D_{0100}$  and  $D_{0200}$  for the HRSE have to be modified for that central momentum

$$D'_{0100} = D_{0100} + f_1 \quad (\text{B.5})$$

$$D'_{0200} = D_{0200} + f_2. \quad (\text{B.6})$$

Figure B-3 shows the missing energy vs.  $\theta_{fp}^e$  using the new matrix elements. Figure B-4 displays the missing energy spectrum using the modified matrix elements. The FWHM missing energy resolution was improved by nearly a factor of two.

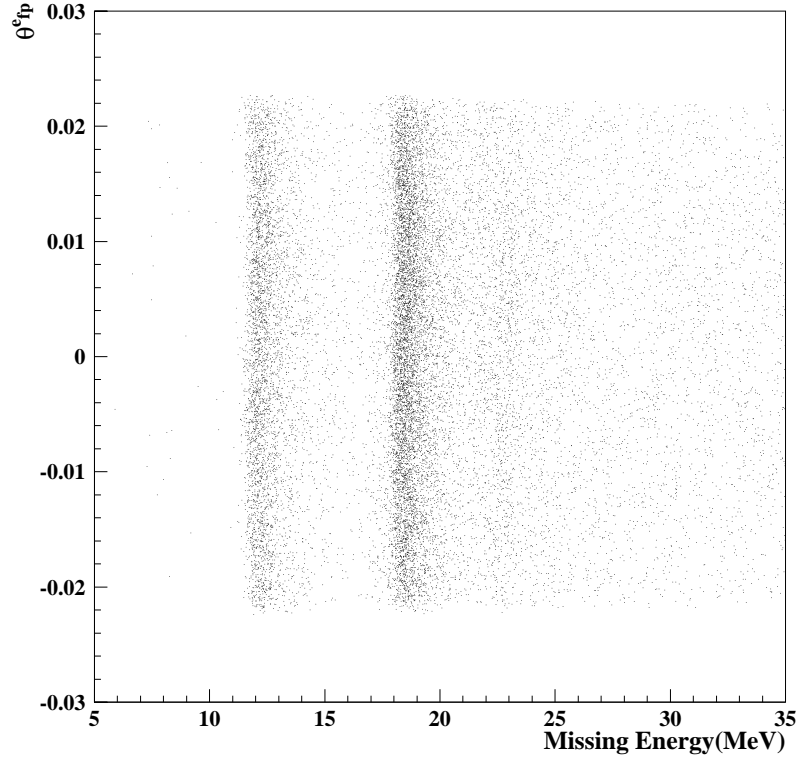


Figure B-3: Missing energy vs.  $\theta_{fp}^e$  for the 2445 MeV  $^{16}\text{O}(e, e'p)$  runs using the modified matrix elements.

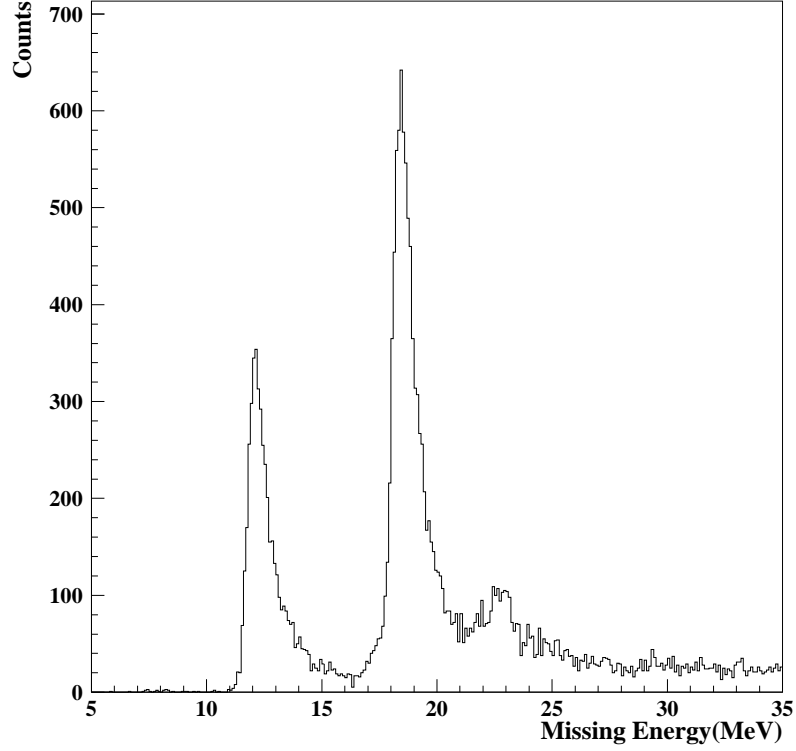


Figure B-4: Missing energy spectrum for the nominal 2445 MeV  $^{16}\text{O}(e, e'p)$  runs using the modified matrix elements. The FWHM missing energy resolution is about 0.9 MeV.

This procedure was performed for all three HRSE central momenta runs and the new matrix elements  $D_{0100}$  and  $D_{0200}$  are listed in Table B.7.

$P_0^e$ (MeV/c)	845	400	1200	2000
$D_{0100}$	-3.5017E-02	-1.0482E-02	-3.5181E-02	-4.9402E-02
$D_{0200}$	-1.4479E+00	-2.8899E+00	-1.4763E+00	-1.8889E+00

Table B.7: Modified HRSE matrix elements for different central momenta.

# Bibliography

- [1] R.R. Whitney *et al.*, Phys. Rev. **C9** 2230(1974).
- [2] E.J. Moniz, Phys. Rev. **184** 1154(1969).
- [3] T. De Forest, Saclay, CEA DPHN p223(1975).
- [4] G.B. West, Phys. Rep. **18C** 269(1975).
- [5] Y. Kowazoe, G. Takeda and H. Matsuzaki, Prog. Theo. Phys. **54**, 1394(1975).
- [6] J.J. Kelly, Adv. Nucl. Phys., **23** 75(1996)
- [7] T. De Forest, Nucl. Phys. **A392** 232(1983).
- [8] L. Chinitz *et al.*, Phys. Rev. Lett. **67** 568(1991).
- [9] C.M. Spaltro *et al.*, Phys. Rev. **C48** 2385(1993).
- [10] P. Schwandt *et al.*, Phys. Rev. **C26** 55(1982).
- [11] M. Leuschner, J.R. Calarco, F.W. Hersman *et al.*, Phys. Rev. **C49** 955(1994).
- [12] V. Van der Sluys, J. Ryckebusch, and M. Waroquier, Phys. Rev. **C49** 2695(1994).
- [13] J. Ryckebusch *et al.*, Nucl. Phys. **A476** 237(1988).
- [14] M. Cavinato *et al.*, Z. Phys. **A335** 401(1990).
- [15] K.I. Blomqvist *et al.*, Phys. Lett. **B344** 85(1995).

- [16] D.G. Ireland and G. van der Steenhoven, Phys. Rev. **C49** 2182(1994).
- [17] James J. Kelly, Phys. Rev. **C56** 2672(1997).
- [18] H. Serfeit *et al.*, Phys. Rev. **C47** 1615(1993).
- [19] D.G. Madland, Technical report No. LA-UR-97-0306, Los Alamos National Laboratory, 1997(unpublished).
- [20] E.D. Cooper, S. Hama, B.C. Clark, and R.L. Mercer, Phys. Rev. **C40** 297(1993).
- [21] James J. Kelly, Phys. Rev. **C54** 2547(1996).
- [22] K.G. Fissum, A Study of the Quasielastic ( $e, e'p$ ) Reaction in  $^{16}\text{O}$  at High Recoil Momentum, MIT-LNS Internal Report #02, 1997.
- [23] F. Garibaldi *et al.*, Nucl. Instrum. Methods **A314** 1 (1992).
- [24] K.B. Unser *Design and Preliminary Test of a Beam Intensity Monitor for LEP*, Proc. IEEE Particle Acc. Conf., Chicago, IL, 71(1989).
- [25] P. Ulmer, Beam Current Measurements - Experiment E89-003 at Jefferson Laboratory, 1998(unpublished).
- [26] CEBAF Conceptual Design Report, 1990.
- [27] K.G.Fissum, VDC Manual, MIT-LNS Internal Report #03, 1997.
- [28] W. Bertozzi *et al.*, Nucl. Instrum. Methods (to be published).
- [29] CODA User's Manual, 1995
- [30] W. Bertozzi *et al.*, Nucl. Instrum. Methods **A111** 1 (1968).
- [31] J. Gao *et al.*, Beam Energy Measurement at Jefferson Lab Using the Hall A Spectrometers, MIT-LNS Internal Report #04, 1998.
- [32] L. Weinstein, Ph.D. thesis, MIT, 1988(unpublished).

- [33] James.J. Kelly, private communication.
- [34] G.G. Simon *et al.*, Nuclear Physics **A333** 381(1980).
- [35] J. Schwinger, Physical Review **76** 760(1949).
- [36] Y.S. Tsai, Reviews of Modern Physics **122** 1898(1961).
- [37] L.W. Mo and Y.S. Tsai, Reviews of Modern Physics **41** 205(1969).
- [38] E. Quint, Ph.D. thesis, NIKHEF 1988(unpublished).
- [39] R. Florizone, Ph.D. thesis, MIT 1999(unpublished).
- [40] S. Penner, Nuclear Structure Physics, Proceedings of the 18th Scottish Univ. Summer School in Physics, 284(1977).
- [41] J. Friedrich, Nucl. Instrum. Methods **129** 505(1975).
- [42] D.J.S. Findlay and A.R. Dusautory, Nucl. Instrum. Methods **174** 531(1980).
- [43] J.W. Van Orden, private communication.
- [44] F. Perey and B. Buck, Nuclear Physics **32** 353(1962).
- [45] A. Picklesimer, J.W. Van Orden, and S.J. Wallace, Phys. Rev. **C32** 1312(1985).
- [46] A. Picklesimer and J.W. Van Orden, Phys. Rev. **C40** 290(1989).
- [47] J.D. Walecka, Ann. of Phys. **83** 491(1974).
- [48] C.J. Horowitz and B.D. Serot, Nuclear Physics **A368** 503(1981).
- [49] M.V. Hynes *et al.*, Phys. Rev. **C31** 1438(1985).
- [50] N. Liyanage *et al.*, MIT-LNS Internal Report #05, 1998.
- [51] E. Offermann, private communication.
- [52] E. Offermann, ESPACE Manual.

- [53] D. Jordan, Ph.D. thesis, MIT 1994(unpublished).
- [54] R. Veenhoff, GARFIELD, *a drift chamber simulation program: User's guide*. CERN(1995).
- [55] F. Ajzenberg-Selove, Nuclear Physics **A506** 1(1990).
- [56] J.J. LeRose, private communication.
- [57] J.J. LeRose, Jefferson Lab Tech Notes **TN 97-042**.
- [58] N. Liyanage, Ph.D. thesis, MIT 1999(unpublished).
- [59] J. Gao *et al.*, VDC Logbook (1996).
- [60] B. Wojtsekhowski *et al.*, CEBAF Survey Reports (1996).
- [61] M. Liang, Survey Summary Report (1998).

# Acknowledgments

This thesis could not have been accomplished without the help of many individuals. Therefore, I feel obligated to make a list of their contributions here, even though the list may not be complete. I apologize for any possible but unintentional omissions.

First, I would like to thank my thesis advisor Professor William Bertozzi for being generous with his time, attention, patience and encouragement throughout this project. Bill's physical sense and insight always impressed me. During the last four and half years, many long and useful discussions with him not only enriched my physics knowledge, but more importantly, made a professional nuclear physicist out of me.

I would also like to thank Dr. Shalev Gilad for many interesting conversations about the VDC construction, experimental data taking and data analysis. Shalev acted as my mentor in many aspects. One thing I will always remember is that at the final stage of assembling the first VDC, he was the only person who realized that the VDC center frame should be reversed to avoid blocking the gas flow.

I would like to thank Dr. Jeff Templon for his participation in the VDC project, which made flipping the 250 lbs wire plane a snap (because Jeff could lift one side by himself while Nilanga and I held the other side).

I would like to thank Dr. Kevin Fissum for his tremendous efforts throughout the entire project. Kevin contributed not only to installing and maintaining the VDCs, commissioning the spectrometers and organizing the data taking and data analysis, but also he proofread this thesis, which made quite a difference.

I would like to thank Dr. Larry Weinstein and Dr. Paul Ulmer for optimizing the beam time for this experiment, and sharing their experience in data analysis. The pizza meetings at ODU were fun and also helped to derive solutions to several difficult problems during the data analysis.

I would like to thank Dr. Larry Cardman and Dr. Kees De Jager, the former and

the present Hall A leaders, for their efforts and influence in making this experiment both prompt and successful. I would also like to thank the Hall A staff members: Drs. Jian-Ping Chen, Bob Michaels, Javier Gomez, Eddy Offermann, Bogdan Wojtsekhowski, Sirish Nanda, John LeRose, Arun Saha, Ole Hansen, Eugene Chudakov, Meihua Liang and Michael Kuss for sharing their expertise with me. I would like to thank the Jefferson Lab accelerator crew for delivering stable, high quality beam during this experiment.

I would like to thank Dr. Franco Garibaldi and his group for building the waterfall target for this experiment. I would also like to thank the E89-033 spokespersons Drs. George Chang, Charles Glashauser, Sirish Nanda and Paul Rutt for sharing part of their data. Finally, I would like to thank all the collaborators who built equipment or took shifts for this experiment. Forgive me that I cannot list all your names here.

I would like to thank Dr. James Kelly for many useful theoretical discussions and for teaching me how to use his theoretical calculation code LEA. I would like to thank Dr. Wally Van Orden for providing theoretical calculations for this experiment. I would like to thank Dr. Bill Donnelly for giving me theoretical advice, and I would like to thank another thesis committee member, Prof. Alan Guth for reading my thesis.

Many thanks to my fellow graduate student Nilanga Liyanage for working closely with me during the entire project, from building the VDCs to performing the data analysis. Nilanga is a very fine person and it is a pleasure to work with him. I enjoyed many useful discussions with him as well as several road trips from Cambridge to Newport News. Also, I have to thank Krishni Wijesooriya for cooking all those wonderful meals.

I would like to thank other members of the Nuclear Interactions Group, Drs. Jianguo Zhao, Zilu Zhou and David Rowntree for participating this experiment and sharing their useful opinions.

I would like to thank all the friends I knew either at MIT or Jefferson Lab. They are Jiang Chen, Richard Florizone, Shiao-bin Soong, Haijun Song, Jian Tang, Alex Skabelin, Alaine Young, Christian Kunz, Riad Suleiman, Kathy McCormick, Gilles Quemener, Mark Jones, Luminita Todor, Paul Gueye, Sergey Malov, Zhengwei Chai, Bin Zhang, Marat Rvachev, Feng Xiong and Wang Xu. They made my graduate studies an enjoyable experience.

I would like to thank Joanne Gregory for making all the travel arrangements.

At last, but definitely not least, I extend special thanks to my wife (also my fellow graduate student at MIT), Wenxia Zhao, for encouraging me and helping me through many difficult moments over all these years together. Without her support, I cannot imagine where I could have ended up.

I would like to thank my parents for helping me in many ways. They always believed that the greatest gift they could give to their children was to provide them with the opportunity to pursue higher education. I will thank them for this provision for the rest of my life.

# Biographical Note

Juncai Gao was born on August 5th, 1970 in Hubei Province, China. In 1985, he went to the University of Science and Technology of China, and received a B.Sc. in physics in July, 1990. After spending three years as a graduate student at the Institute of High Energy Physics, Beijing, he obtained a M.Sc. in experimental particle physics. There, he met and married Wenxia Zhao.

In September 1994, the author entered the Massachusetts Institute of Technology as a Ph.D. student. Since then, he has played a major role in building the Vertical Drifting Chambers, commissioning the High Resolution Spectrometers as well as initiating the physics program in Hall A at Jefferson Lab. In March, 1999, he will join the California Institute of Technology as a postdoctoral scholar.

The author is a member of the American Physical Society. He plays Go, table-tennis, badminton and tennis. He is also a huge soccer fan.